To the Graduate Council:

I am submitting herewith a thesis written by Ronald J. Litchford entitled "Formulation and Evaluation of a High-Pressure Discrete Droplet Gasification Model for Bipropellant Liquid Rocket Combustor Modeling Applications." I have examined the final copy of this thesis for form and content and recommend that it be accepted in partial fulfillment of the requirements for the degree of Master of Science, with a major in Mechanical Engineering.

San-Mou Jeng

San-Mou Jeng, Major Professor

We have read this thesis
and recommend its acceptance:

Roy J. Schultz

Carroll E. Peters

Accepted for the Council:

Vice Provost
and Dean of the Graduate School

STATEMENT OF PERMISSION TO USE

In presenting this thesis in partial fulfillment of the requirements for a Master's degree at the University of Tennessee, Knoxville, I agree that the Library shall make it available to borrowers under rules of the Library. Brief quotations from this thesis are allowable without special permission, provided that accurate acknowledgment of the source is made.

Permission for extensive quotation from or reproduction of this thesis may be granted by my major professor, or in his absence, by the Head of Interlibrary Services when, in the opinion of either, the proposed use of the material is for scholarly purposes. Any copying or use of the material in this thesis for financial gain shall not be allowed without my written permission.

Signature Ronald J. Litchford

Date 22 November 1989

Formulation and Evaluation of a High-Pressure Discrete Droplet Gasification Model for Bipropellant Liquid Rocket Combustor Modeling Applications

A Thesis

Presented for the

Master of Science

Degree

The University of Tennessee, Knoxville

Ronald J. Litchford

December 1989

ACKNOWLEDGMENTS

I wish to acknowledge and thank my major professor Dr. San-Mou Jeng for his contributions and guidance in the work reported in this thesis, and I also wish to express my thanks to Dr. Roy Schulz and Dr. Carroll Peters for serving on my committee. I acknowledge the assistance of my laboratory associate, Mr. Chris Norton, in the experimental work reported, and Mr. Jim Goodman, senior engineer with the Center for Laser Applications, deserves my special thanks for his contributions in the design and acquisition of the experimental apparatus. In particular, I want to thank my wife, Betrice, and our son, Thomas, for their many sacrifices during the course of my graduate studies and during the research and preparation of this thesis. The work reported was conducted while the author was supported by a NASA Graduate Student Researcher Fellowship through the Marshall Space Flight Center in Huntsville, Alabama under Training Grant NGT–50360. Partial funding was also derived from a Rocketdyne supported spray combustion stability study by the Center for Advanced Space Propulsion at UTSI. Computational and laboratory resources for this work were generously provided by the Center for Laser Applications at UTSI. Whatever errors appear in in this thesis are solely my responsibility.

ABSTRACT

This thesis presents the formulation of a high-pressure, discrete droplet gasification submodel for application in a spray combustion CFD code and an evaluation of its potential for use in liquid rocket combustor modeling. Introductory background information and a critical review and survey of the research literature are presented to identify current research status and needs and to assimilate existing knowledge as a basis for model development. The theoretical formulation of a spherically-symmetric, diffusion-transport-controlled, and quasi-steady, time-dependent gasification model, with empirical corrections for convective effects, is presented. And thermodynamic vapor-liquid equilibria models, based upon the Redlich-Kwong equation of state with modified mixing rules for high ambient pressures, are described. Computer codes are developed allowing comparison of theoretical predictions with available experimental data for validation. The pressure dependent parametric behavior of an n-pentane droplet vaporizing in hot nitrogen gas is also examined for subcritical, critical, and supercritical pressures. Vapor-liquid equilibria calculations are performed for an oxygen–hydrogen system using quantum gas mixing rules, and the results are utilized in an investigation of LOX droplet behavior when injected into the hydrogen-rich gas of a high-pressure, liquid rocket combustor. In addition, an evaluation of the gasification characteristics of these LOX droplets in the high-frequency, transverse-mode acoustic oscillations of liquid rocket combustion instability is made from which a physical mechanism for the initiation or sustenance of instability, termed *punctuated criticality*, is proposed. Some droplet size measurements from preliminary, elevated-pressure droplet combustion experiments are given for hydrocarbons burning in air.

CONTENTS

CHAPTER PAGE

1 INTRODUCTION AND MOTIVATION 1

1.1 Prefatory Remarks 1

1.2 General Motivation With Regard To Spray Combustion Modeling 2

1.3 Particular Motivation With Regard To Liquid Rocket Combustor Modeling 7

2 BACKGROUND INFORMATION AND RETROSPECTIVE SURVEY 9

2.1 High-Pressure Droplet Gasification Theory 9

2.2 The Role of Droplet Gasification in High-Frequency Liquid Rocket Combustion Instability Theory 23

3 THEORETICAL MODELING OF HIGH-PRESSURE DROPLET GASIFICATION 26

3.1 Theoretical Formulation of Transport Model 26

3.1.1 Diffusion Controlled Transport Model 26

3.1.2 Mass Transfer by Aerodynamic Stripping Vaporization 46

3.2 Formulation of Thermodynamic Vapor-Liquid Equilibria Models . . 47

3.2.1 Fundamental Relations of Phase Equilibria Thermodynamics 47

3.2.2 A General High-Pressure Vapor-Liquid Equilibria Model with the Redlich-Kwong Equation of State 54

3.2.3 Modification of General High-Pressure Vapor-Liquid Equilibria Model for Inclusion of Quantum Gases 61

3.2.4 A Simplified Vapor-Liquid Equilibria Model with the Redlich-Kwong Equation of State: No Ambient Gas Absorption 64

4 NUMERICAL SIMULATION, MODEL VALIDATION, AND PARAMETRIC BEHAVIOR 68

4.1 Numerical Simulation Codes and Model Validation 68

4.1.1 Evaluation of Vapor-Liquid Equilibria Models 68

4.1.2 Evaluation of Transport Model 78

4.2 Pressure Dependent Parametric Behavior: High-Pressure Droplet Vaporization Theory 87

5 APPLICATION TO LOX/HYDROGEN LIQUID ROCKET COMBUSTOR MODELING 108

5.1 Isobaric LOX Gasification in LOX/H_2 High-Pressure, Cylindrical Combustor 108

5.1.1 LOX/H_2 High-Pressure Vapor-Liquid Equilibria 108

5.1.2 Simulation of Isobaric LOX Droplet Gasification in a LOX/H_2 High-Pressure, Cylindrical Combustor 112

5.2 LOX Gasification in Acoustically Oscillating Field Inside a LOX/H_2 High-Pressure, Cylindrical Combustor 120

5.2.1 High-Frequency Transverse-Mode Acoustic Oscillation Theory for a Cylindrical Combustor 120

5.2.2 Simulation of LOX Gasification in Unstable LOX/H_2 High-Pressure, Cylindrical Combustor 122

6 PRELIMINARY RESULTS FROM DROPLET COMBUSTION EXPERIMENTS AT ELEVATED PRESSURES 133

6.1 Scope of Experimental Effort 133

6.2 Experimental Apparatus and Set-Up 133

6.3 Experimental Results 136
7 CONCLUDING REMARKS 143
LIST OF REFERENCES 146
VITA 153

LIST OF FIGURES

FIGURE PAGE

1 Schematic representing steady-state and fully transient droplet vaporization for simplified ideal-gas vapor-liquid equilibria model;(a)$P_v < P_{amb} \leq P_c$, (b)$P_v \leq P_c < P_{amb}$ 14

2 Qualitative droplet temperature histories at different pressures 16

3 Schematic of typical vapor-liquid equilibria for a binary system 19

4 Schematic representing threshold to fully transient droplet gasification 19

5 Schematic of transport processes during gasification of a propellant droplet 30

6 Representative time dependent propellant vapor concentration profiles as gasification proceeds 38

7 Comparison of theoretical equilibria from no-absorption model and ideal-gas model (dashed line) with experimental data for the n-hexane—nitrogen binary system at $T_\infty = 220\ F$ 70

8 Comparison of theoretical equilibria from no-absorption model and ideal-gas model (dashed line) with experimental data for the n-hexane—nitrogen binary system at $T_\infty = 280\ F$ 71

9 Comparison of theoretical enthalpy of vaporization, based upon a no-absorption model, to the latent heat of vaporization for the n-hexane—nitrogen binary system 73

10 Comparison of theoretical equilibria from general model including ambient gas absorption with experimental data at $P_\infty = 600\ psia$

for the n-pentane—nitrogen binary system 75

11 Theoretical equilibria from general model including ambient gas absorption at supercritical pressures for the n-pentane—nitrogen binary system 76

12 Comparison of theoretical enthalpy of vaporization from general model including ambient gas absorption at supercritical pressures with the latent heat of vaporization for the n-pentane—nitrogen binary system 77

13 Comparison of theoretical and experimental vaporization histories of n-hexane droplet in nitrogen gas at 548 K and 20.4 atm 82

14 Comparison of theoretical and experimental vaporization histories of n-hexane droplet in nitrogen gas at 548 K and 81.6 atm 83

15 Comparison of theoretical and experimental vaporization histories of n-heptane droplet in nitrogen gas at 573 K and 11 atm 84

16 Comparison of theoretical and experimental vaporization histories of n-heptane droplet in nitrogen gas at 573 K and 31 atm 85

17 Comparison of theoretical and experimental vaporization histories of n-heptane droplet in nitrogen gas at 573 K and 51 atm 86

18 Calculated $d_d^2/d_{d_0}^2$ ratio histories at different ambient pressures for n-pentane drop in N_2 90

19 Calculated droplet temperature histories at different ambient pressures for n-pentane drop in N_2 91

20 Calculated m_d/m_{d_0} ratio histories at different ambient pressures for n-pentane drop in N_2 93

21 Calculated vaporization mass flux histories at different ambient pressures for n-pentane drop in N_2 94

22 Calculated heat transfer coefficient histories at different ambient pressures for n-pentane drop in N_2 96
23 Calculated mass transfer coefficient histories at different ambient pressures for n-pentane drop in N_2 97
24 Calculated heat flux histories at $P_r = 0.5$ for n-pentane drop in N_2 98
25 Calculated heat flux histories at $P_r = 1$ for n-pentane drop in N_2 99
26 Calculated heat flux histories at $P_r = 2$ for n-pentane drop in N_2 100
27 Calculated surface regression parameter and mass transfer B number histories at $P_r = 0.5$ for n-pentane drop in N_2 102
28 Calculated surface regression parameter and mass transfer B number histories at $P_r = 1$ for n-pentane drop in N_2 103
29 Calculated surface regression parameter and mass transfer B number histories at $P_r = 2$ for n-pentane drop in N_2 104
30 Calculated Prandtl number, Schmidt number, and Lewis number histories for $P_r = 0.5$ for n-pentane drop in N_2 105
31 Calculated Prandtl number, Schmidt number, and Lewis number histories for $P_r = 1$ for n-pentane drop in N_2 106
32 Calculated Prandtl number, Schmidt number, and Lewis number histories for $P_r = 2$ for n-pentane drop in N_2 107
33 Comparison of theoretical equilibria from general model including ambient gas absorption with current correlation in ARICC-LJ code for oxygen—hydrogen binary system 110
34 Comparison of theoretical enthalpy of vaporization from general

model including ambient gas absorption at supercritical pressures with the latent heat of vaporization for the oxygen—hydrogen binary system 111

35 Calculated $d_d^2/d_{d_0}^2$ ratio histories for LOX/H_2 liquid rocket combustor 114

36 Calculated droplet temperature histories for LOX/H_2 liquid rocket combustor 115

37 Calculated m_d/m_{d_0} ratio histories for LOX/H_2 liquid rocket combustor 117

38 Calculated relative axial droplet velocity in LOX/H_2 liquid rocket combustor 118

39 Calculated axial distance traveled by LOX droplet in LOX/H_2 liquid rocket combustor 119

40 Pressure and velocity oscillations of a traveling-transverse resonant acoustic mode in a cylindrical LOX/H_2 combustion chamber 123

41 Calculated droplet temperature and acoustic pressure oscillation histories for LOX droplet injection phase angle $\theta = 0$ 126

42 Calculated droplet temperature history on LOX/H_2 vapor-liquid equilibria diagram for LOX droplet injection phase angle $\theta = 0$ . . . 127

43 Schematic of *punctuated criticality* process 129

44 Calculated droplet temperature and acoustic pressure oscillation histories for LOX droplet injection phase angle $\theta = -\pi$ 130

45 Calculated droplet temperature history on LOX/H_2 vapor-liquid equilibria diagram for LOX droplet injection phase angle $\theta = -\pi$ . . 131

46 Schematic of experimental arrangement for elevated pressure hydrocarbon droplet combustion tests 134

47 Experimentally observed $d_d^2/d_{d_0}^2$ ratio history for n-pentane burning in dry air at $P = 100$ psig ($P_r = 0.2343$) 138

48 Experimentally observed $d_d^2/d_{d_0}^2$ ratio history for n-pentane burning in dry air at $P = 150$ psig ($P_r = 0.3364$) 139

49 Experimentally observed $d_d^2/d_{d_0}^2$ ratio history for n-pentane burning in dry air at $P = 200$ psig ($P_r = 0.4386$) 140

50 Experimentally observed $d_d^2/d_{d_0}^2$ ratio history for 2,2,4 trimethylpentane burning in dry air at $P = 180$ psig ($P_r = 0.5215$) . . 141

NOMENCLATURE

English Symbols

A	area (m^2)
A^*	defined variable [eqt. (3.32)] (m^{-2})
a	Redlich-Kwong equation of state constant $(kN\,K^{\frac{1}{2}}\,m^4/kmol^2)$ or gas-phase speed of sound (m/s)
B	mass transfer driving potential
B^*	defined variable [eqt. (3.33)] $(kg/m^2\,s)$
b	Redlich-Kwong equation of state constant $(m^3/kmol)$
C	number of components or species in a system
C_D	drag coefficient
C_p	isobaric specific heat $(kj/kg\,K)$
$\mathcal{D}$	diffusivity (m^2/s)
d	diameter (m)
f	fugacity (kPa) or frequency (Hz)
F	thermodynamic degrees of freedom of a system
F_D	drag force (N)
g	earth gravity $(9.81\ m/s^2)$
Gr	Grashof number, $g(1-\frac{\rho_s}{\rho_\infty})(\frac{d_d^3}{\nu^2})$
h	heat transfer coefficient $(kj/m^2\,s\,K)$
h_{vap}	heat of vaporization (kj/kg)

$\tilde{h}_i$	partial molar enthalpy of the ith component $\left[\left(\frac{\partial H}{\partial n_i}\right)_{T,P,n_{j(j\neq i)}}\right]$ $(kj/kmol)$
J	Bessel function
k	mass transfer coefficient $(kg/m^2\,s)$
k_{ij}	binary interaction constant
$\overline{L}$	molar latent heat of vaporization $(kj/kmol)$
Le	Lewis number, $\lambda/\rho C_p \mathcal{D}$
m	mass (kg)
$\dot{m}$	mass flow (kg/s)
$\dot{m}''$	mass flux $(kg/m^2\,s)$
Nu	Nusselt number, hd_d/λ
n	mole number (mol)
ODE	ordinary differential equation
P	pressure (kPa)
P_r	reduced pressure
Pr	Prandtl number, $\nu\rho C_p/\lambda$
Q	heat transfer rate (kW)
$\overline{R}$	universal gas constant $(8.31439\,kj/kmol\,K)$
Ra	Rabin number, $We/Re^{\frac{1}{2}}$
Re	Reynolds number, $\Delta V d_d/\nu$
RHS	right hand side
r	radius (m)
Sc	Schmidt number, $\nu/\mathcal{D}$
Sh	Sherwood number, $kd_d/\rho^v \mathcal{D}$

T	temperature (K)
T_r	reduced temperature (K)
t	time (s)
U	velocity (m/s)
V	volume (m^3) or velocity (m/s)
W	molecular weight $(kg/kmol)$
We	Weber number, $\rho_p d_d \Delta V^2/\sigma_p$
v	velocity (m/s)
$\overline{v}$	molar specific volume $(m^3/kmol)$
x	mole fraction
y	mass fraction
Z	compressibility factor

Greek Symbols

α	weighting coefficient
γ	specific heat ratio
Δ	relative to freestream condition
ζ	surface regression parameter [eqt. (3.3)]
θ	angular displacement
λ	thermal conductivity $(kj/m\,s\,K)$
μ	chemical potential $(kj/kmol)$
ν	kinematic viscosity (m^2/s)
Π	number of thermodynamic phases in a system
π	3.14159...
ρ	density (kg/m^3)

σ	surface tension (N/m)
φ	fugacity coefficient
ϕ	generic property or parameter
Ω_a	dimensionless constant in Redlich-Kwong equation of state
Ω_b	dimensionless constant in Redlich-Kwong equation of state
ω	acentric factor

Subscripts and Superscripts

a	ambient gas or ambient gas mixture
amb	ambient condition
amp	amplitude of perturbation
$axial$	axial component
c	thermodynamic critical condition
$crit$	critical threshold condition
d	droplet
eff	effective value
$evap$	evaporative condition
F	final condition
in	transport to the drop
i	ith component
j	jth component
l	liquid state
$mean$	average value
N	number of components in system

out	transport away from drop
p	propellant
r	radial component
ref	reference condition
rel	relative condition
s	surface condition
$strip$	aerodynamic stripping condition
ss	steady-state condition
t	tangential component
v	vapor state
$wall$	chamber wall
x	directional component in rectangular coordinates
y	directional component in rectangular coordinates
z	directional component in rectangular coordinates
θ	tangential direction or phase angle
∞	condition at infinite distance from droplet
$\circ$	ideal gas condition or classical value

CHAPTER 1

INTRODUCTION AND MOTIVATION

1.1 PREFATORY REMARKS

The frequently encountered realm of high-pressure droplet gasification encompasses combustor environments at near-critical and supercritical pressures of the drop liquid. This includes the major prime movers used in propulsive and automotive applications. In the propulsion field, for example, typical liquid rocket operating conditions are generally supercritical for both cryogenic fuel/oxidants and hydrocarbon fuels, and proposed new-generation aircraft gas turbines will run at maximum combustor pressures, around 25 atm, very close to the critical pressure of characteristic hydrocarbon fuels. Of course, the spray processes within these combustors are important to their successful operation. The high-frequency, screeching instability of liquid rocket motors, for instance, is crucially dependent upon the spray characteristics near the propellant injection plate, and the liquid spray evaporation rate in gas turbine combustors determines the fuel vapor concentration entering the downstream combustion zone. In relevance to reciprocating internal combustion engines, the fuel spray in diesel engines experiences pressures in excess of 1000 psi, well above the critical pressure of the various fuel components, and the drop life history is of importance as it determines the fuel vapor available for ignition and combustion and whether a drop gasifies completely before impacting the piston or chamber wall. Spark ignition engines may also have residual, unevaporated fuel drops in the cylinder during the compression stroke which will experience increasingly higher pressures as the piston nears top-dead-center (TDC) and ignition of the fuel-vapor/air mixture occurs.

Because spray processes play such a fundamental, precursory role in a wide variety of high-pressure combustors, in particular liquid rocket motors, individual droplet gasification at high ambient pressures is of serious, practical concern and is the subject of this work. In fact, the physical phenomena of this problem are so closely linked to the successful operation of these combustors that it has received considerable attention over the past thirty years with a substantial increase in our understanding of the thermodynamics and fluid mechanical transport processes involved. But with increased computing power and complex computational fluid dynamic (CFD) methodologies for spray combustion modeling becoming available, development of practical, yet comprehensive, physical submodels for droplet gasification at high combustor pressures will be needed. It is the intent of this work, therefore, to assimilate present knowledge in this area and take steps toward its implementation in a workable engineering submodel with an emphasis on bipropellant liquid rocket engines. Because the current trend in propulsive devices using liquid fuels is to operate at increasingly higher pressures in order to increase the thrust/weight ratio, combustion efficiency, and overall engine performance and since there has been a resurgence of interest in efficient, reliable liquid rocket engines, a continued research concern in this area may be expected from the aerospace community.

1.2 GENERAL MOTIVATION WITH REGARD TO SPRAY COMBUSTION MODELING

Obviously, the successful design and operation of liquid-fueled combustion devices depends upon a knowledge and understanding of the interphase exchange of mass, momentum, and energy in high-pressure, two-phase, chemically reacting

flows. With this understanding, detailed and comprehensive computational codes may be developed and employed as design tools capable of estimating the performance, heat transfer characteristics, and flow dynamics of practical spray combustion systems.

To date, a number of spray combustion models based on finite difference solutions of the governing partial differential equations have been developed with attempts made at validation. Because the interphase transport occurs on length scales smaller than the grid scales of current CFD codes, these models have incorporated alternative approaches for the submodeling of liquid-phase and gas-phase exchange processes which have varied in degree of complexity and success. The ability of these codes to make accurate simulations is inherently dependent upon the validity of these physical submodels, and code deficiencies are generally the result of inadequate submodels. The modeling approaches can be categorized and subcategorized as follows (Faeth, 1979; Kuo, 1986):

(1) **Locally-Homogeneous-Flow (LHF) MODELS.** The gas-phase and liquid-phase drops are assumed to be in local dynamic and thermodynamic equilibrium throughout the flow. These assumptions imply that interphase transport is fast in comparison to the development of the whole flow field. The relationships between mixture enthalpy, composition, temperature, density, and mixture fraction can be regarded as equations of state. The mixture fraction becomes a dependent variable and the conservation equations reduce to that of single phase flows.

   (a) *Integral Model* (IM). Employs integral turbulence models.

   (b) *Full-Field Modeling* (FFM). Employs full-field partial differential equations governing mean flow properties and turbulence parameters.

(c) *Large Eddy Simulation* (LES). Entails time-dependent calculations of grid scale or larger turbulence structure with specified initial conditions to reflect randomness. Modeling required only for sub-grid scale turbulence. Largely undeveloped and presently impractical due to enormous computational time requirements.

(2) **Separated-Flow** (SF) or **Two Phase-Flow** (TPF) **MODELS**. Considers finite rates of interphase transport. Requires that exchange processes between phases be modeled independently. That is, a submodel for liquid droplet gas-phase exchange processes must be formulated.

(a) *Particle-Source-in-Cell Model* (PSICM), *or Discrete-Droplet Model* (DDM). The spray is represented by finite groups of particles which are tracked through the flow field using a Lagrangian formulation. The Eularian gas-phase conservation equations with appropriate source terms correcting for the effect of droplets in the flow are also solved.

(i) *Deterministic Separated-Flow Models* (DSF models). Slip and finite interphase transport is considered but turbulent droplet dispersion and turbulent effects on interphase transport are ignored. The droplet is assumed to be affected only by the mean of the turbulent velocity.

(ii) *Stochastic Separated-Flow Models* (SSF models). Interphase slip and turbulent fluctuations are considered through random sampling of turbulence properties for random-walk computations. The droplet is assumed to be affected by the fluctating velocity components within the turbulent eddies.

(b) *Continuous Droplet Model* (CDM). Invokes use of the spray distribution function concept. The spray distribution function transport

equation is solved with the gas phase conservation equations containing appropriate source terms.

(c) *Continuum-Formulation Model* (CFM). The motion of the drops and gas are treated as an interpenetrating continua yielding similar governing equations for both phases.

(d) *Group-Combustion Models* (GCM). The collective behavior of discrete droplets in a spray cloud are accounted for by a simultaneous analysis of the group interaction within a heterogeneous inner core region and with a homogeneous gas-phase outer region. Depending upon the group combustion number, the drops may be undergoing pure vaporization with the fuel vapor migrating to a stand off flame surrounding the spray cloud, drops in the core may be undergoing pure vaporization with a diffusion flame inside the spray cloud while outer droplets burn with individual envelope flames, or the drops in the cloud may all burn within discrete envelope flames.

The LHF approximations lead to spray combustion models that are generally suitable for sprays where the drop size is small, the densities of the two phases are comparable, and the rate of development of the whole flow process is slow. Otherwise, LHF models, although advantageous from the point of view that the fluid mechanic conservation equations need be solved for one phase only, tend to overestimate the rate of development of the flow since they neglect the finite-rate nature of actual transport processes. One experimentally verified exception (Newman and Brzustowski, 1971) is the case where a liquid near its thermodynamic critical point was injected into a high-pressure gas, a situation which favors the LHF approximations due to reduced surface tension, leading to very small drops and less interphase

slip (relative velocity between phases), and decreasing liquid phase density near the critical point. This case yielded good agreement for the spray boundary, and leads one to assume that the LHF model might be applicable to high-pressure combustors in which the injected, relatively cool drops heat up and approach or possible even reach their critical point. Shearer and Faeth (1977), however, found the deduction unfounded as slip near the injector remains important since the vaporization process as a whole is shorter. The resulting consensus is that the primary value of LHF models is in providing a preliminary assessment of the spray process.

For analysis of practical spray combustors, SF models are desirable as they allow for slip and finite transport rates between phases. Since a spray is essentially a droplet cloud, at least downstream from the near-injector atomization region, the liquid phase is conventionally modeled as discrete droplet parcels in SF codes. Even for the case of group-combustion models, where collective droplet transport interactions are considered, a knowledge of discrete droplet behavior is required. As a result, single droplet models are formulated with simplifying assumptions to reduce computational effort yet with sufficient detail to correctly account for important transport characteristics. Many such models have been proposed for low and moderate pressures and some few for the realistic high-pressure case. Generally, the models have been based upon the assumptions of spherical symmetry, diffusion-controlled transport, and quasi-steady time dependence with empirical corrections for natural or forced convection and have correlated reasonably well in most cases with experimental results. Because of this success, the author has undertaken an effort to formulate, with similar assumptions, a general high-pressure droplet gasification model with an aim toward application in SF computational models for spray combustion.

1.3 PARTICULAR MOTIVATION WITH REGARD TO LIQUID ROCKET COMBUSTOR MODELING

Early liquid rocket engine development in the 50's and during the intense space exploration programs of the 60's was more of an engineering art than a science, and it remains so to a large extent today. Indeed, pioneering trial and error design methods employed for liquid rocket injectors required many expensive, time consuming developmental iterations, and only after a successful injector design was obtained was chamber wall compatibility considered, with the result that final design flight engines sometimes operated far from optimal performance and weight conditions (Valentine, 1972). For optimum design and minimum developmental iterations, therefore, an understanding of the interactions between factors influencing performance, stability, and wall compatibility is essential.

Apparently, droplet vaporization theory provides a rate limiting basis for the interrelated effects observed to occur in the thrust chamber, and analytical engineering techniques for prediction of combustor dynamics and stability limits depend upon valid propellant droplet gasification models. Furthermore, a maturing of the liquid rocket design process is resulting in the development of comprehensive CFD spray combustion codes for detailed combustor modeling (Sutton *et al.*, 1972; Reichel *et al.*, 1973; Liang *et al.*, 1985; Jiang and Chiu, 1986; Philipart and Moser, 1988; Fang and Jones, 1987; Liang, 1989). These codes yield predicted behavior that is sensitive to the physical submodels employed, and the validity of their predictions depends upon the validity of the atomization and droplet gasification submodels. The limitations imposed upon the practical application of the codes are directly related to the interphase transport processes being modeled. Thus, current research interests are on the formulation and experimental validation of atomization

and droplet gasification models which are computationally efficient yet sufficiently sophisticated to encompass the physics of the actual processes.

For this reason, the formulation of a high-pressure, time-dependent discrete droplet gasification model has been pursued in this study with special emphasis for application to bipropellant liquid rocket combustor modeling. Because of immediate concern to the Space Shuttle Main Engine (SSME), an evaluation of LOX droplet behavior was conducted for the case of injection into a high-pressure, gaseous, hydrogen rich rocket chamber. An examination was also made of LOX droplet gasification characteristics in the presence of high-frequency transverse-mode acoustic oscillations representative of liquid rocket combustion instability.

CHAPTER 2

BACKGROUND INFORMATION AND RETROSPECTIVE SURVEY

2.1 HIGH-PRESSURE DROPLET GASIFICATION THEORY

In approaching the phenomena of droplet vaporization at elevated pressures, the fundamental physical mechanisms which distinguish the high-pressure case from the low-pressure case must be recognized and taken into consideration. Whereas the fundamental mechanisms of low-pressure droplet gasification are reasonably well understood and present theoretical formulations employing film theory, the quasi-steady assumption, and phase equilibrium on the basis of the pure liquid vapor pressure ideal-gas concept confirm our phenomenological descriptions and correspond to experimental data (Faeth, 1977; Law, 1982), development of theory for high-pressure droplet gasification theory has lagged due to a larger degree of uncertainty and increased complexity in the physical processes. For example, the quasi-steady assumption implies that the diffusion time scale is small enough for the gas phase to adjust rapidly to changing boundary conditions and that heat and mass transfer rates can be determined from a steady-state solution for the boundary conditions corresponding to each instant of time. The extrapolation of this supposition into the high-pressure regime is questionable but seems to be a plausible approach at least for vaporization to the critical state. On the other hand, a comparison of the simplified ideal-gas vapor-liquid equilibria predictions with experimental results at high pressures reveal substantial deviation such that a more complex and more physically realistic model is needed (Kuo, 1986). Other phenomenological perplexities encountered require careful examination.

The peculiarities encountered at elevated pressures derive primarily from thermodynamic considerations. For instance, with increasing pressure, absorption of ambient gas into the liquid occurs and real-gas effects become important in determining thermophysical properties and thermodynamic phase equilibrium. The critical temperature and pressure no longer occur at the pure component critical point but become a function of the mixture composition producing a locus of critical points designated as *the critical mixing line.* If the droplet temperature approaches the critical mixing state, the enthalpy of vaporization decreases to zero, the specific heat approaches infinity, and the liquid-phase and gas-phase densities become comparable. This in turn can affect the magnitude of the surface regression rate since the ratio of the ambient gas mass flux to the fuel vapor mass flux at the surface may become significant. For increasingly higher drop temperatures, surface motion caused by bulk thermal expansion of the liquid drop must be considered as well, and since the surface tension approaches zero near the critical mixing line, the drop is expected to undergo extreme deformation and breakup. Of crucial consequence is the implication – to be demonstrated later – that the droplet temperature never reaches steady-state conditions but continuously changes throughout the drop lifetime for ambient pressures sufficiently higher than the pure component critical pressure. This is in stark contrast to the low-pressure prediction of a relatively short heat-up period followed by steady-state gasification at the wet-bulb temperature. This behavior requires that any high-pressure model account for the inherent time dependence implied from thermodynamics and heat/mass transport processes. If the ambient temperature is so low that the critical mixing line is unattainable by droplet heating, many of these phenomena cannot occur; however, such low temperature environments are not encountered in practical combustors.

Despite the complexity of the problem, there have been many fruitful efforts over the years to understand and model droplet gasification at elevated pressures. Much of the initial work in this area was concerned with combustion behavior once the drop had attained the critical condition. For example, Spalding (1959) initially presented a time dependent analysis of supercritical droplet combustion by modeling the process as an instantaneous point source of fuel vapor surrounded by a diffusion flame yielding analytical solutions for the burning time and flame history. His results emphasized the important transient nature of droplet combustion at high pressures and stressed the invalidity of the steady-state approach in this regime. Rosner (1967) relaxed the point source assumption and allowed for an instantaneous distributed fuel vapor source producing similar flame historys but a slightly reduced burning time. The methodology was further extended by Chervinsky (1969) who allowed for radial convection and variable fluid properties. These theories have all essentially concluded that the burning time is proportional to $P_\infty^{1/3}$ and have been generally comfirmed by the experimental work of Faeth *et al.* (1969); however, they are all asymptotic theories applicable only under the assumption that droplet heating has driven the liquid-phase density down such that the drop becomes a puff of dense gas. The supercritical combustion models are essentially laminar, mixing-limited models for the restrictive nonconvective case which provide no information about the subcritical heat-up history nor the critical transition regime. Such theoretical restrictions introduce an important implication. If the subcritical heat-up period and critical transition regime account for a significant portion of the total drop lifetime or significantly affect the flow dynamics of the combustor, then these portions of the gasification history require modeling consideration.

Wieber (1963), in his pioneering investigation of this heat-up period for droplet vaporization, demonstrated how a liquid droplet can experience continuous heating

to supercritical transition and explained the possible role of this process in liquid rocket combustion instability. He considered a time dependent analysis of droplet vaporization in a high-pressure, high-temperature rocket combustor environment utilizing the quasi-steady gas-phase theory of Priem and Heidmann (1960) while employing realistic thermophysical property evaluations and a simplified ideal-gas, low-pressure phase equilibrium model neglecting real-gas effects and ambient gas absorption into the droplet. Investigating heptane and LOX (liquid oxygen) propellants, Wieber found that a drop would experience continuous heating to its critical temperature under sufficiently high gas pressure with less than 10% of the initial drop mass evaporated. He also postulated that, because LOX droplets will experience near-critical temperatures and thus vapor pressures almost equal to the respective chamber pressures, vaporization of LOX may occur by surface ebullition (surface boiling). He further concluded that these boiling LOX drops may interact with a pressure rarefaction causing them to shatter or release a surge of oxygen vapor which might initiate or support combustion instability. This is worth noting as present investigations in this thesis will show that inclusion of high-pressure thermodynamics infers pressure induced gasification response inversed to that proposed by Wieber.

The most important conclusion from Wieber's calculations, though, was that a drop will not reach a steady-state temperature for sufficiently high ambient pressures but will heat continuously to the critical state, thus establishing the fully transient nature of the problem. He was able to explain this anomaly mathematically from the governing transport equations and from the thermodynamic behavior of the latent heat of vaporization and the vapor pressure in the limit of the propellant critical temperature.

Avoiding the nonlinear effects in the vaporization process, Wieber assumed

a constant pressure and uniform flow field around the droplet, implying from the Priem Heidmann theory (1960) that the mass transfer rate $\dot{m}_p$ is roughly proportional to $\ln[P_\infty/(P_\infty - P_v)]$ and that the enthalpy transported away from the drop is proportional to $\dot{m}_p h_{vap}$. In addition, a constant incident heat flux to the droplet was assumed for simplicity. By observing that h_{vap} decreases and P_v increases with increasing droplet temperature, Wieber determined general droplet histories as shown in Figure 1 for the two cases: (I) $P_v < P_\infty \leq P_c$ and (II) $P_v \leq P_c < P_\infty$. Wieber's explanation is as follows.

For case (I) where $P_\infty \leq P_c$, the vapor pressure P_v can approach P_∞ as close as necessary in the denominator of the logaritmic term $\ln[P_\infty/(P_\infty - P_v)]$ to give a mass transfer rate as large as necessary such that Q_{out} can always attain the same value as Q_{in}. In this manner, a steady-state temperature is assured for ambient pressures less than the critical pressure of the propellant as depicted for case (I) in Figure 1.

For case (II) where $P_c < P_\infty$, however, the vapor pressure P_v and thus mass transfer rate $\dot{m}_p$ reach an upper limit at the critical temperature T_c. Also, the heat of vaporization goes to zero at the critical point implying that Q_{out} reaches a maximum at a temperature slightly less than the critical temperature. From this behavior, Wieber deduced three possible outcomes represented by curves (a), (b), and (c) for Q_{out} in Figure 1. If $Q_{in} < Q_{out_{max}}$, then a steady-state temperature will be attained as illustrated by curve (a). If $Q_{in} = Q_{out_{max}}$ the maximum possible steady-state temperature will be reached as depicted by curve (b). Finally, for $Q_{in} > Q_{out_{max}}$ the droplet must continue heating to the critical point as implied by curve (c).

The essential characteristics of the transient phenomenon in high-pressure droplet gasification are accounted for by the above explanation; however, predic-

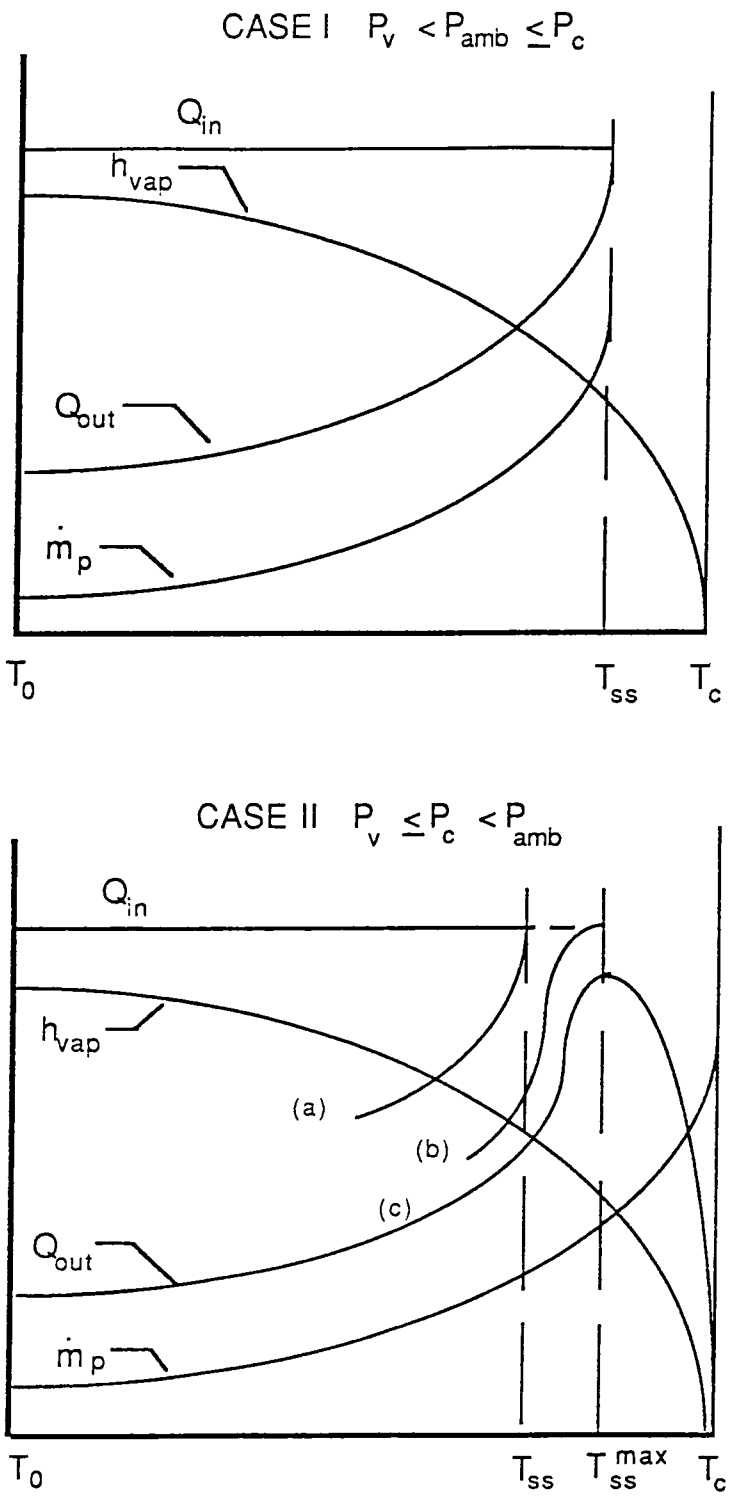

Figure 1. Schematic representing steady-state and fully transient droplet vaporization for simplified ideal-gas vapor-liquid equilibria model;(a)$P_v < P_{amb} \leq P_c$, (b)$P_v \leq P_c < P_{amb}$.

tions for vapor-liquid equilibria and enthalpy of vaporization from multicomponent thermodynamics alter the limiting conditions somewhat. The limiting condition in the actual case is not the pure component critical temperature but the *critical mixing temperature* which is itself a function of pressure and composition. In addition, the mass transfer rate is limited not by the pure component vapor pressure at the critical temperature but by the surface gas-phase propellant concentration at the droplet surface as predicted by multi-component thermodynamics. Furthermore, the actual enthalpy of vaporization deviates substantially from the latent heat of vaporization, due to real-gas effects and ambient gas absorption with increasing pressure. These thermodynamic effects change the limiting conditions, but the qualitative trends expounded by Wieber remain indicative of the actual process.

The theoretical prediction of fully transient droplet gasification has been further demonstrated by the experimental work of Faeth, et. al.(1969), Savery and Borman (1970), Lazar and Faeth (1971), Canada and Faeth (1975), and Kadota and Hiroyasu (1981), the general trends of which are shown in Figure 2. The observed minimum ambient pressures required for fully transient gasification for hydrocarbon fuels are in the range of 1.2 to 2 times the pure component critical pressure.

Note that at low pressures the droplet experiences an initial rise in temperature after injection into the hot environment but quickly reaches its steady-state or wet-bulb temperature. For near-critical pressures, the wet-bulb temperature and the rate of temperature rise of the drop both increase, and the transient heat-up period becomes longer while the steady-state period becomes shorter. Finally, for pressures substantially higher than the critical pressure of the pure liquid, the temperature history of the droplet becomes fully transient, and the drop heats up continuously through the critical state.

This unique transient nature of droplet vaporization at supercritical pres-

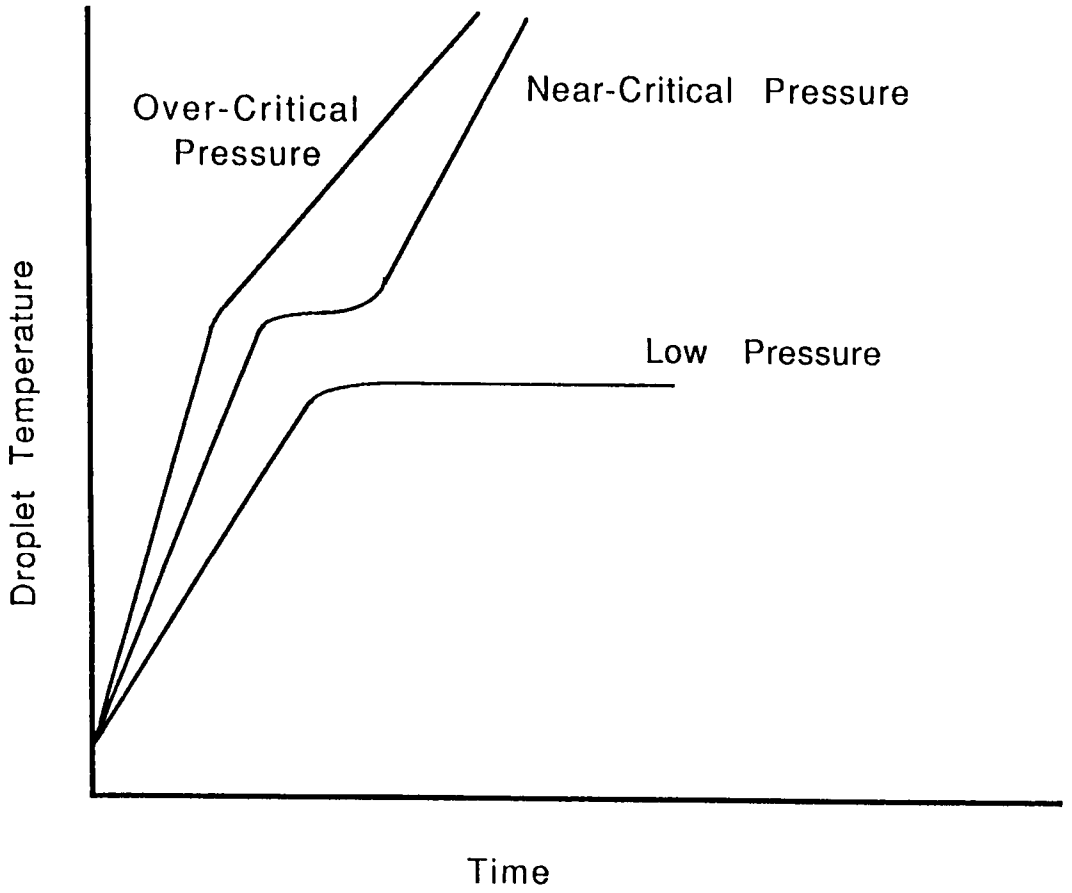

Figure 2. Qualitative droplet temperature histories at different pressures.

sures has yielded significant implications concerning the liquid-to-vapor transitional regime. Combs (1964), for instance, examined Wieber's analysis and concluded that if the drop heats through its critical temperature while retaining the bulk of its initial mass, it will undergo transition to a pocket of dense, supercritical fluid. He further inferred that, not propellant vaporization, but turbulent diffusion and mixing would control the ensuing combustion rate. Experimental validation of this proposition has yet to appear in the open literature since published work to date has been confined to thermocouple-suspended droplets under free or nonconvective conditions, thereby neglecting the liquid to supercritical fluid transition and breakup regime encountered by a free drop.

A more realistic evaluation of phase equilibrium at the surface and enthalpy required for vaporization was introduced by Manrique and Borman (1969). They considered solubility of ambient gas into the liquid, enforced thermodynamic equilibrium at the phase interface, and modeled real-gas behavior at high pressures with the Redlich-Kwong equation of state to obtain realistic values for the surface mole fractions. They also showed that the correct enthalpy of vaporization was not the latent heat of vaporization but the difference between the partial molar enthalpy in the vapor phase and the liquid phase for the vaporizing component, which they calculated from deviation equations based on the Redlich-Kwong equation of state. Calculations using these corrections were compared with predictions from a low-pressure model indicating that the low-pressure assumptions lead to large error with increasing pressure.

Since they performed a steady-state analysis, results could only be obtained below a certain pressure threshold as discussed in relation to Wieber's analysis and to the experimental results generalized in Figure 2. Manrique and Borman showed that this pressure threshold is the result of phase equilibruim requirements at the

droplet surface. For example, Figure 3 depicts a typical vapor-liquid phase equilibrium diagram for a binary system. For each isotherm, the upper portion of the curve corresponds to the liquid-phase concentration of the considered component, and the lower portion of the curve corresponds to the gas-phase concentration of this component. Note that there is a definite pressure for each isotherm at which the liquid and gas phase compositions become identical, and for those conditions outside the envelope given by the locus of these critical points, which is designated as the critical mixing line, the two phases become indistinguishable and steady-state conditions become unattainable. Manrique and Borman recognized that the critical mixing line, depicted in Figure 4, represented the threshold to fully transient behavior just as the pure component critical point did in the explanation given by Wieber.

For a physical interpretation, the phenomenon may be examined from consideration of surface heat transfer and evaporative cooling rates. If the instantaneous rate of surface heat transfer exceeds the instantaneous rate of evaporative cooling, due to the greatly reduced enthalpy of vaporization with increasing pressure, the droplet temperature will continually increase. Since the heat of vaporization vanishes when the liquid-vapor interface reaches the critical mixing temperature, all subsequent heat transfer results in sensible heating of the drop. This implies that once the surface reaches the critical mixing state, a wet-bulb (steady-state) condition is unattainable. The hypothesis has been further substantiated by the work of Rosner and Chang (1973) and Lazar and Faeth (1971).

Matlosz *et al.* (1972) conducted a nonconvective transient analysis using similar assumptions except for neglecting the dissolution of ambient gas into the liquid, but their experimental set-up included natural convection which was ignored in their model. Kadota and Hiroyasu (1976) have developed a global vaporization

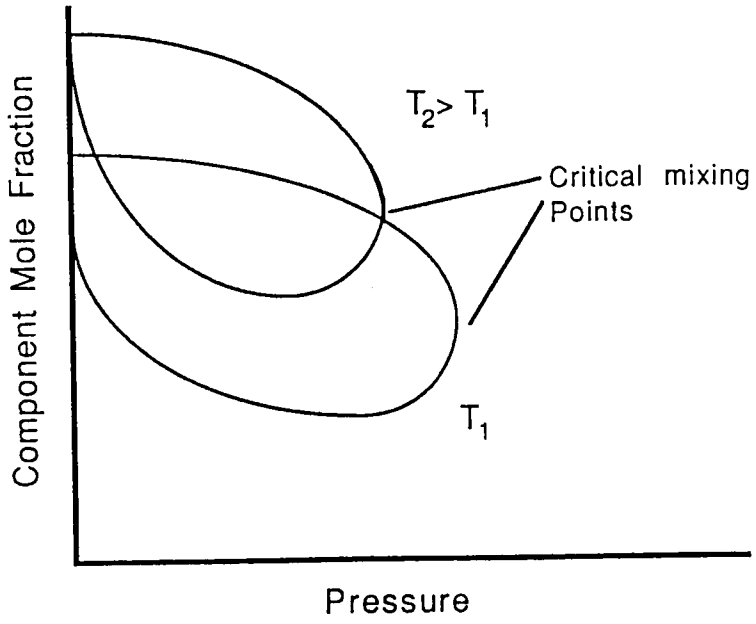

Figure 3. Schematic of typical vapor-liquid equilibria for a binary system.

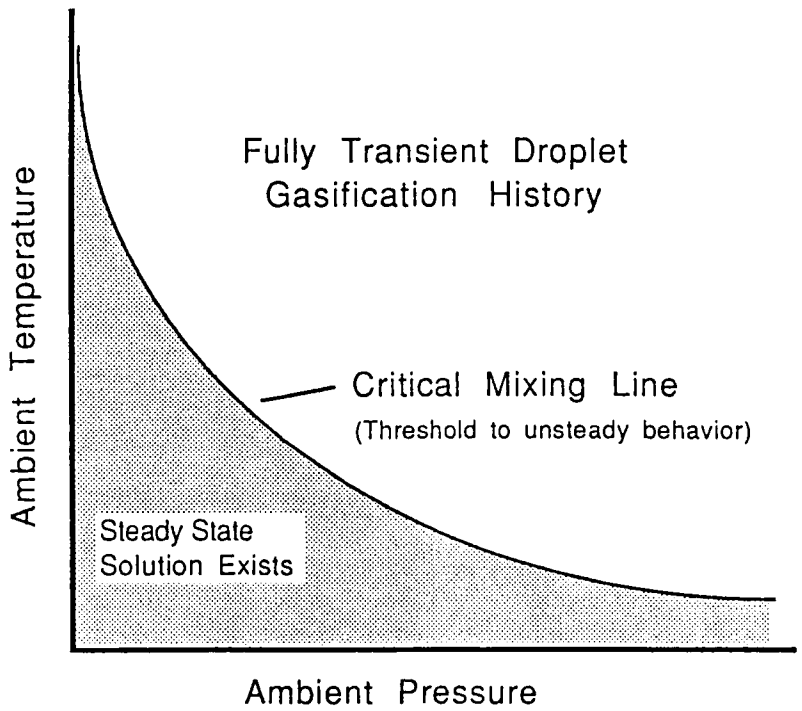

Figure 4. Schematic representing threshold to fully transient droplet gasification.

model with successful comparison between theory and experiment. They used the Redlich-Kwong phase equilibrium model with the assumption of no ambient gas absorption, employed the Redlich-Kwong deviation equations for the heat of vaporization, and corrected for high-pressure effects on the drop regression rate in a constant property, quasi-steady, stagnant film model with empirical corrections for natural convection. Excellent comparisons between theory and experiment were obtained. A similar model extended to encompass multicomponent systems considering forced convection, absorption of ambient gas, and diffusion and circulation within the drop has been presented by Jin and Borman (1985), although theoretical predictions were not compared with experimental results. More recently, Hsieh *et al.* (1988) have conducted a comprehensive numerical study of nonconvective, high-pressure droplet vaporization for multicomponent systems. They solved the complete, time-dependent conservation equations for both the liquid and gas phases with appropriate matching conditions at the surface in an attempt to encompass all high-pressure phenomena in a single calculation. Their calculations did not, however, consider droplet deformation and breakup nor supercritical vaporization once the droplet surface reached the critical mixing temperature. In addition, the computational effort is too encumbering for application to SF spray combustion modeling. Other recent contributions include the analyses by Umemura (1986) and Chang *et al.* (1988) on the supercritical combustion of a finite slab of fuel in which they show that the mutual diffusion coefficient vanishes at the critical-state interface implying that the vaporization rate attains a limiting finite magnitude for supercritical gasification. Their contributions should be of value in the formulation of future droplet gasification models valid from subcritical through critical-transition to supercritical conditions.

For practical combustors, secondary droplet atomization processes must also

be considered. In these environments the flow is turbulent with large velocity fluctuations which creates a pressure field over the drop and a shear stress at the phase boundary. These aerodynamic forces cause the drop to experience sudden and large accelerations and induce internal stresses which are resisted by the liquid surface tension. The competing tendencies between a deforming or tearing apart of the droplet and a retention of its form can be expressed quantitatively as the Weber number

$$We = \frac{\rho_p d_d \Delta U^2}{\sigma_p} \tag{2.1}$$

which represents the ratio of external aerodynamic pressure to the surface tension. Furthermore, a Reynolds number effect on atomization processes has been shown to be important leading to empirical correlation between these processes and the dimensionless Rabin number

$$Ra = \frac{We}{Re^{\frac{1}{2}}} \tag{2.2}$$

The general dynamic response of a suddenly accelerated droplet and the resulting atomization process is described by Rabin *et al.* (1960), Kogarko *et al.* (1971), Harper *et al.* (1971), and Harrje and Reardon (1972), and the different regimes of atomization are shown to correlate with a critical Weber number We_{crit} and a critical Rabin number Ra_{crit}. For Weber numbers below the critical value, the droplets do not breakup but retain their identity until they gasify or impact with another drop or the chamber surface. If the Weber number slightly exceeds its critical value, the droplet will undergo bag-type deformation and fragmentation. In this mode of disintigration, the center of the droplet is inflated in the downstream direction due to the windward side stagnation pressure. Eventually, the inflated central core breaks into a multitude of small droplets, and the outer rim is torn away into large

droplets. Finally, for Weber numbers much larger than the critical value such that the Rabin number exceeds its critical value, the drop will experience a stripping mode of disintegration in which unstable waves on the drop surface become strong enough for the periphery of the drop to be sheared off. The fragments removed from the drop in this way are extremely small and may be considered to vaporize instantaneously. Aerodynamic stripping can thus act as a very effective mode of vaporization. The critical Weber and Rabin have been roughly approximated by $We_{crit} \approx 20$ and $Ra_{crit} \approx 1$.

For typical rocket chambers, the conditions for initiating breakup can be exceeded rather easily, but the bag type breakup time scale is usually much longer than the chamber residence time (Harrje and Reardon, 1972). Thus, the stripping mode of atomization is of more pertinence to liquid rocket combustors and in particular to liquid rocket combustion instability where the frequency response of this process to acoustic oscillations may provide a Rayleigh type reinforcement mechanism. Campbell and Chadwick (1968) have also suggested that $Ra_{crit} \approx 10$ should be used as the breakup criteria in rocket combustion instability calculations since marginally short duration instabilty waves should not allow the process to proceed to full stripping.

To date, researchers have identified the unique thermodynamic phenomena associated with supercritical ambient pressures and have devised a theoretical basis for approaching high-pressure droplet vaporization modeling. What has also been shown to be of concern in the modeling of high-pressure spray combustors is drop deformation and breakup at near-critical conditions and the transitional regime from subcritical to supercritical gasification. Future comprehensive modeling codes for high-pressure combustors will require atomization and gasification submodels valid throughout the droplet lifetime, and experimental verification and calibration

will be essential. Therefore, extension of low-pressure correlations into the high-pressure regime is a practice that may be relinquished through the formulation of new relationships for dense-gas environments as experimental results become available. Alternatively, knowledge assimilated from this retrospective survey of past work can provide a foundation for formulating a physically plausible engineering model for current applications.

2.2 THE ROLE OF DROPLET GASIFICATION IN HIGH-FREQUENCY LIQUID ROCKET COMBUSTION INSTABILITY THEORY

Consideration of droplet gasification theory has yielded meaningful insight into Rayleigh-type mechanisms responsible for high-frequency liquid rocket combustion instability. Rayleigh-type mechanisms of combustion instability are based upon the criterion that if an oscillating energy or mass source within the flow has a component of its rate in phase with an acoustic density oscillation, the acoustic oscillation will be reinforced so long as the phase relationship is maintained (Toong, 1983). As vaporizing propellant drops can act as effective energy sources in the combustion chamber, assuming the evaporated propellant is burned instantaneously, the dynamic response of the droplet gasification process to oscillating acoustic excitations provides a governing mechanism for acoustic wave reinforcement which can be used to analyze combustion instability limits.

Such a theory was initially proposed by Priem and Guentert (1962) of which extended versions have become standard design tools for stability analysis (Harrje and Reardon, 1972). Certainly, the validity of the droplet gasification submodel is important in obtaining meaningful estimates of stability limits in these analyses,

and since most liquid rocket combustors operate at supercritical pressures, the ability of the submodel to display the correct frequency response characteristics of high-pressure droplet gasification would seem to play a central role in the accurate prediction of stability limits for these high-pressure combustors.

Investigations into the possible coupling between acoustic oscillations and the propellant vaporization process were initiated by Wieber and Mickelson (1960) who examined the vaporization of discrete n-octane droplets under a transverse acoustic velocity oscillation assuming the drops remained along the constant-pressure axis of the rocket chamber for the acoustic mode considered. Using a low-pressure vaporization model which neglected the thermal inertia of droplet heating, they found that the fluctuating vaporization rate provided a plausible process for acoustic wave amplification in support of resonant combustion; however, conclusive evidence was not presented.

Later, Heidmann and Wieber (1966) performed a more substantial analysis using a nonlinear, low-pressure vaporization theory considering droplet thermal inertia with the infinite thermal conductivity assumption (Priem and Heidmann, 1960), and realistic traveling, transverse-mode acoustic pressure and velocity oscillations were included. By repetitively injecting n-heptane droplets into the chamber at different time intervals and superimposing the results for an array of droplets undergoing vaporization at any instant, the vaporization response of the effective spray was obtained. From this analysis they determined a response factor to quantify the tendency for the vaporization process to couple with acoustic excitations with positive values being indicative of acoustic wave reinforcement and negative values indicating a damping effect. It was found that the response factor peaked at a value of about 0.6 – 0.9 in a frequency range of 400 – 1000 Hz and that the frequency response factor decreased to negative values at higher frequencies for

n-heptane droplets. Similar analysis for LOX droplets showed a shift to a higher frequency regime for the peak response factor factor and an absence of negative values of the response factor at the highest acoustic frequencies. Although their computations revealed peak positive response factors in the high-frequency range of experimentally observed instability, the magnitude of the calculated response factor was insufficiently large to account for nozzle losses and affirm propellant vaporization controlled instability.

More recent work has been conducted by Tong and Sirignano (1987, 1989) using the same array combination methodology as Heidmann and Wieber but with the employment of internal heat conduction and convection effects in their low-pressure droplet vaporization model. Results from their caculations for n-heptane droplets show that the existence of a thermal wave within the droplet affects the vaporization response to the acoustic excitations and that the corresponding response factors are sufficiently large to sustain instability according to the Rayleigh criterion. This appears to be the first conclusive theoretical basis for propellant vaporization as a rate-controlling feedback mechanism, although there will be continued uncertainty until there is credible experimental evidence.

None of the vaporization models utilized in the above studies, however, considered the high-pressure phenomena associated with practical liquid rocket combustors. As droplet gasification behavior at elevated pressures is substantially modified from low-pressure behavior, the inclusion of a realistic high-pressure gasification model in a similar analysis would seem warranted. The effects of stripping mode atomization might also be of importance in the instability process and should be investigated. Steps toward such studies are initiated in this work.

CHAPTER 3

THEORETICAL MODELING OF HIGH-PRESSURE DROPLET GASIFICATION

3.1 THEORETICAL FORMULATION OF TRANSPORT MODEL

3.1.1 Diffusion Controlled Transport Model

Before examining the peculiarities of the high-pressure, discrete droplet gasification model formulation, a clarification of terminology and some qualifications for the assumptions used are in order. Researchers have conventionally differentiated droplet combustion from droplet vaporization by the presence of a flame envelope around the drop; however, it has been suggested (McCreath and Chigier, 1973; Faeth, 1979; Law, 1982) that since the detailed transport mechanisms in the two cases are qualitatively similar, the combusting drop can be studied from the viewpoint of a vaporizing drop which sees the flame as an effective hot ambient environment. Alternatively, if the chemical reaction times are long compared with the time for the vapor to be swept away from the vicinity of the droplet yet short compared with the total droplet lifetime, nonreactive droplet vaporization theory provides a valid description of the process (Harrje and Reardon, 1972). In fact, some combustor flows have such dense sprays and/or are so violently turbulent that the presence of envelope flames seems intuitively unlikely. This supposition is supported by experimental evidence and the group combustion theory of Chiu *et al.* (1978) in which the major combustion mode for a typical spray burner is external group combustion where the flame is located at some radial distance away from the spray boundary.

Such thinking has led many workers in spray combustion modeling to the con-

venient assumption that envelope flames are never present and that drops vaporize and then combust in turbulent eddys in the gas phase. While not appropriate within particular regions of the combustor, the method does provide a simple ad hoc engineering approach.

Indeed, through similar reasoning the terminology of droplet gasification can pertain to droplet vaporization in both combusting and noncombusting environments depending upon how the ambiance is modeled. For example, gasification can occur for normal combustion in which the fuel droplet vaporizes and oxidizes in an envelope flame or for conjugate combustion in which an oxidant droplet vaporizes and combusts with fuel vapor in an envelope flame (Chiu, 1986). It is concievable, in addition, that for sufficiently high pressures a liquid drop might undergo vigorous stripping atomization due to reduced surface tension for the higher drop temperatures attained or experience transition to a supercritical fluid and behave as a dense gas, and the terminology of droplet gasification may be loosely applied for these cases. In this work, therefore, droplet gasification is considered more general representative terminology for the processes of pure vaporization, normal or conjugate combustion driven vaporization, aerodynamic stripping vaporization, and flash supercritical transition. Furthermore, vaporizing or combusting drops are modeled as identical processes under the assumption that an envelope flame can be simulated as an effective hot ambient environment. The actual validity and realm of application of this assumption is left to future studies.

At atmospheric pressures, quasi-steady film theory is known to accurately predict droplet life historys over a wide range of ambient temperatures, convective conditions, and drop sizes. Extension of the fundamental model to the high-pressure case seems, therefore, a valid proposition provided adequate modifications are incorporated into the theory. Several investigators have taken this approach (Savery

and Borman, 1970; Kadota and Hiroyasu, 1976; Jin and Borman, 1985) using the stagnant film methodology, and a similar approach is made here, although the formulation methodology employed follows the conventional manner (Faeth, 1977; Faeth, 1983; Mao *et al.*, 1980) yielding a modified governing system of equations due to the inclusion of bulk thermal expansion and surface regression effects. The resulting governing ODE's are also forced into a form suitable for efficient numerical solution. The basic assumptions incorporated in this general model are as follow:

(1) The droplet is at uniform temperature due to rapid internal mixing.

(2) Transport can be modeled as a spherically symmetric, diffusion controlled process which can be corrected for convective effects using global steady-state heat and mass transfer correlations.

(3) Empirical drag coefficients for the low-pressure case are assumed to apply in the high-pressure case.

(4) Film thermophysical properties are based on weight-averaged temperature and composition between the surface and ambient.

(5) Pressure effects on the thermophysical properties are considered.

(6) Propellant vapor accumulation effects in the film region are neglected for forced convective conditions. The mass and thermal film thickness are assumed to be fully developed at time zero in this case.

(7) Surface regression and counter-diffusion effects and bulk thermal expansion of the drop are considered.

(8) High-pressure, thermodynamic phase equilibrium including ambient gas solubility is considered.

(9) The liquid drop consists of a single component with dissolved ambient gases confined to a thin layer near the surface.

The transport processes occurring during the gasification process are represented in Figure 5. Since the drop may be either liquid fuel or oxidant and since liquid propulsion applications are of primary emphasis, the drop substance will be generically designated as propellant. In the schematic, the propellant vapor flows out from the surface while ambient gas flows in toward the drop during the gasification process. By Fick's law of mass diffusion, the mass flux of the propellant in the gas phase at any radius relative to the drop center may be written as

$$\dot{m}_p'' = y_p \dot{m}'' - \rho^v \mathcal{D} \nabla y_p \tag{3.1}$$

If an effective two-component system of propellant drop and ambient gas is considered where the effective ambient gas may actually be a multicomponent mixture of gases then $\dot{m}'' = \dot{m}_p'' + \dot{m}_a''$, and the mass diffusion equation becomes

$$\dot{m}_p'' - y_p(\dot{m}_p'' + \dot{m}_a'') = -\rho^v \mathcal{D} \nabla y_p \tag{3.2}$$

Compensation for an ambient gas mixture modeled as an effective pure component gas can be made through evaluation of the gas-phase thermophysical properties and the vapor-liquid equilibria concentrations. Surface regression and counter-diffusion effects may be combined in a single variable by defining

$$\varsigma = \frac{\dot{m}_a''}{\dot{m}_p''} = \frac{\rho_a^v v_a}{\rho_p^v v_p} \tag{3.3}$$

Then equation (3.2) may be expressed as

$$\dot{m}_p'' = -\frac{\rho^v \mathcal{D} \nabla y_p}{[1 - y_p(1 + \varsigma)]} \tag{3.4}$$

The gradient of propellant vapor concentration in the gas phase is conveniently handled through the engineering concept of a mass transfer coefficient. This concept is of practical usefulness since empirical convection corrections are primarily

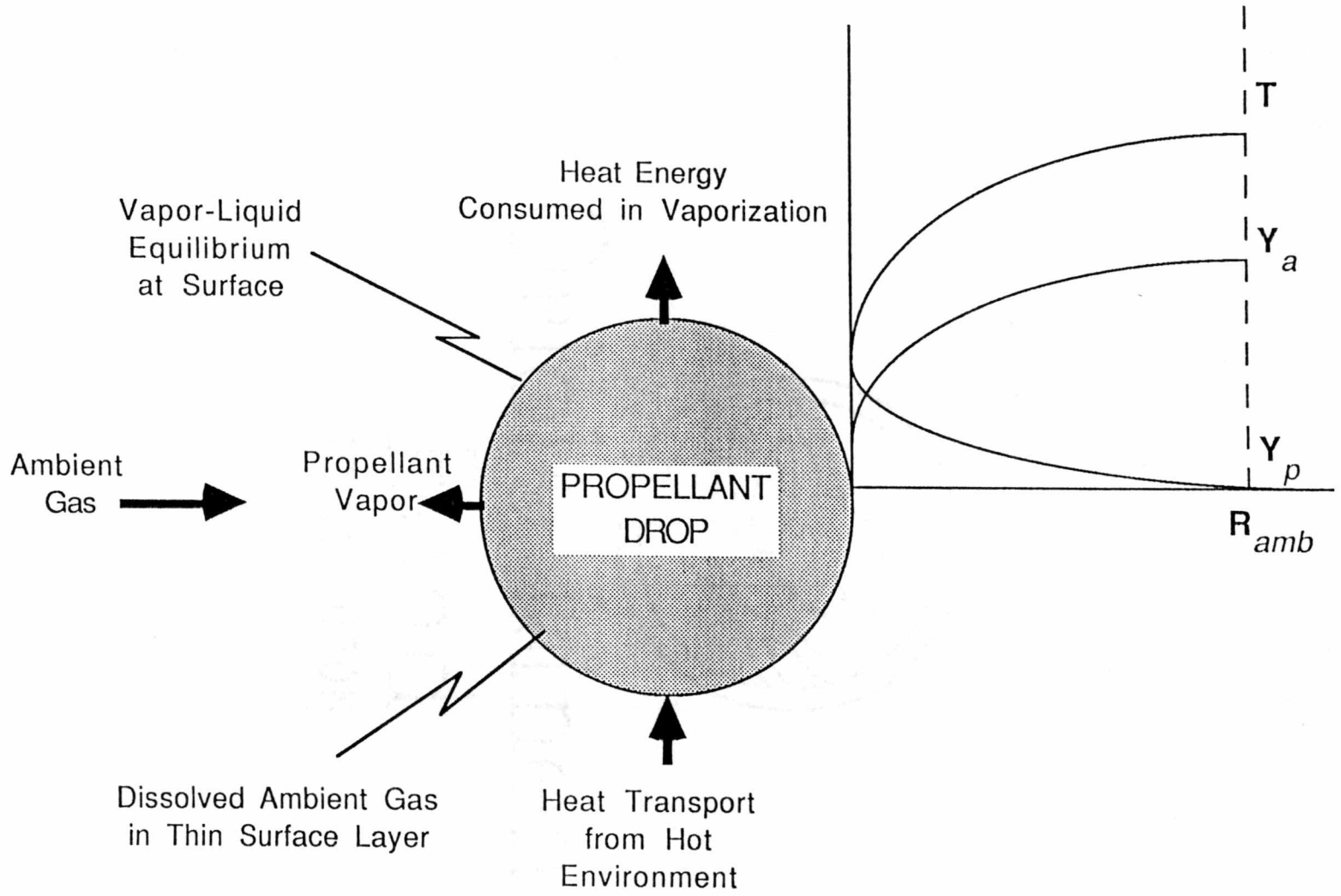

Figure 5. Schematic of transport processes during gasification of a propellant droplet.

formulated in terms of the Sherwood number and the Reynolds number. The mass transfer coefficient is defined by the relation

$$\rho^v \mathcal{D} \nabla y_p = k(y_{p_\infty} - y_p) \tag{3.5}$$

Substitution into equation (3.4) and evaluation at the drop surface gives an equation for the propellant gasification flux

$$\dot{m}_p'' = \frac{k(y_{p_s} - y_{p_\infty})}{[1 - y_{p_s}(1+\varsigma)]} \tag{3.6}$$

An expression for the instantaneous time derivative of the droplet mass follows directly from equation (3.6) with the introduction of the drop surface area

$$\frac{dm_d}{dt} = -\dot{m}_p'' A_s = -\pi d_d^2 \frac{k(y_{p_s} - y_{p_\infty})}{[1 - y_{p_s}(1+\varsigma)]} \tag{3.7}$$

Further use will now be made of equation (3.4). By recognizing that $\dot{m}_p'' = \rho_p^v v_p$, rearranging the equation in terms of v_p, and evaluating at the droplet surface, one obtains

$$v_{p_s} = \frac{\rho_s^v \mathcal{D}_s}{\rho_{p_s}^v} \frac{\nabla y_p|_s}{[y_{p_s}(1+\varsigma) - 1]} \tag{3.8}$$

Following the Spalding approach, a parameter b can be defined as

$$b = \frac{y_p}{[y_{p_s}(1+\varsigma) - 1]} \tag{3.9}$$

such that with spherical symmetry enforced equation (3.8) is transformed in terms of the new dependent variable b

$$v_{p_s} = \frac{\rho_s^v \mathcal{D}_s}{\rho_{p_s}^v} \nabla b \Big|_s = \frac{\rho_s^v \mathcal{D}_s}{\rho_{p_s}^v} \frac{db}{dr}\Big|_s \tag{3.10}$$

Putting equation (3.10) aside for the moment, the gas-phase fuel species equation with spherical symmetry and no chemical reaction may be reduced to

$$r^2 \rho^v v \frac{dy_p}{dr} = \frac{d}{dr}\left[r^2 \rho \mathcal{D} \frac{dy_p}{dr}\right] \tag{3.11}$$

If equation (3.9) is substituted into equation (3.11) which is then integrated once and evaluated at the drop surface utilizing equation (3.10), and overall continuity ($r^2\rho^v v = r_s^2\rho_s^v v_s$) is enforced, the result is

$$r_s^2\rho_s^v v_s\left[b - b_s + \frac{1}{1+\varsigma}\right] = r^2\rho^v \mathcal{D}\frac{db}{dr} \tag{3.12}$$

Assuming $\rho^v \mathcal{D} = \rho_s^v \mathcal{D}_s$, separating variables, and integrating again from the surface, through the film thickness, and to ambient conditions produces

$$v_s = \frac{r_{amb}}{r_s(r_{amb} - r_s)}\mathcal{D}_s \ln\left[1 + (1+\varsigma)(b_\infty - b_s)\right] \tag{3.13}$$

Note that r_{amb} is not infinity – the usual assumption for a quasi-steady analysis. Here the instantaneous film thickness can be determined from gas-phase mass conservation so that the amount of propellant vapor in the film thickness cannot exceed the total vaporized propellant mass, assuming the ambient has zero propellant vapor concentration. Analysis for film thickness determination will be presented in abeyance. Continuing with the current development, a mass transfer driving potential may be defined as

$$B = b_\infty - b_s = \frac{y_{p_s} - y_{p_\infty}}{[1 - y_{p_s}(1+\varsigma)]} \tag{3.14}$$

so that equation (3.13) becomes

$$v_s = \frac{r_{amb}}{r_s(r_{amb} - r_s)}\mathcal{D}_s \ln\left[1 + (1+\varsigma)B\right] \tag{3.15}$$

Noting that $\dot{m}'' = \frac{\dot{m}}{4\pi r_s^2} = \rho_s^v v_s$ and substituting for v_s from equation (3.13) yields another expression for the mass gasification flux of the propellant.

$$\dot{m}_p'' = \frac{r_{amb}}{r_s(r_{amb} - r_s)}\rho_s^v \mathcal{D}_s \frac{\ln\left[1 + (1+\varsigma)B\right]}{(1+\varsigma)} \tag{3.16}$$

And an additional equation for the instantaneous droplet mass time derivative may also be obtained from equation (3.16)

$$\frac{dm_d}{dt} = -\dot{m}_p'' A_s = -4\pi \left(\frac{d_d r_{amb}}{2r_{amb} - d_d} \right) \rho_s^v \mathcal{D}_s \frac{\ln\left[1 + (1+\varsigma)B\right]}{(1+\varsigma)} \tag{3.17}$$

By combining equation (3.17) with equation (3.7), the Sherwood number is obtained for the nonconvective flow case ($Re = 0$)

$$Sh_{Re=0} = \left. \frac{k d_d}{\rho^v \mathcal{D}} \right|_{Re=0} = \left(\frac{r_{amb}}{r_{amb} - \frac{d_d}{2}} \right) \frac{2\ln\left[1 + (1+\varsigma)B\right]}{(1+\varsigma)B} \tag{3.18}$$

Now ς, recall, was defined as the ratio of the inwardly flowing ambient gas mass flux to the outwardly flowing propellant vapor evaluated at the drop surface. It is clear then that ς represents the surface regression effect since the inwardly moving droplet surface leaves a volume formerly occupied by liquid which must be replace by gaseous mass. Also, since the liquid and and gas phase densities can become of comparable magnitude at near-critical conditions and the increasing drop temperature causes bulk thermal expansion of the droplet, the surface regression cannot be neglected and may be evaluated as

$$\varsigma = \left. \frac{\dot{m}_a''}{\dot{m}_p''} \right|_s = \left. \frac{\dot{m}_a}{\dot{m}_p} \right|_s = -\frac{\rho_{a_s}^v \frac{dV_d}{dt}}{\frac{d(\rho_p V_d)}{dt}} = -\frac{\rho_{a_s}^v \frac{dV_d}{dt}}{\rho_p \frac{dV_d}{dt} + V_d \frac{d\rho_p}{dt}} \tag{3.19}$$

Eliminating V_d for d_d gives

$$\varsigma = -\frac{\rho_s^v (1 - y_{p_s}) \frac{dd_d^3}{dt}}{\rho_p \frac{dd_d^3}{dt} + d_d^3 \frac{d\rho_p}{dt}} \tag{3.20}$$

which, upon retention of the propellant density temperature dependence and further manipulation, becomes

$$\varsigma = -\rho_s^v (1 - y_{p_s}) \left[\rho_p + \frac{d_d}{3} \left(\frac{d\rho_p}{dT_d} \frac{dT_d}{dt} \Big/ \frac{dd_d}{dt} \right) \right]^{-1} \tag{3.21}$$

Attention may now be turned to the gas-phase energy equation which for spherical symmetry and no chemical reaction takes the form

$$r^2 \rho^v v C_p \frac{dT}{dr} = \frac{d}{dr}\left[\lambda r^2 \frac{dT}{dr}\right] \tag{3.22}$$

Integrating once with the surface boundary condition $\lambda \frac{dT}{dr} = h(T_\infty - T_d)$, enforcing continuity, and integrating once more from the drop surface, through the film thickness, and to ambient conditions, where r_{amb} is finite and is assumed identical to the concentration film thickness, produces the expression

$$\frac{\dot{m}'' C_p}{h} + 1 = \left[1 + (1+\varsigma)B\right]^{Le^{-1}} \tag{3.23}$$

Since $\dot{m}'' = \rho_s^v v_s$ and v_s is known explicitly from equation (3.15), equation (3.23) can be formulated into a Nusselt number for the nonconvective case ($Re = 0$)

$$Nu_{Re=0} = \frac{h d_d}{\lambda}\bigg|_{Re=0} = \left(\frac{r_{amb}}{r_{amb} - \frac{d_d}{2}}\right) \frac{2 \ln\left[1 + (1+\varsigma)B\right]^{Le^{-1}}}{\left[1 + (1+\varsigma)B\right]^{Le^{-1}} - 1} \tag{3.24}$$

Thus far, the analysis has been concerned with the gas-phase transport only. The transient heating of the drop must be considered, however, since the time to reach a steady-state drop temperature may be of significant duration compared to the overall gasification time, or as noted for the high-pressure case, the drop might never even attain a steady wet-bulb temperature during its lifetime. It is also necessary to determine the time varying drop size so that aerodynamic forces on the drop are known for use in a force balance on the individual drop.

In considering energy transport in the liquid phase, it is possible to model the spatial variation with a finite difference methodology, but computing time would be exessive. A simpler engineering approach is to assume the drop temperature and properties have spatial uniformity but temporal variance. An energy balance on the drop, neglecting radiation heat transfer, gives

$$m_d C_{p_p} \frac{dT_d}{dt} = \pi d_d^2 h (T_\infty - T_d) + h_{vap} \frac{dm_d}{dt} \tag{3.25}$$

Dividing through by $m_d C_{p_p}$ yields an expression for the instantaneous drop temperature time derivative which couples the liquid-phase and and gas-phase solutions.

$$\frac{dT_d}{dt} = \frac{\pi d_d^2 h}{m_d C_{p_p}}(T_\infty - T_d) + \frac{h_{vap}}{m_d C_{p_p}}\frac{dm_d}{dt} \tag{3.26}$$

Furthermore, a liquid-phase mass balance on the drop may be written as

$$\frac{dm_d}{dt} = \frac{d(\rho_p V_d)}{dt} = \rho_p \frac{dV_d}{dt} + V_d \frac{d\rho_p}{dt} \tag{3.27}$$

This equation can be manipulated to yield the instantaneous drop diameter time derivative which is also coupled with the gas-phase solutions

$$\frac{dd_d}{dt} = \frac{2}{\pi \rho_p d_d^2}\frac{dm_d}{dt} - \frac{1}{3}\frac{d_d}{\rho_p}\frac{d\rho_p}{dT_d}\frac{dT_d}{dt} \tag{3.28}$$

And substituting from equation (3.26) into equation (3.28) gives

$$\frac{dd_d}{dt} = \frac{2}{\pi \rho_p d_d^2}\frac{dm_d}{dt} - \frac{1}{3}\frac{\pi d_d^3 h(T_\infty - T_d)}{m_d C_{p_p}}\frac{1}{\rho_p}\frac{d\rho_p}{dT_d} - \frac{1}{3}\frac{d_d h_{vap}}{m_d C_{p_p}}\frac{1}{\rho_p}\frac{d\rho_p}{dT_d}\frac{dm_d}{dt} \tag{3.29}$$

The heat and mass transport relations have now been formulated to describe the drop history in terms of three coupled, nonlinear, first-order ordinary differential equations for the three dependent variables T_d, m_d, and d_d as given by equations (3.26), (3.17), and (3.29) with three additional coupling parameters ς, $Sh|_{Re=0}$, and $Nu|_{Re=0}$ given by equations (3.21), (3.18), (3.24), respectively. For numerical solution it is advantageous to force the system to three first-order differential equations each containing only one time derivative term. The procedure is algebraically tedious and will only be described.

First, solve equation (3.7) for ς and equate the result to the right hand side of equation (3.21) yielding

$$\left(\frac{1 - y_{p_s}}{y_{p_s}}\right) + \frac{\pi d_d^2 k}{\frac{dm_d}{dt}}\left(\frac{y_{p_s} - y_{p_\infty}}{y_{p_s}}\right) = -\frac{\rho_s^v (1 - y_{p_s})}{\left[\rho_p + \frac{d_d}{3}\left(\frac{d\rho_p}{dT_d}\frac{dT_d}{dt} \Big/ \frac{dd_d}{dt}\right)\right]} \tag{3.30}$$

Multiplying through by the denominator of the RHS and by $\frac{dm_d}{dt}\frac{dd_d}{dt}$ and then substituting for $\frac{dd_d}{dt}$ from equation (3.29) and $\frac{dT_d}{dt}$ from equation (3.26) produces an equation which contains the time derivative of droplet mass only since all other time derivatives have been eliminated. Gathering like terms and simplifying gives a quadratic equation for $\frac{dm_d}{dt}$ where the constant term is identically zero.

$$A^*\left(\frac{dm_d}{dt}\right)^2 - B^*\left(\frac{dm_d}{dt}\right) = 0 \tag{3.31}$$

where

$$A^* = \frac{2}{\pi d_d^2}\left[\left(\frac{1-y_{p_s}}{y_{p_s}}\right) + \frac{\rho_s^v}{\rho_p}\left(1-y_{p_s}\right)\right] - \frac{1}{3}\frac{h_{vap}d_d}{m_d C_{p_p}}\frac{d\rho_p}{dT_d}\left[\frac{\rho_s^v}{\rho_p}(1-y_{p_s})\right] \tag{3.32}$$

and

$$B^* = -2k\left[\frac{y_{p_s}-y_{p_\infty}}{y_{p_s}}\right] + \frac{1}{3}\frac{\pi d_d^3 h(T_\infty - T_d)}{m_d C_{p_p}}\frac{d\rho_p}{dT_d}\left[\frac{\rho_s^v}{\rho_p}(1-y_{p_s})\right] \tag{3.33}$$

Since the trivial root is physically insignificant, the only meaningful real, nonzero root is given by

$$\frac{dm_d}{dt} = \frac{B^*}{A^*} \tag{3.34}$$

If this result is substituted into equation (3.7) which is then solved for ς, a time derivative free expression for the surface regression parameter is derived

$$\varsigma = \left(\frac{1-y_{p_s}}{y_{p_s}}\right) + \pi d_d^2 k\frac{A^*}{B^*}\left(\frac{y_{p_s}-y_{p_\infty}}{y_{p_s}}\right) \tag{3.35}$$

Equation (3.35) also implies that equations (3.18) and (3.24) for the Sherwood and Nusselt numbers become time derivative free. In addition, substitution of equation (3.34) into equations (3.26) and (3.29) yields the desired governing system in the

form of three first-order differential equations each containing only one time derivative. These equations remain, however, strongly coupled and strongly nonlinear. The new form of the governing system follows:

$$\frac{dm_d}{dt} = \frac{B^*}{A^*} \tag{3.36}$$

$$\frac{dd_d}{dt} = \frac{2}{\pi\rho_p d_d^2}\frac{B^*}{A^*} - \frac{1}{3}\frac{\pi d_d^3 h(T_\infty - T_d)}{m_d C_{p_p}}\frac{1}{\rho_p}\frac{d\rho_p}{dT_d} - \frac{1}{3}\frac{d_d h_{vap}}{m_d C_{p_p}}\frac{1}{\rho_p}\frac{d\rho_p}{dT_d}\frac{B^*}{A^*} \tag{3.37}$$

$$\frac{dT_d}{dt} = \frac{\pi d_d^2 h}{m_d C_{p_p}}(T_\infty - T_d) + \frac{h_{vap}}{m_d C_{p_p}}\frac{B^*}{A^*} \tag{3.38}$$

where A^*, B^*, and ς are given by equations (3.32), (3.33), and (3.35), respectively, and k and h are obtained from the simultaneous solution of the analytic equations (3.18) and (3.24) assuming r_{amb} is known. Up to this point, however, evaluation of r_{amb} has been avoided in the analysis. Special consideration is now devoted to the instantaneous film thickness.

If r_{amb} is taken as approaching infinity, as is the typical quasi-steady assumption, the preceedingly derived governing system of equations may be solved numerically without the development of an additional expression for the instantaneous film thickness. There is an innate error for the nonconvective case in the assumption of an infinite film thickness at time zero, however. In actuality, there is a relaxation time before the fuel vapor molecules can move far away from the drop. Figure 6, for example, illustrates representative time dependent propellant vapor concentration profiles as gasification proceeds. If r_{amb} is assumed to approach infinity at time zero, then some error can be incurred for long starting transients.

To avoid these deficiencies at low pressures, Law *et al.* (1980) enforced transient global continuity for the propellant and formulated an integral expression for r_{amb}

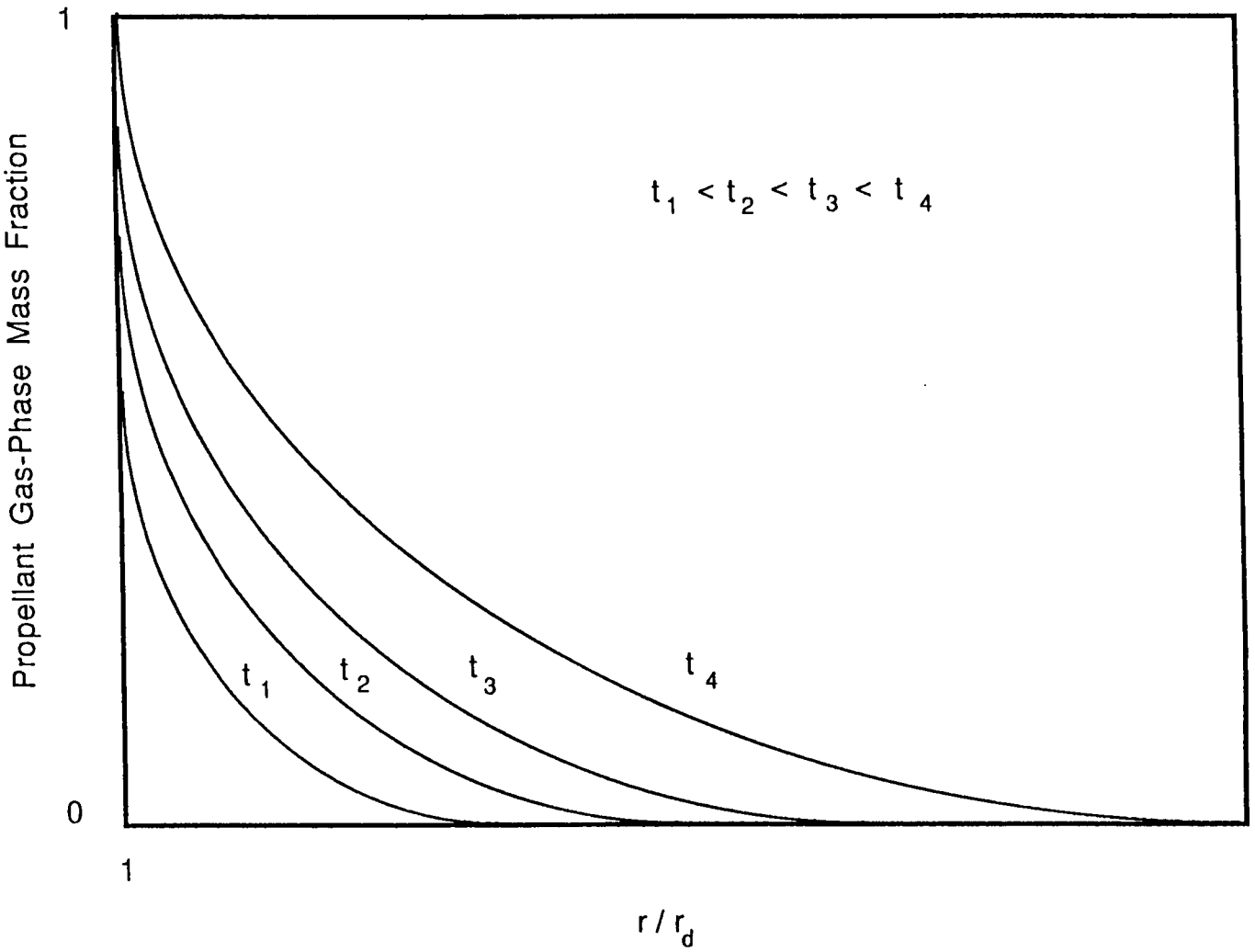

Figure 6. Representative time dependent propellant vapor concentration profiles as gasification proceeds.

as a function of the instantaneous droplet size. This approach may also be applied at high pressures to account for the diffusion relaxation time. An integral expression can be formulated and then integrated to examine the tractability of including the film growth in the mathematical analysis. To assure total conservation of propellant in the system, global continuity implies that the rate of change of the droplet mass equals the negative of the rate of change of the propellant vapor in the gas phase.

$$\frac{d}{dt}\left\{\frac{4\pi}{3}r_d^3\rho_p\right\} = -\frac{d}{dt}\left\{\int_{r_d}^{r_{amb}} 4\pi r^2\left(\rho^v y_p - \rho_\infty y_{p_\infty}\right) dr\right\} \tag{3.39}$$

Implying that

$$\frac{4\pi}{3}r_d^3\rho_p + \int_{r_d}^{r_{amb}} 4\pi r^2\left(\rho^v y_p - \rho_\infty y_{p_\infty}\right) dr = \frac{4\pi}{3}r_{d_0}^3\rho_{p_0} \tag{3.40}$$

Simplifying further gives

$$\int_{r_d}^{r_{amb}} 4\pi r^2\left(\rho^v y_p - \rho_\infty y_{p_\infty}\right) dr = \frac{4\pi}{3}[r_{d_0}^3\rho_{p_0} - r_d^3\rho_p] \tag{3.41}$$

Equation (3.41) simply means that the instantaneous mass of propellant vapor in the gas phase in excess of ambient conditions is equal to the mass of propellant evaporated from the drop from time zero. To perform the necessary integration in equation (3.41), the gas-phase propellant mass fraction y_p must be expressed as a function of r. This may be accomplished by first integrating equation (3.12) from radius r to ambient conditions and introducing the mass transfer driving potential B to obtain

$$b = b_s - \frac{1}{1+\zeta} + \left(B + \frac{1}{1+\zeta}\right)\exp\left\{\frac{r_s^2 v_s}{\mathcal{D}_s}\left(\frac{1}{r_{amb}} - \frac{1}{r}\right)\right\} \tag{3.42}$$

Utilizing the definition of b from equation (3.9) and substituting for $v_s/\mathcal{D}_s$ from equation (3.15) gives a spatial expression for the propellant concentration in the

gas phase

$$y_p = \frac{1}{1+\varsigma} + \left(y_{p_\infty} - \frac{1}{1+\varsigma}\right) \exp\left\{\left(\frac{r_d}{r_{amb} - r_d}\right) \ln\left[1 + (1+\varsigma)B\right]\right\}$$
$$\exp\left\{\left(\frac{r_d r_{amb}}{r_d - r_{amb}}\right) \ln\left[1 + (1+\varsigma)B\right] \frac{1}{r}\right\} \quad (3.43)$$

If equation (3.43) is substituted into equation (3.41) and the trivial integrations are performed, the resulting equation containing one unevaluated integral is

$$\int_{r_d}^{r_{amb}} r^2 \exp\left\{\left(\frac{r_d r_{amb}}{r_d - r_{amb}}\right) \frac{\ln\left[1 + (1+\varsigma)B\right]}{r}\right\} dr$$
$$= \frac{1}{3} \frac{\exp\left\{\left(\frac{r_d}{r_d - r_{amb}}\right) \ln\left[1 + (1+\varsigma)B\right]\right\}}{\rho^v \left(y_{p_\infty} - \frac{1}{1+\varsigma}\right)}$$
$$\left[(r_{amb}^3 - r_d^3)\left(\rho_\infty y_{p_\infty} - \frac{\rho^v}{1+\varsigma}\right) + (r_{d_0}^3 \rho_{p_0} - r_d^3 \rho_p)\right] \quad (3.44)$$

The integral in equation (3.44) is of the form $\int r^2 e^{a/r}\, dr$ where a is a constant, and it cannot be evaluated analytically. The integration may be performed in terms of an infinite series, though. Two integrations by parts, an integration by substitution, and the use of integral tables give an antiderivative of the form

$$\int r^2 e^{\frac{a}{r}}\, dr = \frac{r^3}{3} e^{\frac{a}{r}} + \frac{ar^2}{6} e^{\frac{a}{r}} + \frac{a^2 r}{6} e^{\frac{a}{r}} - \frac{a^3}{6} \ln \frac{a}{r}$$
$$-\left\{\frac{a^4}{6 \cdot 1! r} + \frac{a^5}{12 \cdot 2! r^2} + \frac{a^6}{18 \cdot 3! r^3} + \ldots\right\} \quad (3.45)$$

Employing this result in equation (3.44) with evaluation at the limits and algebraic manipulation produces a nonlinear equation for the ambient film radius r_{amb}.

$$\left[\frac{r^3}{3} e^{\frac{a}{r}} + \frac{ar^2}{6} e^{\frac{a}{r}} + \frac{a^2 r}{6} e^{\frac{a}{r}} - \frac{a^3}{6} \ln \frac{a}{r} - \left\{\frac{a^4}{6 \cdot 1! r} + \frac{a^5}{12 \cdot 2! r^2} + \frac{a^6}{18 \cdot 3! r^3} + \ldots\right\}\right]_{r_d}^{r_{amb}}$$
$$= \frac{e^{a/r_{amb}}}{3} \frac{(r_{amb}^3 - r_d^3)\left(\rho_\infty y_{p_\infty} - \frac{\rho^v}{1+\varsigma}\right) + (r_{d_0}^3 \rho_{p_0} - r_d^3 \rho_p)}{\rho^v \left(y_{p_\infty} - \frac{1}{1+\varsigma}\right)} \quad (3.46)$$

Note that equation (3.46) is coupled to equations (3.18) and (3.24) through the surface regression parameter given by equation (3.35). Therefore, these equations

must be solved simultaneously. Equation (3.46) also contains an infinite series complicating the matter greatly. The series can be truncated after a finite number of terms since the factorial driven denominator will eventually override the exponential in the numerator, but the number of terms needed to make the truncation error small may be unrealistically large for practical application. Neglect of the transient growth of the film thickness is, therefore, a typical simplification to the mathematical analysis, and it is a reasonable assumption for forced convection.

At this point the formulated equations are strictly applicable to stagnant, nonconvective droplet vaporization only. If steady-state heat and mass transfer correlations are considered valid in the quasi-steady case, however, convective effects can be introduced as multiplicative correction factors for the nonconvective Nusselt and Sherwood numbers. For natural convection, the Ranz/Marshall correlation is utilized. For forced convection, the Ranz/Marshall or Frossling correlations are conventionally adopted, but they are not applicable at low Reynolds numbers. The best forced-convective correlation available which is valid at both low and high Reynolds numbers appears to be a synthesized version of the Frossling correlation and an asymptotic analysis for creeping flow as proposed by Faeth (1977). The convective corrections are of the form

$$\frac{(Nu \text{ or } Sh)}{(Nu \text{ or } Sh)_{Re=0}} = \begin{cases} 1 + \dfrac{0.278 Re^{\frac{1}{2}} (Pr \text{ or } Sc)^{\frac{1}{3}}}{\left\{1+1.232/[Re(Pr \text{ or } Sc)^{\frac{4}{3}}]\right\}^{\frac{1}{2}}} & ; \begin{matrix} forced \\ convection \end{matrix} \\ 1 + 0.3 Gr^{\frac{1}{4}} (Pr \text{ or } Sc)^{\frac{1}{3}} & ; \begin{matrix} natural \\ convection \end{matrix} \end{cases} \tag{3.47}$$

Considering the more practical case of forced convection and applying equation (3.47) as a convective mass transfer correction with the substitution for $Sh_{Re=0}$ made from equation (3.18) gives the Sherwood number for forced convection

$$Sh = \frac{k d_d}{\rho \mathcal{D}} = \left(\frac{r_{amb}}{r_{amb} - \frac{d_d}{2}} \right) \frac{2 \ln \left[1 + (1+\varsigma)B\right]}{(1+\varsigma)B} \left[1 + \frac{0.278 Re^{\frac{1}{2}} Sc^{\frac{1}{3}}}{\left\{1 + 1.232/[ReSc^{\frac{4}{3}}]\right\}^{\frac{1}{2}}} \right] \tag{3.48}$$

Furthermore, applying equation (3.47) as a convective heat transfer correction with substitution for $Nu_{Re=0}$ made from equation (3.24) gives the Nusselt number for forced convection

$$Nu = \frac{hd_d}{\lambda} = \left(\frac{r_{amb}}{r_{amb} - \frac{d_d}{2}}\right) \frac{2\ln\left[1 + (1+\varsigma)B\right]^{Le^{-1}}}{\left[1 + (1+\varsigma)B\right]^{Le^{-1}} - 1} \left[1 + \frac{0.278 Re^{\frac{1}{2}} Pr^{\frac{1}{3}}}{\left\{1 + 1.232/[RePr^{\frac{4}{3}}]\right\}^{\frac{1}{2}}}\right] \quad (3.49)$$

Equations (3.48) and (3.49) replace equations (3.18) and (3.24) in the gas-phase transport solution for forced convective conditions. Although the correlations were developed for steady-state analyses, they are assumed to apply here under transient conditions. While the development has been illustrated for forced convection, the procedure for natural convection follows in a similar manner where the empirical correlation in terms of the Grashof number is utilized.

The governing system of equations derived to this point are strongly coupled requiring extensive iterations and computational time. This is disadvantageous for a submodel used in a large CFD code which is composed of several physical submodel routines and primary flow-field algorithms. Relaxation of assumptions used in the general model may be attempted to simplify the governing equations and reduce computational effort without unduly invalidating the model.

One possible relaxation in the general model is to assume the initial diffusional starting transient is small and take $r_{amb} \rightarrow \infty$ from time zero. This is a bad assumption for nonconvective analysis but it would seem valid for forced convection where the vaporizing propellant is continually blown away into the wake region. In addition, the empirical convection corrections were formulated for steady-state conditions which further support the argument for neglecting the transient growth of the film thickness. If the numerator and denominator on the RHS of equations

(3.48) and (3.49) are multiplied by $1/r_{amb}$ and these equations are evaluated in the limit $r_{amb} \rightarrow \infty$, the convection corrections become

$$Sh = \frac{kd_d}{\rho \mathcal{D}} = \frac{2\ln\left[1+(1+\varsigma)B\right]}{(1+\varsigma)B}\left[1+\frac{0.278Re^{\frac{1}{2}}Sc^{\frac{1}{3}}}{\left\{1+1.232/[ReSc^{\frac{4}{3}}]\right\}^{\frac{1}{2}}}\right] \tag{3.50}$$

and

$$Nu = \frac{hd_d}{\lambda} = \frac{2\ln\left[1+(1+\varsigma)B\right]^{Le^{-1}}}{\left[1+(1+\varsigma)B\right]^{Le^{-1}}-1}\left[1+\frac{0.278Re^{\frac{1}{2}}Pr^{\frac{1}{3}}}{\left\{1+1.232/[RePr^{\frac{4}{3}}]\right\}^{\frac{1}{2}}}\right] \tag{3.51}$$

The film thickness does not appear in these equations so that evaluation of r_{amb} is eliminated from the solution for k and h.

Calculation of convective effects requires a knowledge of the Reynolds number which depends upon the relative velocity of the droplet with respect to the ambient gas flow, and Lagrangian tracking of the particles requires a droplet acceleration equation. Utilizing the drag coefficient concept, droplet acceleration equations in three dimensions may be formulated. The development is described for the axial component in rectangular coordinates and the results for the transverse components are obtained in a similar manner.

Since the droplet moves with three components of relative velocity, the resultant relative velocity of the droplet is given by

$$\Delta U = \left[(U_x - U_{x_d})^2 + (U_y - U_{y_d})^2 + (U_z - U_{z_d})^2\right]^{\frac{1}{2}} \tag{3.52}$$

The resultant drag force on the drop is obtained by use of a drag coefficient which is correlated with the Reynolds number from experimental results. The resultant drag force from the three velocity components is given by

$$F_D = \rho_\infty A_{proj} C_D \frac{\Delta U^2}{2} = \frac{\pi d_d^2}{8}\rho_\infty C_D \Delta U^2 \tag{3.53}$$

The momentum equation in the axial direction may also be expressed as

$$F_{D_z} = m\frac{dU_{z_d}}{dt} = \frac{\pi}{6}d_d^3\rho_p\frac{dU_{z_d}}{dt} \tag{3.54}$$

Now, the vector relation between the resultant and axial components of force is needed. This is obtained by noting that the resultant relative velocity vector and resultant force vector have the same direction at each instant of time and that, likewise, the axial-component relative velocity and axial-component drag force have the same instantaneous direction. The desired relation is then provided from the vector geometry.

$$\frac{F_{D_z}}{F_D} = \frac{(U_z - U_{z_d})}{\Delta U} \tag{3.55}$$

Combining equation (3.53), (3.54), and (3.55) produces the axial-component of droplet acceleration.

$$\frac{dU_{z_d}}{dt} = \frac{3}{4}\frac{\rho_\infty}{\rho_p}\frac{C_D}{d_d}\Delta U(U_z - U_{z_d}) \tag{3.56}$$

The same analysis provides similar equations for the transverse components of droplet acceleration.

$$\frac{dU_{x_d}}{dt} = \frac{3}{4}\frac{\rho_\infty}{\rho_p}\frac{C_D}{d_d}\Delta U(U_x - U_{x_d}) \tag{3.57}$$

and

$$\frac{dU_{y_d}}{dt} = \frac{3}{4}\frac{\rho_\infty}{\rho_p}\frac{C_D}{d_d}\Delta U(U_y - U_{y_d}) \tag{3.58}$$

The droplet acceleration equations must be solved simultaneously with the preceedingly derived ordinary differential equations for heat and mass transport.

The drag coefficient may be determined over a broad range of Reynolds numbers by the expressions of Harrje and Reardon (1972). These relations were obtained

for the low pressure case but are extrapolated here for high-pressure environments as correlations for droplet drag in a dense gas are not available. The correlations are

$$C_D = \begin{cases} 27\,Re^{-0.84} & ;Re<80 \\ 0.271\,Re^{0.217} & ;80 \leq Re < 10^4 \\ 2 & ;10^4 \leq Re \end{cases} \tag{3.59}$$

where

$$Re = \frac{d_d \Delta U}{\nu} \tag{3.60}$$

The equations necessary for simulation of nonconvective and forced convective droplet vaporization have now been formulated. The governing system of ordinary differential equations in time are given by equations (3.36)–(3.38) with inclusion of equations (3.56)–(3.58) for the Lagrangian droplet acceleration in the convective case. A^*, B^*, and ς are defined by equations (3.32), (3.33), and (3.35), respectively. The transport parameters h, k, and r_{amb} are obtained from the simultaneous solution of the analytic equations (3.18), (3.24), and (3.46) for the nonconvective environment where the series in equation (3.46) must be truncated, and for forced convection h and k are obtained from the simultaneous solution of equations (3.48) and (3.49) where r_{amb} has been taken as infinity.

Another possible relaxation assumption is to take $\frac{d\rho_p}{dT_d} \approx 0$ which is only accurate away from critical conditions. Although the change in liquid density with respect to temperature is neglected as a derivative, the actual density change may still be accounted for in the property evaluation calculation at each time step. Great simplification occurs with this assumption and a markedly simple surface regression parameter is obtained as

$$\varsigma = -\frac{\rho_s^v}{\rho_p}(1 - y_{p_s}) = -\frac{PW_a}{\rho_p Z^v \bar{R} T_d}(1 - y_{p_s}) \tag{3.61}$$

Neglect of the bulk thermal expansion is a very strong supposition and can lead to large error approaching critical conditions where the liquid-phase density decreases to the order of the gas-phase density and during initial heat-up where bulk thermal expansion dominates over the gasification rate.

3.1.2 Mass Transfer by Aerodynamic Stripping Vaporization

The secondary atomization of droplets in the combustor was qualitatively described in Chapter 2, but inclusion of atomization in the computational physical submodel demands a quantitative description. Since the time scale for bag type fragmentation is usually longer than the residence time in a rocket chamber, only stripping mode atomization need be modeled. A heuristic expression for the stripping vaporization rate is used by Liang (1989) in the ARICC–LJ code.

$$\dot{m}_{strip} = \frac{\pi}{8} d_d^2 \Delta U \left(\rho_\infty^v \rho_p\right)^{\frac{1}{2}} \tag{3.62}$$

A more complex equation was developed by Dickerson and Coultas (1966) for the stripping vaporization rate, but it is neglected here for simplicity. The stripping mode of atomization is actuated when the Rabin number exceeds the critical value.

$$Ra > Ra_{crit} \tag{3.63}$$

Because the build up of capillary waves takes a finite amount of time, an induction period should actually be considered for the breakup process. A simple, empirically verified expression for this time period has been presented (Campbell and Chadwick, 1968). If the Rabin number criteria fails during the induction period, the capillary wave build-up process should be terminated. A new induction period would be calculated if the Rabin number criteria is exceeded again.

Modeling of stripping vaporization is especially useful for high-pressure combustors when the droplet life history is completely transient and the drop heats

to the critical state where the surface tension and heat of vaporization tend to zero. In this way, finite rate vaporization may still be considered even though the previously developed transport model predicts supercritical transition to a puff of dense gas. The reason that finite rate mass transfer is probably more realistic than flash gasification is because the drop will actually have internal temperature and concentration gradients rather than the assumed uniform profiles.

A speculative gasification process may be imagined. When the surface reaches the critical mixing temperature, somewhat lower than the pure propellant critical temperature, the less contaminated propellant in the inner region of the droplet should be slightly cooler and near to, but not at, criticality. As the surface layer is sheared away, the layer beneath rapidly heats to the critical mixture temperature and is itself sheared away, and a continuous mechanism for supercritical finite rate gasification is sustained.

According to Liang (1989), stripping vaporization is about an order of magnitude greater than transport controlled vaporization for practical applications. Using Liang's criteria for selection, the larger of the two mass transfer rates may be chosen during numerical simulation of propellant vaporization in rocket combustors

$$\dot{m} = \max\left(\dot{m}_{evap}, \dot{m}_{strip}\right) \tag{3.64}$$

3.2 FORMULATION OF THERMODYNAMIC VAPOR-LIQUID EQUILIBRIA MODELS

3.2.1 Fundamental Relations of Phase Equilibria Thermodynamics

Solution of droplet gasification transport models is inseparable from thermodynamic considerations; the vapor-liquid equilibria concentrations at the phase interface and the heat of vaporization based on real gas effects in a multi-component

system are required matching conditions for coupling the liquid-phase and gas-phase solutions. At low pressures this has traditionally been accomplished by assuming the partial pressure of the propellant vapor at the surface is identically the vapor pressure of the pure component liquid at the surface temperature, and this partial pressure is then related to the gas-phase mole fraction of the propellant at the surface. Also, the heat of vaporization is taken as the latent heat of the pure component liquid substance. These are adequate approaches for low-pressure ambiance, but they are invalid and erroneous for moderate and increasingly higher pressures. Proper evaluation demands rather rigorous formulations from multicomponent thermodynamics. Development of these formulations begins with the fundamental relations of phase equilibria thermodynamics.

From the monumental work of Josiah Willard Gibbs on classical thermodynamic equilibrium, the general results for a closed, heterogeneous system consisting of Π phases and C components or species at equilibrium with respect to the three processes of heat transfer, boundary displacement, and mass transfer are (Gibbs, 1961 re-publication)

$$T^{(1)} = T^{(2)} = \cdots = T^{(\Pi)} \tag{3.65}$$

$$P^{(1)} = P^{(2)} = \cdots = P^{(\Pi)} \tag{3.66}$$

$$\mu_i{}^{(1)} = \mu_i{}^{(2)} = \cdots = \mu_i{}^{(\Pi)} \tag{3.67}$$

where the superscript denotes the phase and the subscript denotes the component. For the case of vapor-liquid equilibria, this reduces to

$$T^v = T^l \tag{3.68}$$

$$P^v = P^l \tag{3.69}$$

$$\mu_i{}^v = \mu_i{}^l \tag{3.70}$$

The preceeding equations provide the basic criteria for vapor-liquid equilibria. That is, uniform temperature and pressure and equal chemical potentials for both phases of each component.

The chemical potential, however, is an abstract quantity with no physical representation making its use in practical application awkward. This difficulty was circumvented by G. N. Lewis who considered the chemical potential for a pure, ideal gas and then generalized this case to all systems. He first considered the thermodynamic relation

$$\left(\frac{\partial \mu_i}{\partial P}\right)_T = \overline{v}_i \tag{3.71}$$

substituted the ideal gas equation

$$\overline{v}_i = \frac{\overline{R}T}{P} \tag{3.72}$$

and integrated isothermally to obtain

$$\mu_i - \mu_i^\circ = \overline{R}T \ln \frac{P}{P^\circ} \tag{3.73}$$

For an ideal gas this equation relates the abstract quantity, chemical potential, to the physically real quantity, pressure. With a stroke of ingenuity, Lewis generalized this relation to apply to any component of any phase for any system by defining the pseudo-pressure auxiliary function f called the fugacity.

$$\mu_i - \mu_i^\circ = \overline{R}T \ln \frac{f_i}{f_i^\circ} \tag{3.74}$$

From comparison of equations (3.73) and (3.74), it is noted that for a pure, ideal gas the fugacity is identically the system pressure and for an ideal-gas mixture the fugacity of component i is identically its partial pressure $x_i{}^v P$. Hence, the

definition of fugacity is completed by observing that all systems approach ideal gas behavior at low pressures expressed mathematically by the limit

$$\lim_{P \to 0} f_i = x_i P \tag{3.75}$$

The fugacity function concept allows for the substitution of the abstract chemical potential function with a physically realistic pseudo-pressure f correcting for the non-ideal behavior of a real system. This not only furnishes a concept with tangible physical meaning but permits the transformation of the phase equilibrium relation given by equation (3.67) to an expression equating the fugacities of each phase of a given component i (Prausnitz *et al.*, 1986).

$$f_i^{(1)} = f_i^{(2)} = \cdots = f_i^{(\Pi)} \tag{3.76}$$

The governing equations for vapor-liquid equilibria therefore become

$$T^v = T^l \tag{3.77}$$

$$P^v = P^l \tag{3.78}$$

$$f_i^v = f_i^l \tag{3.79}$$

Equation (3.79) is of little more use than equation (3.70) unless the fugacity of each component can be related to the temperature, pressure, and mixture composition. This may be accomplished, though, by introducing the auxiliary function φ_i called the fugacity coefficient which is defined as

$$\varphi_i = \frac{f_i}{x_i P} \tag{3.80}$$

Assuming that the volumetric behavior of the mixture is known either from experiment or theory in the form

$$P = P(T, V, n_1, n_2, ...) \tag{3.81}$$

then the fugacity coefficient of component i may be rigorously related to the volumetric properties of a mixture through the thermodynamic relation (Prausnitz *et al.*, 1986)

$$\ln \varphi_i = \frac{1}{\overline{R}T} \int_V^\infty \left[\left(\frac{\partial P}{\partial n_i} \right)_{T,V,n_j} - \frac{\overline{R}T}{V} \right] dV - \ln Z \tag{3.82}$$

Equation (3.82) applies to all phases of component i assuming the relation of state expressed in equation (3.81) is valid for the range of densities of interest. Thus is confronted the fundamental obstacle to the practical application of phase equilibrium thermodynamics. No general, satisfactory equation of state for multicomponent mixtures exists over the density range from zero density to liquid densities (Prausnitz *et al.*, 1986). If such an analytic relationship was known explicitly in terms of pressure, its application in equation (3.82) along with the enforcement of the criteria expressed by equations (3.77) - (3.79) would solve the problem of vapor-liquid equilibria once and for all. An alternative approach developed by the engineering community is the use of a semi-empirical equation of state for determining the gas-phase fugacity from equation (3.82) and the introduction of the activity coefficient for determining the liquid phase fugacity where the activity coefficient is obtained from the Henry's constant and partial molar volume thermodynamic functions; however, experience has shown that this procedure is not generally useful for high-pressure vapor-liquid equilibria (Prausnitz *et al.*, 1986). But, in fact, a more successful course toward quantitatively useful solutions is the incorporation of an inexact yet reasonably approximate, semi-empirical equation of state, over the density range of interest, with appropriate mixing rules allowing application of the fugacity coefficient in both fluid phases. From equations (3.79) and (3.80), the criteria for equilibrium at uniform temperature and pressure becomes

$$\varphi_i{}^v x_i{}^v = \varphi_i{}^l x_i{}^l \tag{3.83}$$

where the vapor-phase and liquid-phase fugacity coefficients are obtained from an integration of the equation of state

$$\ln \varphi_i{}^v = \frac{1}{\overline{R}T} \int_{V^v}^{\infty} \left[\left(\frac{\partial P}{\partial n_i} \right)_{T,V,n_j} - \frac{\overline{R}T}{V} \right] dV - \ln Z^v \tag{3.84}$$

$$\ln \varphi_i{}^l = \frac{1}{\overline{R}T} \int_{V^l}^{\infty} \left[\left(\frac{\partial P}{\partial n_i} \right)_{T,V,n_j} - \frac{\overline{R}T}{V} \right] dV - \ln Z^l \tag{3.85}$$

Fortunately, there are reasonable, approximate equations of state and mixing rules for this purpose. An application of the Redlich-Kwong equation of state with the mixing rules of Chueh and Prausnitz (1968), known to yield good, experimentally verifiable results, is the conventional approach for droplet analyses at high pressure and is effected in this study.

In addition to the equilibrium concentrations from the phase equilibria relationships, the heat of vaporization for each component is required as a matching condition at the phase boundary for the energy transport equations. The component heat of vaporization is defined as the difference between the partial molar enthalpy of the vapor and liquid phases

$$\overline{h}_{vap,i} = \tilde{h}_i^{\,v} - \tilde{h}_i^{\,l} \tag{3.86}$$

where the partial molar enthalpy for a component in a mixture can be determined from the rigorous thermodynamic relation (Prausnitz *et al.*, 1986)

$$\frac{\overline{h}_i^{\circ} - \tilde{h}_i}{\overline{R}T^2} = \frac{\partial(\ln \varphi_i)}{\partial T} \tag{3.87}$$

where

$$\overline{h}_i^{\circ}(T) = \overline{h}_i^{\circ}(T_{ref}) + \int_{T_{ref}}^{T} \overline{C}_{p_i}^{\circ} dT \tag{3.88}$$

Before examining the development of a practical multicomponent vapor-liquid equilibria model, some consequential implications for the overall droplet vaporization model are obtained from the Gibbs phase rule. For a system that does not involve chemical reaction, the Gibbs phase rule states that the degrees of freedom F, which is the number of intensive thermodynamic properties required to fix the state of the system, is equal to the difference between the number of components C and number of phases Π present in the system plus two

$$F = C - \Pi + 2 \tag{3.89}$$

The immediate inference is that for a two phase vapor-liquid system the number of intensive properties that must be specified is identically the number of components present in the system. Thus, for a two-component vapor-liquid system, only two intensive properties of the system need be specified which, for a droplet vaporization model, would be the temperature and pressure at the phase interface. For a system with three or more components, however, $C-2$ vapor-phase or liquid-phase mole fractions must be specified in addition to the temperature and pressure at the drop surface to satisfy the Gibbs phase rule. This poses a critical but avoidable impediment to a phase equilibrium solution since the mole fractions are not known a priori in a droplet gasification model.

Careful consideration reveals that the problem is surmountable by making a first order approximation in time for the liquid-phase species conservation equations and iterating to convergence for each time step in the overall numerical solution procedure (Shuen, 1988). At time zero the initial concentrations are given, and liquid-phase mole fractions for the ensuing time step are guessed to meet the required number of specified intensive variables from the Gibbs phase rule. The phase equilibrium relationships are then solved providing the unknown vapor-phase and

liquid-phase mole fractions. At this point, the predicted liquid-phase mole fractions are checked against the overall conservation of species in the liquid using the first order approximation

$$n_{i_l}(t+\Delta t) \approx n_{i_l}(t) - \left[\left.\frac{dn_i''}{dt}\right|_s \Delta t\right]\pi d_d^2 \tag{3.90}$$

from which the previously guessed liquid-phase mole fractions are adjusted. The whole process is then repeated to convergence. This method provides the liquid-phase composition as a function of time.

3.2.2 A General High-Pressure Vapor-Liquid Equilibria Model with the Redlich-Kwong Equation of State

The generalized results presented in the preceeding section provides the basis for high-pressure vapor-liquid equilibria so long as a suitable equation of state is available. As noted previously, the state relation conventionally used is the Redlich-Kwong equation of state with the mixing rules of Chueh and Prausnitz (1968) for nonpolar and weakly polar molecules in fluid mixtures. Because their method yields reasonably accurate equilibria predictions, it will be incorporated in this study.

Development begins with the Redlich-Kwong equation of state in the functional form of equation (3.81). For a single component system the state relation is

$$P = \frac{\overline{R}T}{\overline{v}-b} - \frac{a}{\overline{v}(\overline{v}+b)T^{\frac{1}{2}}} \tag{3.91}$$

If the compressibility factor Z is introduced, equation (3.91) may be reformulated to give

$$Z^3 - Z^2 + (A - B - B^2)Z - AB = 0 \tag{3.92}$$

where

$$A = \frac{aP}{\overline{R}^2 T^{\frac{5}{2}}} \tag{3.93}$$

and

$$B = \frac{bP}{\overline{R}T} \tag{3.94}$$

The constants a and b in the Redlich-Kwong equation are, for a pure component,

$$a = \Omega_a \frac{\overline{R}^2 T_c^{\frac{5}{2}}}{P_c} \tag{3.95}$$

$$b = \Omega_b \frac{\overline{R}T_c}{P_c} \tag{3.96}$$

where Ω_a and Ω_b are dimensionless constants with the values of 0.4278 and 0.0867 respectively near the critical point. For a mixture, however, Chueh and Prausnitz (1968) have suggested mixing rules which apply over a relatively wide range of temperature, rather than in the critical region only. The rules are

$$b = \sum_{i=1}^{N} x_i b_i \tag{3.97}$$

where

$$b_i = \Omega_{b_i} \frac{\overline{R}T_{c_i}}{P_{c_i}} \tag{3.98}$$

and

$$a = \sum_{i=1}^{N} \sum_{j=1}^{N} x_i x_j a_{ij} \qquad (a_{ij} \neq \sqrt{a_{ii} a_{jj}}) \tag{3.99}$$

where

$$a_{ii} = \Omega_{a_i} \frac{\overline{R}^2 T_{c_i}^{\frac{5}{2}}}{P_{c_i}} \tag{3.100}$$

$$a_{ij} = \left(\frac{\Omega_{a_i} + \Omega_{a_j}}{2}\right)\frac{\overline{R}^2 T_{c_{ij}}^{\frac{5}{2}}}{P_{c_{ij}}} \tag{3.101}$$

$$P_{c_{ij}} = \frac{Z_{c_{ij}}\overline{R}T_{c_{ij}}}{\overline{v}_{c_{ij}}} \tag{3.102}$$

$$\overline{v}_{c_{ij}}^{\frac{1}{3}} = \frac{\overline{v}_{c_i}^{\frac{1}{3}} + \overline{v}_{c_j}^{\frac{1}{3}}}{2} \tag{3.103}$$

$$Z_{c_{ij}} = 0.291 - 0.08\left(\frac{\omega_i + \omega_j}{2}\right) \tag{3.104}$$

$$T_{c_{ij}} = \sqrt{T_{c_i} T_{c_j}}(1 - k_{ij}) \tag{3.105}$$

In the above equations, Ω_{a_i} and Ω_{b_i} are evaluated for each pure component by fitting the Redlich-Kwong state relation to the volumetric data of the saturated vapor. The temperature range generally used is from the normal boiling point to the critical point. The results seem to indicate a correlation with the acentric factor ω. Prausnitz and Chueh (1968) present values of Ω_{a_i} and Ω_{b_i} for some of the most commonly encountered substances and binary systems. The binary interaction constant k_{ij} represents the deviation from the geometric mean for $T_{c_{ij}}$ and must, in general, be determined from experimental information. The most frequently used approach is to fit the interaction constant for second virial cross coefficients. Prausnitz and Chueh (1968) present estimates for the interaction constant for 125 binary systems, and additional values for k_{ij} have been determined by Lazar and Faeth (1971). Some of the more useful values of the required empirical constants are given in Tables 1 and 2.

Note that the polar H_2O molecule has been included despite its relatively significant dipole moment (1.8 *debye*). Such broadening in theory should be considered

Table 1

Acentric Factors and Dimensionless Constants in the

Redlich-Kwong Equation of State for Saturated Vapors*

Substance	ω	Ω_a	Ω_b
methane	0.013	0.4278	0.0867
oxygen†	0.025	0.4280	0.0870
nitrogen	0.040	0.4290	0.0870
ethylene	0.085	0.4323	0.0876
hydrogen sulfide	0.100	0.4340	0.0882
ethane	0.105	0.4340	0.0880
propylene	0.139	0.4370	0.0889
propane	0.152	0.4380	0.0889
iso-butane	0.187	0.4420	0.0898
acetylene	0.190	0.4420	0.0902
1-butene	0.190	0.4420	0.0902
n-butane	0.200	0.4450	0.0906
cyclohexane	0.209	0.4440	0.0903
benzene	0.211	0.4450	0.0904
iso-pentane	0.215	0.4450	0.0906
carbon dioxide	0.225	0.4470	0.0911
n-pentane	0.252	0.4510	0.0919
n-hexane	0.299	0.4590	0.0935
water†	0.344	0.4671	0.0950
n-heptane	0.349	0.4680	0.0952
n-octane	0.398	0.4760	0.0968

* Adapted from Prausnitz and Chueh (1968)

† Author's estimated fit to volumetric data

Table 2

Binary Interaction Parameters, k_{ij}*

$(k_{ij} = k_{ji},\ k_{ii} = 0)$

Substance	N_2	O_2	CO_2	H_2O
methanol	0.10	—	0.08	0.15
ethanol	0.15	—	0.11	0.20
n-decane	0.50	—	0.43	0.55
n-octane	0.40	—	0.34	0.45
n-heptane	0.35	—	0.29	0.40
n-hexane	0.30	—	0.25	0.35
n-pentane	0.25	—	0.20	0.30
hydrogen	0.00	0.00†	—	—

* Adapted from Lazar and Faeth (1971), Chueh and Prausnitz (1967), and Shuen (1988)

† Author's estimate

Note: The conventional method for obtaining values for the binary interaction constant is from data on second virial cross coefficients. If the Redlich-Kwong equation is expanded in a power series in reciprocal volume, and using the fact that the second cross virial coefficient is a quadratic function of mole fraction, the following relation may be obtained (Prausnitz, 1969)

$$B_{ij} = \frac{1}{2}(b_i + b_j) - \frac{a_{ij}}{RT^{\frac{5}{2}}}$$

The binary interaction constants may then be determined by fitting available experimental results.

only tentative until techniques for including polar compounds are developed. There is some justification for the current approach, however. Since the polar (electrostatic) effect results in a tendency to align the molecules and the thermal (kinetic energy) effect tends to randomly orient the molecules, the polar contribution may be expected to become small at higher temperatures (Prausnitz *et al.*, 1986). The ability to approximate the behavior of aqueous gas mixtures at advanced pressures with the Redlich-Kwong equation has been demonstrated (de Santis *et al.*, 1974). Inclusion of the quadrupole CO_2 molecule may also be justified by noting that quadrupole moments have a much reduced effect on thermodynamic properties than that of dipole moments (Parsonage and Scott, 1962).

With the Redlich-Kwong equation of state and the proposed mixing rules, equations (3.84) and (3.85) may be integrated. The results are (Prausnitz *et al.*, 1986)

$$\ln \varphi_i^v = \ln \frac{\overline{v}^v}{\overline{v}^v - b^v} + \frac{b_i}{\overline{v}^v - b^v} - \frac{2\sum_{j=1}^N x_j^v a_{ji}}{\overline{R}T^{\frac{3}{2}} b^v} \ln \frac{\overline{v}^v + b^v}{\overline{v}^v} + \frac{a^v b_i}{\overline{R}T^{\frac{3}{2}}(b^v)^2}\left[\ln \frac{\overline{v}^v + b^v}{\overline{v}^v} - \frac{b^v}{\overline{v}^v + b^v}\right] - \ln Z^v \tag{3.106}$$

and

$$\ln \varphi_i^l = \ln \frac{\overline{v}^l}{\overline{v}^l - b^l} + \frac{b_i}{\overline{v}^l - b^l} - \frac{2\sum_{j=1}^N x_j^l a_{ji}}{\overline{R}T^{\frac{3}{2}} b^l} \ln \frac{\overline{v}^l + b^l}{\overline{v}^l} + \frac{a^l b_i}{\overline{R}T^{\frac{3}{2}}(b^l)^2}\left[\ln \frac{\overline{v}^l + b^l}{\overline{v}^l} - \frac{b^l}{\overline{v}^l + b^l}\right] - \ln Z^l \tag{3.107}$$

where Z^v and Z^l are given by the largest and smallest real roots of equation (3.92), respectively. Upon further algebraic manipulation and introduction of the equation of state as expressed in equation (3.92), the fugacity coefficient relationships become

$$\ln \varphi_i^v = \frac{b_i}{b^v}(Z^v - 1) - \ln(Z^v - B^v) - \frac{A^v}{B^v}\left[\frac{2\sum_{j=1}^N x_j^v a_{ji}}{a^v} - \frac{b_i}{b^v}\right] \ln\left(1 + \frac{B^v}{Z^v}\right) \tag{3.108}$$

and

$$\ln \varphi_i^l = \frac{b_i}{b^l}(Z^l - 1) - \ln(Z^l - B^l) - \frac{A^l}{B^l}\left[\frac{2\sum_{j=1}^{N} x_j^l a_{ji}}{a^l} - \frac{b_i}{b^l}\right] \ln\left(1 + \frac{B^l}{Z^l}\right) \quad (3.109)$$

Substitution of these results into the vapor-liquid equilibria criteria given by equation (3.83) produces an expression in terms of the mole fractions in both phases

$$\frac{x_i^v}{x_i^l} = \frac{\exp\left\{\frac{b_i}{b^l}(Z^l - 1) - \ln(Z^l - B^l) - \frac{A^l}{B^l}\left[\frac{2\sum_{j=1}^{N} x_j^l a_{ji}}{a^l} - \frac{b_i}{b^l}\right] \ln\left(1 + \frac{B^l}{Z^l}\right)\right\}}{\exp\left\{\frac{b_i}{b^v}(Z^v - 1) - \ln(Z^v - B^v) - \frac{A^v}{B^v}\left[\frac{2\sum_{j=1}^{N} x_j^v a_{ji}}{a^v} - \frac{b_i}{b^v}\right] \ln\left(1 + \frac{B^v}{Z^v}\right)\right\}} \quad (3.110)$$

Equation (3.101) applies to each component of the system under consideration. In addition, two more equations may be obtained by noting that the sum of the mole fractions in each phase is unity.

$$\sum_{i=1}^{N}(x_i^v \text{ or } x_i^l) = 1 \quad (3.111)$$

The equations necessary for evaluation of vapor-liquid equilibria have now been presented. With the temperature, pressure, and $C - 2$ vapor-phase or liquid-phase mole fractions specified, expressions (3.92) with its mixing rules, (3.110), and (3.111) produce a system of very nonlinear, coupled algebraic equations for the unknown mole fractions in both phases.

The generalized result for $\ln \varphi_i$, as expressed for the vapor-phase in equation (3.106) and for the liquid-phase in equation (3.107), may be differentiated with respect to temperature for application in equation (3.87). This gives an expression for obtaining the partial molar enthalpy of a component in a designated phase. Applying the rules of multivariable calculus and carrying through with the differentiation yields (Shuen, 1988)

$$\frac{\overline{h}_i^\circ - \tilde{h}_i}{\overline{R}T^2} = \frac{\partial(\ln \varphi_i)}{\partial T} = (\overline{A} - 1)\frac{\overline{C}}{Z} + \frac{\overline{A}}{T} + \overline{B} \quad (3.112)$$

where

$$\overline{A} = \frac{-b}{\overline{v}-b} - \frac{b_i\overline{v}}{(\overline{v}-b)^2} + \frac{2\sum_{j=1}^{N} x_j a_{ji}}{\overline{R}T^{\frac{3}{2}}(\overline{v}+b)} - \frac{ab_i}{\overline{R}T^{\frac{3}{2}}(\overline{v}+b)^2} \tag{3.113}$$

$$\overline{B} = \frac{3}{2\overline{R}T^{\frac{5}{2}}b}\left[2\left(\sum_{j=1}^{N} x_j a_{ji}\right)\ln\left(\frac{\overline{v}+b}{\overline{v}}\right)\frac{ab_i}{b}\ln\left(\frac{\overline{v}+b}{\overline{v}}\right) + \frac{ab_i}{\overline{v}+b}\right] \tag{3.114}$$

$$\overline{C} = \frac{\frac{2\overline{D}Z}{T} + \frac{PZ}{(\overline{R}T)^2}\left[\frac{a}{2T^{\frac{3}{2}}} + b\overline{R}\right] - \frac{3.5abP^2}{\overline{R}^3T^{\frac{9}{2}}}}{3Z^2 - 2Z + \overline{D}} \tag{3.115}$$

$$\overline{D} = \left[\frac{a}{T^{\frac{1}{2}}} - b\overline{R}T - b^2P\right]\frac{P}{(\overline{R}T)^2} \tag{3.116}$$

If equation (3.112) is solved for each phase, and the results substituted into equation (3.86), the heat of vaporization of the specified component is determined.

3.2.3 Modification of General High-Pressure Vapor-Liquid Equilibria Model for Inclusion of Quantum Gases

The general equilibria model described in section 3.2.2 is only applicable for nonpolar or weakly polar molecules and nonquantum gases, whereas the inclusion of quantum gases (eg. hydrogen) into the theory is highly desirable for application to modern propulsion systems. Modern liquid fueled rockets, for example, burn liquid hydrogen with LOX for maximum engine performance. Because hydrogen is extremely volatile, it can generally be assumed to flash vaporize at the injector face (Harrje and Reardon, 1972) such that LOX droplets consequently undergo vaporization in a hydrogen rich gas. This assumption is particularly appropriate for the SSME where, for example, all of the hydrogen fuel and only a small quantity of LOX are coaxially injected into the preburners which operate at around 5000 psia

and 800–900 K to drive the high-pressure turbines. Furthermore, additional LOX and the moderately hot, hydrogen rich gaseous mixture from the preburners are injected coaxially into the high-pressure main combustion chamber operating at about 3000 psia. From this standpoint, theoretical prediction for high-pressure LOX-H_2 vapor-liquid equilibria is of importance to the modeling of LOX droplet vaporization in the hydrogen rich region of high-pressure liquid rocket combustion chambers.

One may immediately ask whether H_2O should also be considered in the analysis. Certainly water vapor is present in the combustor as the major combustion product, but for the fuel/oxidant ratio of the SSME preburners, the water concentration will be small. In addition, unreacted propellant vapors should be dominant in the vaporization region. While H_2O could theoretically be considered, the extrapolation of current theory down to cryogenic temperatures for such a polar molecule would be unfounded. Of course, liquifaction or solidification of H_2O at the cold LOX droplet surface is another consideration.

The distinguishing feature of quantum gases is their low molecular weight which requires that their configurational properties be described by quantum mechanics instead of classical statistical mechanics. In addition, the effective critical properties of quantum gases depend upon molecular weight and temperature. The corresponding-states treatment utilized in the classical equilibria theory of the preceding section is thus invalidated for quantum gases in its present form. Chueh and Prausnitz (1967) have, however, modified their classical theory to encompass quantum gases by defining effective temperature dependent critical properties such that the quantum-gas properties coincide with classical gas properties. By fitting the Redlich-Kwong equation to experimental data with the critical point values $\Omega_a = 0.42478$ and $\Omega_b = 0.08664$, they determined the effective critical constants for

quantum gases as a function of molecular weight and temperature.

$$T_c = \frac{T_c^\circ}{1 + \frac{c_1}{WT}} \tag{3.117}$$

$$P_c = \frac{P_c^\circ}{1 + \frac{c_2}{WT}} \tag{3.118}$$

And, from comparison of experimental data with correlations for second and third virial coefficients, they deduced

$$\overline{v}_c = \frac{\overline{v}_c^\circ}{1 + \frac{c_3}{WT}} \tag{3.119}$$

The constants c_1, c_2, and c_3 as determined by Chueh and Prausnitz are $c_1 = 21.8, c_2 = 44.2$, and $c_3 = -9.91$, and the circle superscript denotes the classical value. Note that the critical constants approach the classical value when the product WT becomes large.

The general vapor-liquid equilibria theory can now be applied to mixtures containing one or more quantum gases by using the mixing rules given by equations (3.97) through (3.101); however, the binary interaction constants must be evaluated using the effective critical constants. In this instance, $T_{c_{ij}}$ and $P_{c_{ij}}$ are given by

$$T_{c_{ij}} = \frac{\sqrt{T_{c_{ii}}^\circ T_{c_{jj}}^\circ}(1 - k_{ij})}{1 + \frac{c_1}{W_{ij}T}} \tag{3.120}$$

$$P_{c_{ij}} = \frac{P_{c_{ij}}^\circ}{1 + \frac{c_2}{W_{ij}T}} \tag{3.121}$$

where

$$P_{c_{ij}}^\circ = \frac{Z_{c_{ij}}^\circ \overline{R}\sqrt{T_{c_{ii}}^\circ T_{c_{jj}}^\circ}(1 - k_{ij})}{\overline{v}_{c_{ij}}^\circ} \tag{3.122}$$

$$\overline{v}^{\circ\,\frac{1}{3}}_{c_{ij}} = \frac{\overline{v}^{\circ\,\frac{1}{3}}_{c_i} + \overline{v}^{\circ\,\frac{1}{3}}_{c_j}}{2} \tag{3.123}$$

$$Z^{\circ}_{c_{ij}} = 0.291 - 0.08\left(\frac{\omega_i + \omega_j}{2}\right) \tag{3.124}$$

$$\frac{1}{W_{ij}} = \frac{1}{2}\left(\frac{1}{W_i} + \frac{1}{W_j}\right) \tag{3.125}$$

For all quantum gases, $\Omega_a = 0.42478$ and $\Omega_b = 0.08664$, and the effective acentric factor is taken as zero. This implies that the classical critical molar specific volume is defined by

$$\overline{v}^{\circ}_c = 0.291\frac{\overline{R}T^{\circ}_c}{P^{\circ}_c} \tag{3.126}$$

The classical critical constants for hydrogen which are used in this study are $T^{\circ}_c = 43.6\ K$ and $P^{\circ}_c = 20.5\ bar$.

3.2.4 A Simplified Vapor-Liquid Equilibria Model with the Redlich-Kwong Equation of State: No Ambient Gas Absorption

The vapor-liquid equilibria model, with appropriate mixing rules as presented in the preceeding sections, is a general formulation that includes ambient gas absorption into the liquid phase. Away from the critical mixing state, however, it seems reasonable to assume ambient gas solubility is negligible implying that the droplet remains a pure component liquid. This introduces much simplification in the phase equilibrium model while retaining the multi-component real gas effects in the gas phase. As long as an awareness for the range of applicability is maintained, the pure liquid component formulation yields good results.

Development in this case follows the introduction of the Redlich-Kwong state relation and mixing rules as previously described for nonpolar substances or polar

gases. In addition, equation (3.108) is retained for the gas-phase fugacity coefficients. Simplification then occurs in evaluation of the liquid-phase fugacity for the assumption of no ambient gas absorption. It can be shown (Prausnitz *et al.*,1986) that the pure component liquid-phase fugacity is given by

$$f_i^l = \varphi_i^s P_{v_i} \exp\left\{ \int_{P_{v_i}}^{P} \frac{\overline{v}_i^l}{\overline{R}T} dP \right\} \tag{3.127}$$

where φ_i^s is the pure component fugacity coefficient at saturation defined by

$$\varphi_i^s = \frac{f_i^s}{P_{v_i}} \tag{3.128}$$

In addition, if the liquid component is considered incompressible, which is a reasonable assumption away from the critical point, the integral in equation (3.127) is directly evaluated such that the pure component fugacity may be approximated as

$$f_i^l \approx \varphi_i^s P_{v_i} \exp\left[\frac{\overline{v}_i^l (P - P_{v_i})}{\overline{R}T} \right] \tag{3.129}$$

Note that equation (3.129) indicates the fugacity is equal to the saturation pressure to a first approximation but is multiplicatively corrected by φ_i^s for deviations of the saturated vapor from ideal gas behavior and by an exponential correction designated as the Poynting factor for pressure effects.

The saturation fugacity coefficient can be evaluated from saturation fugacity and vapor pressure data, or it may be estimated from generalized results from the law of corresponding states. For instance, the saturation fugacity may be estimated from the saturation line on the generalized fugacity chart of Sonntag and Van Wylen (1982) which was obtained through an integration of the generalized compressibility chart. A rough curve fit approximation to the saturation line is given by

$$\varphi_i^s \approx \begin{cases} 1.0 & ;0 \leq T_r < 0.5 \\ 0.77 + 0.77T_r - 0.37T_r^2 - 0.51T_r^3 & ;0.5 \leq T_r \leq 1.0 \end{cases} \tag{3.130}$$

Applying the phase equilibrium criteria and the fugacity definition to equation (3.129) gives an expression for the gas-phase fugacity coefficient

$$\varphi_i^v = \frac{\varphi_i^s P_{v_i}}{x_i^v P} \exp\left[\frac{\overline{v}_i^l (P - P_{v_i})}{\overline{R}T}\right] \tag{3.131}$$

Now, since there is no absorption of ambient gas, the liquid-phase mole fraction remains unity, and the only unknown is the gas-phase mole fraction of the propellant. Applying equation (3.108) and (3.131) for the propellant and combining gives a transcendental expression for the propellant surface gas-phase mole fraction.

$$x_p^v = \frac{\frac{\varphi_p^s P_{v_p}}{P} \exp\left[\frac{\overline{v}_p^l (P - P_{v_p})}{\overline{R}T}\right]}{\exp\left\{\frac{b_p}{b^v}(Z^v - 1) - \ln(Z^v - B^v) - \frac{A^v}{B^v}\left[\frac{2\sum_{j=1}^{N} x_j^v a_{jp}}{a^v} - \frac{b_p}{b^v}\right] \ln\left(1 + \frac{B^v}{Z^v}\right)\right\}} \tag{3.132}$$

Equation (3.132) is also valid for quantum-gas mixtures if the mixing rules from section 3.2.3 are utilized.

Given the concentration of ambient gases, droplet surface temperature, and ambient pressure, equation (3.132) can be solved independently in an iterative fashion for the unknown gas-phase propellant concentration. Because the above analysis neglects dissolution of ambient gas into the propellant droplet, the model is invalid and fails at very high pressures. For these cases, the general model considering ambient gas absorption should be used.

The assumption of a pure component liquid-phase also simplifys the evaluation of the propellant heat of vaporization. This occurs because the partial molar enthalpy of a pure component is identically the molar enthalpy of that component. Thus, equation (3.86) may be written as

$$\overline{h}_{vap,i} = \tilde{h}_i^{\,v} - \overline{h}_i^{\,l} \tag{3.133}$$

Substituting for $\tilde{h}_i^v$ from equation (3.87) and designating the propellant component yields

$$\overline{h}_{vap,p} = (\overline{h}_p^v - \overline{h}_p^l) - \overline{R}T^2 \frac{\partial(\ln \varphi_p^v)}{\partial T} \tag{3.134}$$

or

$$\overline{h}_{vap,p} = \overline{L}_p - \overline{R}T^2 \frac{\partial(\ln \varphi_p^v)}{\partial T} \tag{3.135}$$

In equation (3.135), $\overline{L}_p$ represents the molar latent heat of vaporization for the propellant substance, and the negative term represents the deviation due to real gas effects where the partial derivative is evaluated from equation (3.112) for the vapor phase.

CHAPTER 4

NUMERICAL SIMULATION, MODEL VALIDATION, AND PARAMETRIC BEHAVIOR

4.1 NUMERICAL SIMULATION CODES AND MODEL VALIDATION

4.1.1 Evaluation of Vapor-Liquid Equilibria Models

A general vapor-liquid equilibria model with ambient gas absorption and a simplified vapor-liquid equilibria model without ambient gas absorption were described in Chapter 3 for nonpolar (and weakly polar) or quantum-gas mixtures, and solution methodologies and computational results will now be presented. Analysis of the equilibria models is first undertaken independent from the transport model for validation and illustrative purposes. Equilibria computation is later included as a submodel in the transport simulation code for droplet gasification.

Analysis of the general model entails the simultaneous solution of the nonlinear, algebraic system produced from an application of equation (3.110) for each component and of equation (3.111) for each phase in the system. Furthermore, analysis of the simplified model for a pure liquid component requires solution of the transcendental equation (3.132). In both cases, extraction of a direct, one-step computation for equilibria concentration is not possible and iterative solution procedures for the equilibria concentrations must be employed. Once the equilibria concentrations have been calculated, however, the enthalpy of vaporization is a direct, single calculation for both models.

Solution of the simplified, no absorption model is straight forward and follows the methodology presented by Matlosz *et al.* (1972). The iterative procedure is as follows:

(1) Estimate x_p^v from equation (3.131) with $\varphi_p^v = 1$.

(2) Solve Redlich-Kwong state relation with estimated x_p^v.

(3) Solve for new x_p^v from equation (3.132) by iteration.

(4) If the difference between x_p^v from step 3 and x_p^v from step 1 is not less than some specified small tolerance value, repeat steps 2–4 using latest x_p^v to convergence.

Equation (3.135) is then solved for the enthalpy of vaporization. A FORTRAN computer code was developed using the above computational algorithm and was run on a MASSCOMP 5600 computer. A tolerance value of 0.0001 for the propellant mole fraction was typically specified, and run times were only a few seconds when varying the pressure or temperature over a wide range of values.

Calculations for the n-hexane gas phase mole fraction in a n-hexane–nitrogen binary system with the no ambient gas absorption model are shown by the solid lines of Figures 7 and 8. The experimental data of Poston and McKetta (1966) are also plotted illustrating an excellent comparison with theory. Furthermore, predictions from the low-pressure, pure liquid vapor pressure ideal-gas equilibria assumption are given by the long dashed lines, and they show a substantial underprediction of experiment with increasing pressure. At low pressures the ideal-gas model is an accurate and viable approach for vapor-liquid equilibria, but its use is obviously inappropriate for ambient pressures much greater than 1 atm. Since the difference between the gas-phase surface concentration and ambient concentration represents the driving potential for mass transfer, it is essential to obtain accurate values for equilibria concentration at the phase interface, and the model appropriate to the environmental conditions should be utilized.

The calculated enthalpy of vaporization for the no absorption model is shown by

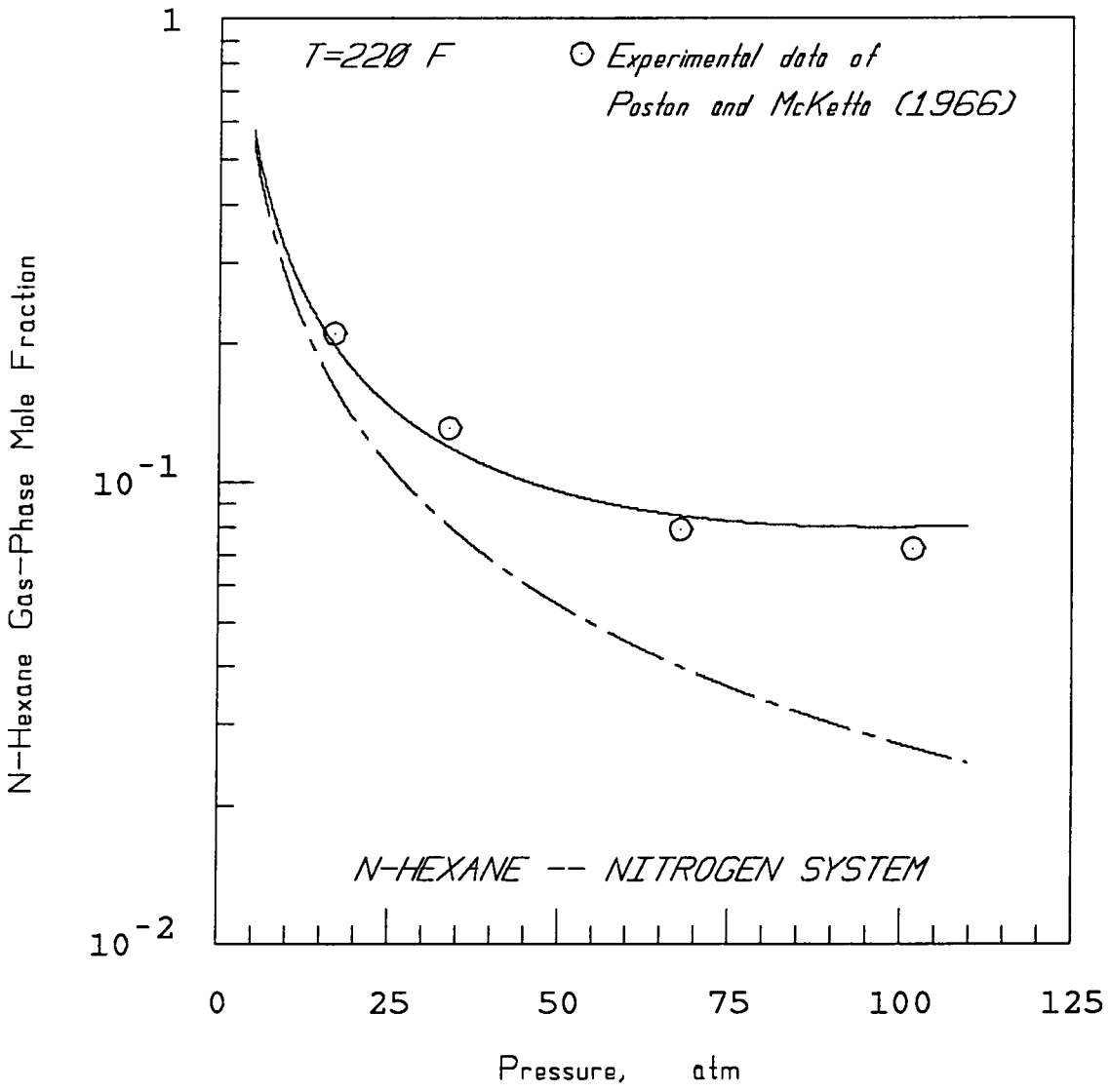

Figure 7. Comparison of theoretical equilibria from no-absorption model and ideal-gas model (dashed line) with experimental data for the n-hexane—nitrogen binary system at $T_\infty = 220\ F$.

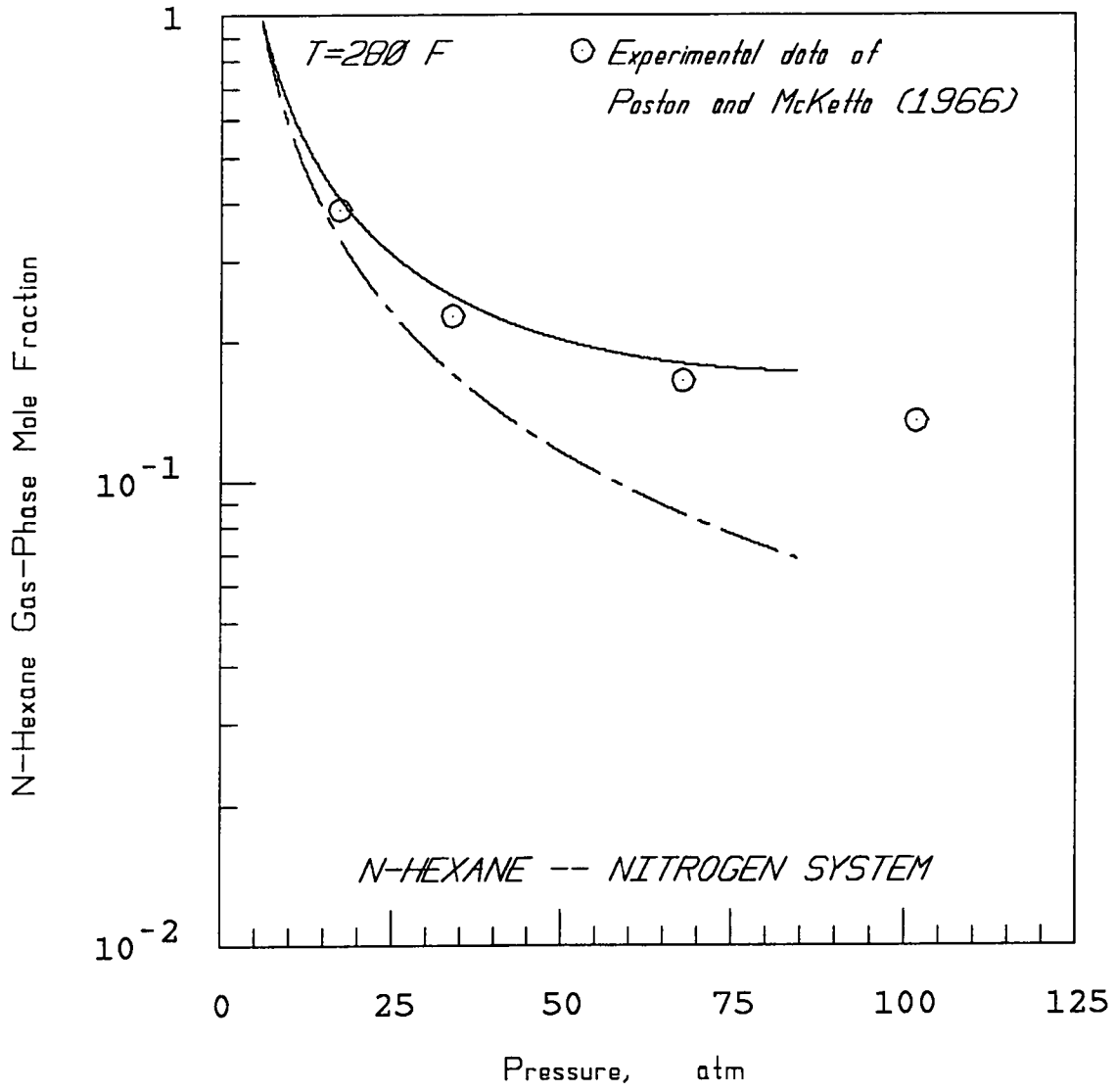

Figure 8. Comparison of theoretical equilibria from no-absorption model and ideal-gas model (dashed line) with experimental data for the n-hexane—nitrogen binary system at $T_\infty = 280\ F$.

the dashed lines in Figure 9 for different ambient pressures, and the pure component latent heat of vaporization is also shown by the solid curve for comparative purposes. A significant deviation between high-pressure theory and low-pressure theory again exists. From the figure one sees that the actual enthalpy of vaporization decreases with increasing pressure and that the latent heat becomes a poorer approximation. At temperatures approaching the critical mixing state, theory is unable to predict an equilibria condition because of the no absorption restriction; therefore, this model is only applicable away from critical conditions. Experimental data on partial molar enthalpies are virtually nil, and validation of the model for prediction of enthalpy of vaporization was not possible.

The numerical effort required for solution of the general vapor-liquid equilibria model which considers ambient gas absorption is much more intensive than the no absorption model as now a system of strongly nonlinear, algebraic equations must be solved rather than a single equation for a single variable. Initially, various simple iterative schemes were devised and coded by the author with diverse degrees of success. Some methods diverged completely while others converged within a range of system temperatures and pressures. None of the schemes provided a comprehensive, reliable technique over a wide range of conditions, and all failed in the near critical region. To circumvent this difficulty, a more sophisticated algorithm was required.

The hybrid algorithm adopted is a variation of Newton's method with finite difference approximations to the Jacobian as coded in the ZSPOW subroutine for roots of a nonlinear system of equations in the IMSL© Software Library (1985). Special steps are also taken in the subroutine to avoid large step sizes or increasing residuals. A FORTRAN code was developed to call the ZSPOW subroutine in the IMSL© Software Library for selected temperatures and pressures with the solution returned to the main program. This code was run on the MASSCOMP 5600

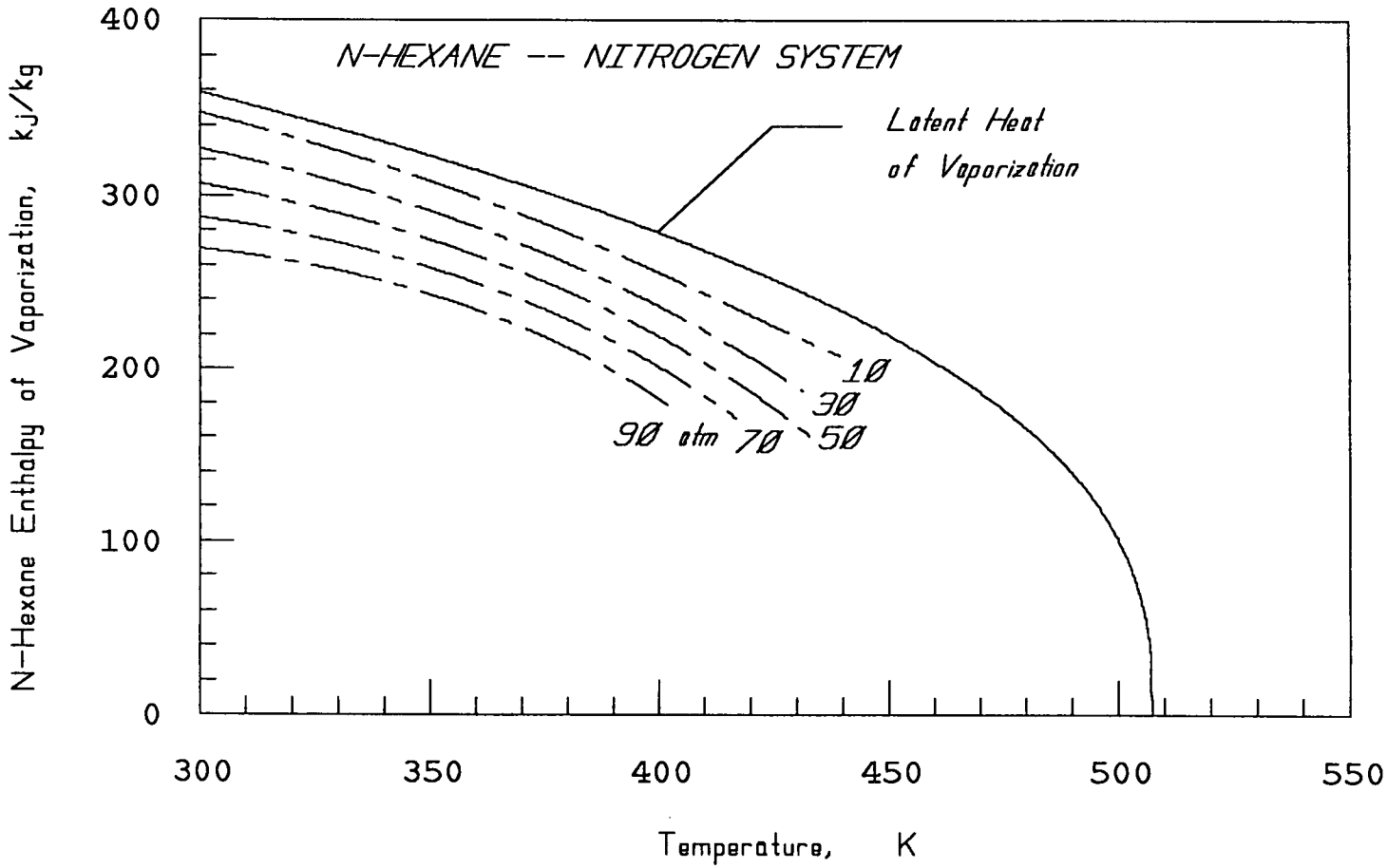

Figure 9. Comparison of theoretical enthalpy of vaporization, based upon a no-absorption model, to the latent heat of vaporization for the n-hexane—nitrogen binary system.

computer with the algorithm obtaining converged solutions for all conditions except for the near-critical region with reduced pressures less than unity. It is believed the inability to converge under these conditions occurred because ambient specie molar concentrations tend to zero in this regime and the subroutine could not meet the tolerance requirements. This problem might be correctable by reformulating the problem with different limiting conditions. The results obtained in the above manner were sufficient for the present study, however.

Validation calculations were performed with the general equilibria model for the n-pentane – carbon dioxide binary system at a pressure of 600 psia ($P_r \approx 1.23$) as shown by the solid curves in Figure 10. The top curve represents vapor-phase equilibria concentrations while the bottom curve represents liquid-phase equilibria concentrations. The experimental data of Poettmann and Katz (1945) are shown for comparison. The theory shows relatively good agreement for the vapor-phase although the error tends to increase with increasing temperature with the greatest deviation occurring at the critical state. Prediction of liquid-phase equilibria concentration is rather bad, especially at lower temperatures, but this should not be surprising as extension of the Redlich-Kwong equation into the liquid-phase region is a rough approximation at best. Since the theoretical model underpredicts the critical mixing temperature in this case by only 10 K, and there is reasonable agreement for the vapor-phase, the theory seems sufficiently accurate for use as a submodel in the high-pressure droplet gasification model.

Results from the code for the general model are also shown in Figures 11 and 12 for the n-pentane – nitrogen binary system over a wider range of conditions. Figure 11 depicts the liquid-phase and vapor-phase equilibria mole fractions of n-pentane from 300 K to the critical state for reduced pressures of $P_r = 1$, $P_r = 2$, $P_r = 3$. With increasing pressure one sees that the critical mixing temperature decreases

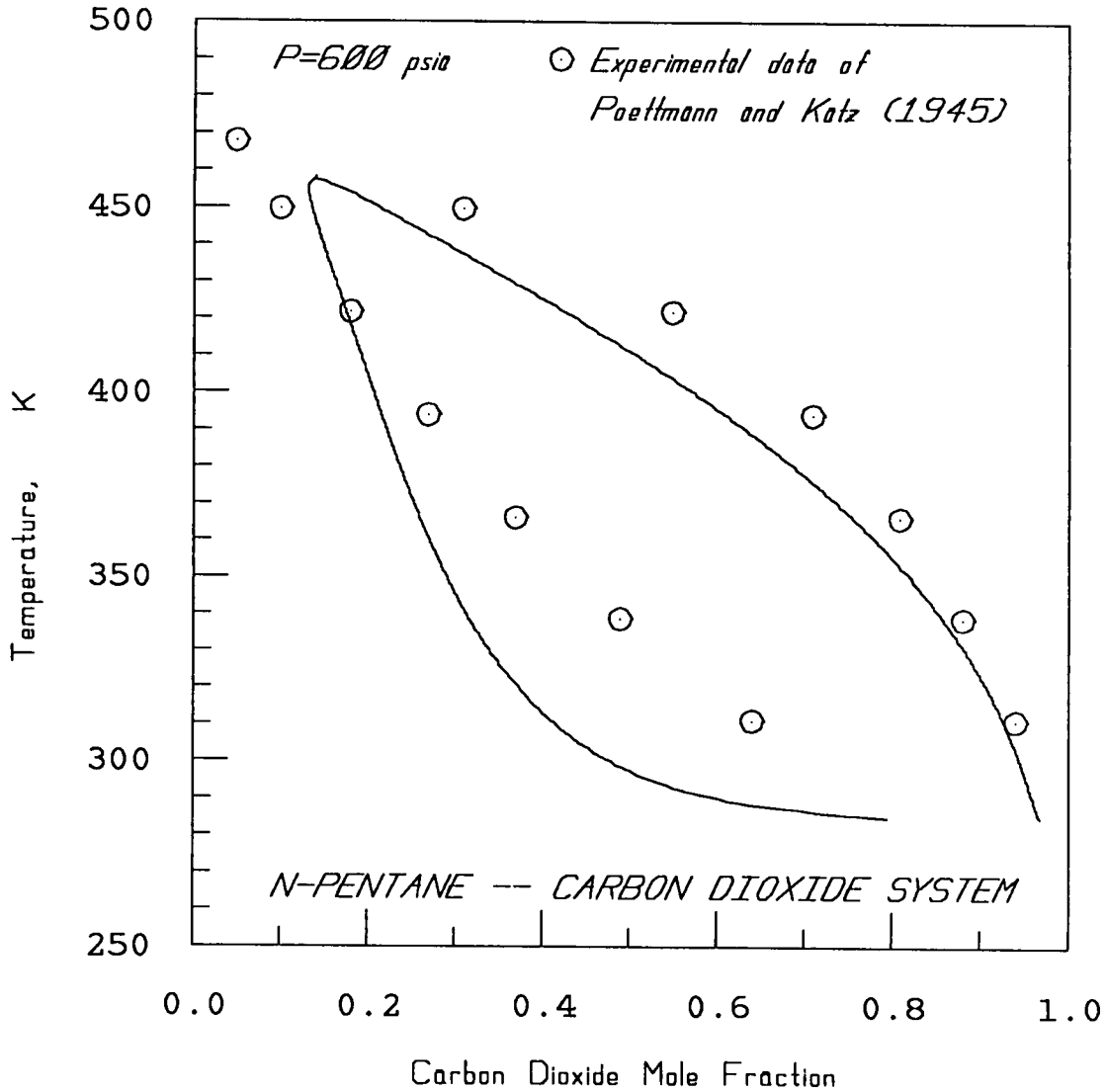

Figure 10. Comparison of theoretical equilibria from general model including ambient gas absorption with experimental data at $P_\infty = 600$ *psia* for the n-pentane—nitrogen binary system.

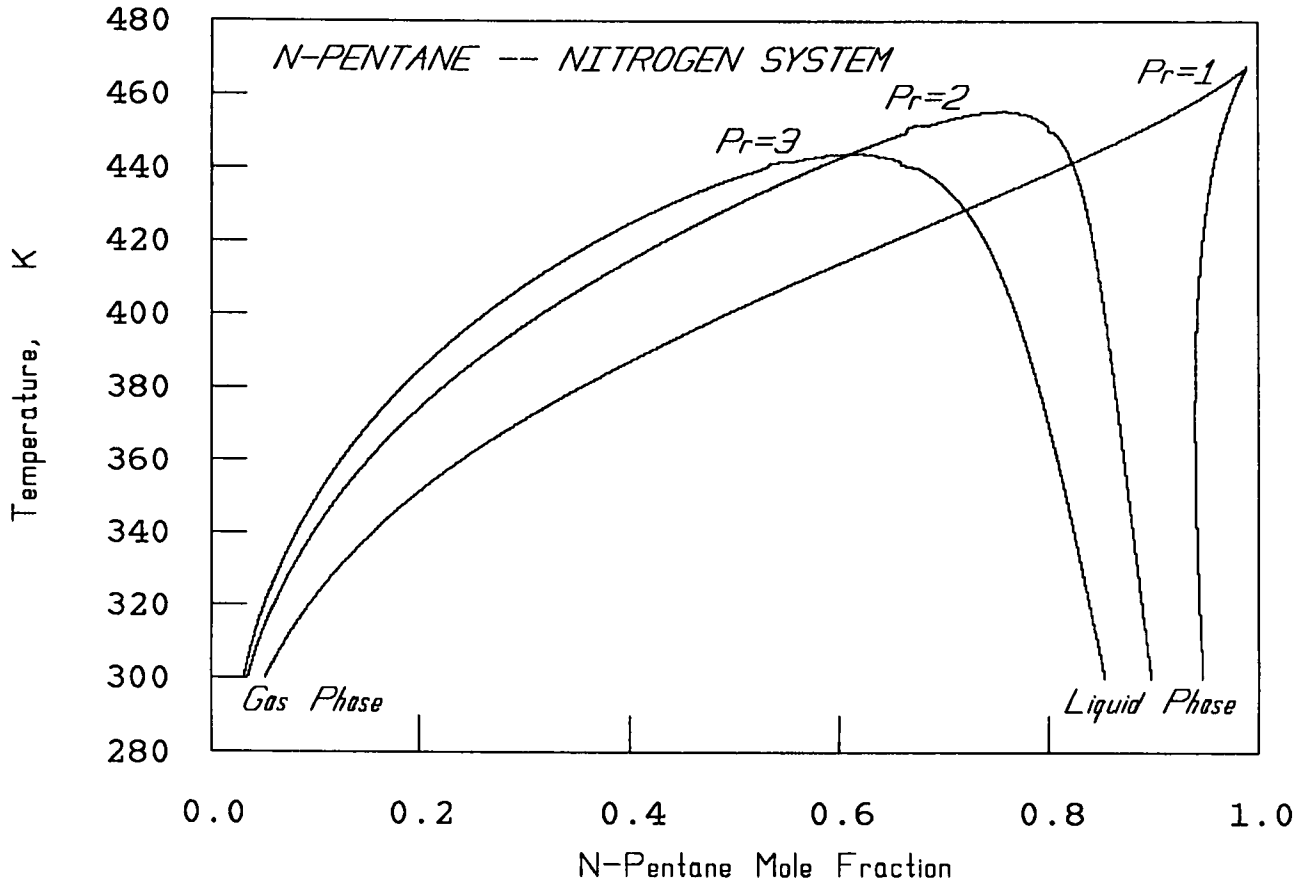

Figure 11. Theoretical equilibria from general model including ambient gas absorption at supercritical pressures for the n-pentane—nitrogen binary system.

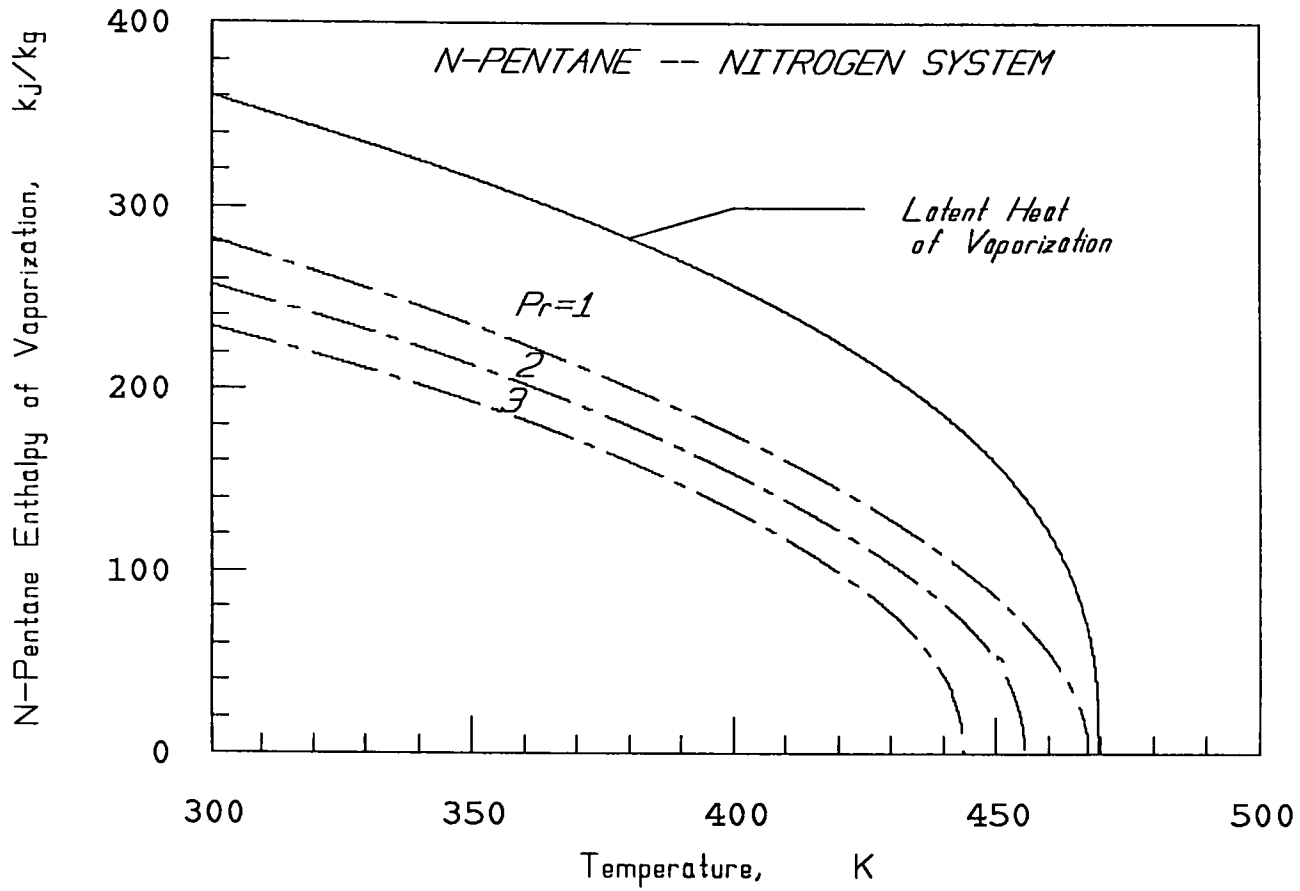

Figure 12. Comparison of theoretical enthalpy of vaporization from general model including ambient gas absorption at supercritical pressures with the latent heat of vaporization for the n-pentane—nitrogen binary system.

and that the liquid-phase concentration of n-pentane decreases due to ambient gas absorption. Figure 12 shows the enthalpy of vaporization from 300 K to the critical state for the same reduced pressures as well as the latent heat of vaporization for comparison. The actual enthalpy of vaporization deviates greatly from the low-pressure latent heat assumption, and the departure enlarges with increasing pressure. It is again clearly shown in this figure that the critical mixing temperature decreases with pressure, and the vanishing of the enthalpy of vaporization at the critical state is distinctly illustrated. Figures 11 and 12 reaffirm the importance of high-pressure, multi-component thermodynamics to the transport processes in droplet gasification theory.

4.1.2 Evaluation of Transport Model

A numerical analysis of the transport model formulated for high-pressure droplet vaporization theory requires the time dependent evaluation of the three ordinary differential equations for droplet mass, diameter, and temperature with an additional differential equation for each component of velocity under consideration. At each time step, furthermore, the heat and mass transfer coefficients must be determined from the simultaneous solution of two nonlinear, algebraic equations , and the vapor-liquid equilibria submodel must be solved for the droplet surface condition. The computational effort required for simulation is, therefore, intensive but not overwhelming for practical application as a submodel in a spray combustion code.

The general numerical procedure adopted for this study is to evaluate thermodynamic and thermophysical properties, heat and mass transfer coefficients, and vapor-liquid equilibria explicitly and assume these values hold over the numerical time step used in the solution of the governing ODE's.

A FORTRAN computer simulation code was developed based on the above procedure. At each time step the thermodynamic and thermophysical properties are evaluated explicitly, vapor-liquid equilibria is evaluated from the general model by calling the ZSPOW simultaneous equations solver of the IMSL© Software Library, the enthalpy of vaporization is calculated, and the heat and mass transfer coefficients are obtained by another call to the ZSPOW subroutine. At this point the first order governing ODE's are solved for the new time step using a Runge-Kutta 5th and 6th order method by the DEVERK differential equation solver from the IMSL© Software Library. The code repeats the process until the maximum allowable number of iterations have been reached, the droplet diameter becomes smaller than an arbitrarily specified value, or the thermodynamic critical state is reached. For 1500 cycles the code uses about 5 to 6 minutes of cpu time on the MASSCOMP 5600 computer.

Thermodynamic and thermophysical property evaluations at high-pressures required special considerations since experimental data are generally unavailable for the dense-gas regime, especially for mixtures. For this reason, semi-empirical estimation techniques described by Reid and Sherwood (1966) and Reid *et al.* (1987) were utilized to correct for mixture and high-pressure effects. The compressed liquid density of the droplet was estimated by Thompson's extension of the H-B-T method (Reid *et al.*, 1987) from which the temperature derivative of liquid density was also approximated. Where experimental data for the pure component liquid vapor pressure was not available, the Lee-Kesler method as described by Reid *et al.* (1987) was employed, and the liquid-phase specific heat was estimated using a corresponding states method (Reid *et al.*, 1987). Mixture gas-phase specific heat was obtained from the mole fraction average where the pure component specific heats were calculated with the ideal-gas curve fits of Reid *et al.* (1987). Lucas' corresponding

states method for low-pressure, pure-component, gas-phase viscosities (Reid *et al.*, 1987) applied in Wilke's method gave a mixture viscosity which was corrected for high-pressure effects by the Dean-Stiel dense-gas correlation (Reid and Sherwood, 1966). In a similar procedure, the low-pressure, pure-component, gas-phase thermal conductivities were calculted using Chung's method (Reid *et al.*, 1987), mixture thermal conductivity was obtained from the Mason-Saxena formulation (Reid and Sherwood, 1966), and the Stiel-Thodos dense-gas correlation provided a correction for high-pressure effects (Reid and Sherwood, 1966). A theoretical formulation was employed for the low-pressure diffusion coefficient with a rough curve fit to Takahashi's graphical correlation for high-pressure corrections (Reid *et al.*, 1987). A corresponding states method was also utilized for an estimate of the surface tension (Reid *et al.*, 1987).

In addition, the constant property assumption of the formulated transport theory requires that effective values for the gas-phase temperature and composition be obtained for use in property evaluations. A weighted average effective value was determined according to the expression (Mao, 1980; Solomon, 1984)

$$\phi_{eff} = \alpha\phi_s + (1-\alpha)\phi_\infty \tag{4.1}$$

where in this study $\alpha = 0.75$ as suggested by Solomon (1984).

To validate the model, experimental data was sought for comparison with computational results. The test case chosen was for droplets undergoing natural-convective, pure vaporization over a wide range of pressures as forced convective data is unavailable. Experimental data was obtained from Matlosz *et al.* (1972) and Kadota and Hiroyasu (1976) for suspended droplets in a hot, stagnant, pressurized gas. Matlosz and coworkers reported some results for n-hexane droplets in nitrogen

gas while Kadota and Hiroyasu studied n-heptane droplets in nitrogen gas; both groups investigated the vaporization behavior over a range of pressures below, near, and above the fuel critical pressure.

A comparison of the calculated and experimental droplet diameter and temperature histories are given in Figures 13 and 14 for the data of Matlosz and his coworkers and in Figures 15–17 for the data of Kadota and Hiroyasu. The Ranz/Marshall correlation for natural convection, as given in equation (3.47), and the general vapor-liquid equilibria model with ambient gas absorption were employed for all calculations. In the figures, circular symbols denote droplet size data while triangular symbols denote temperature data.

The cases for n-hexane vaporization in nitrogen gas for reduced pressures of $P_r = 0.682$ and $P_r = 2.73$ are given in Figures 13 and 14, respectively. For both pressures the calculated histories agree reasonably well with experimental histories during the early part of the lifetime; however, there is an increasing deviation with time such that the calculated history overestimates the experimental lifetime of the droplet significantly, especially at the higher pressure. This is probably due primarily to heat conduction through the thermocouple wires and radiation from the furnace walls both of which were neglected in the computations. Because the drops were not much larger than the thermocouple bead upon which they were suspended, the conduction effect was probably not negligible. For the reduced pressure of $P_r = 0.682$, the calculated and experimental results both show a steady-state temperature although the calculated value is about 20 K less than the reported experimental value. This anomaly is presumably attributal to an inaccuracy in the estimation of thermodynamic and thermophysical properties. For the case of a reduced pressure of $P_r = 2.73$, the experimental and calculated temperatures both show a continuous increase throughout the droplet lifetime and both share the same

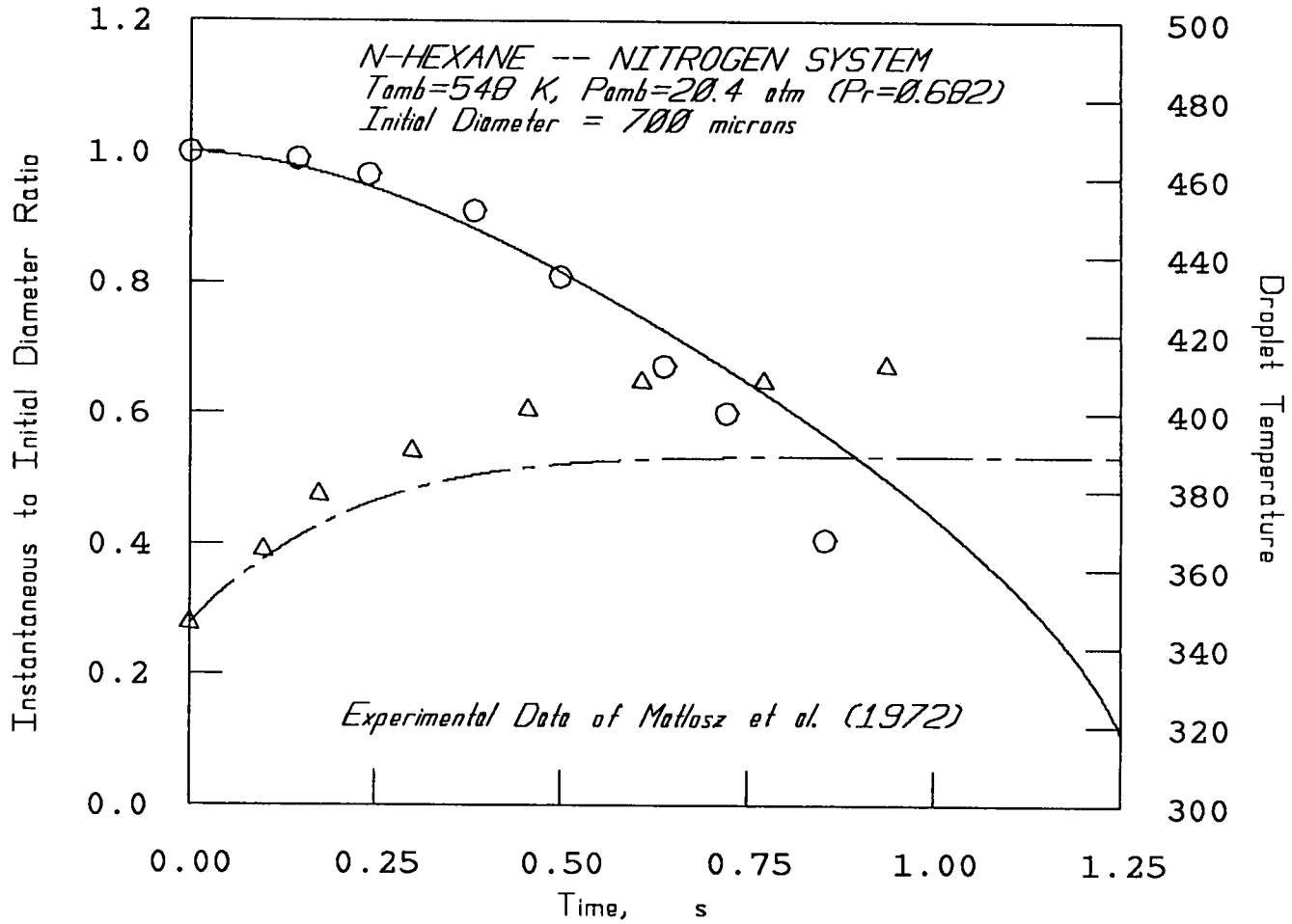

Figure 13. Comparison of theoretical and experimental vaporization histories of n-hexane droplet in nitrogen gas at 548 K and 20.4 atm.

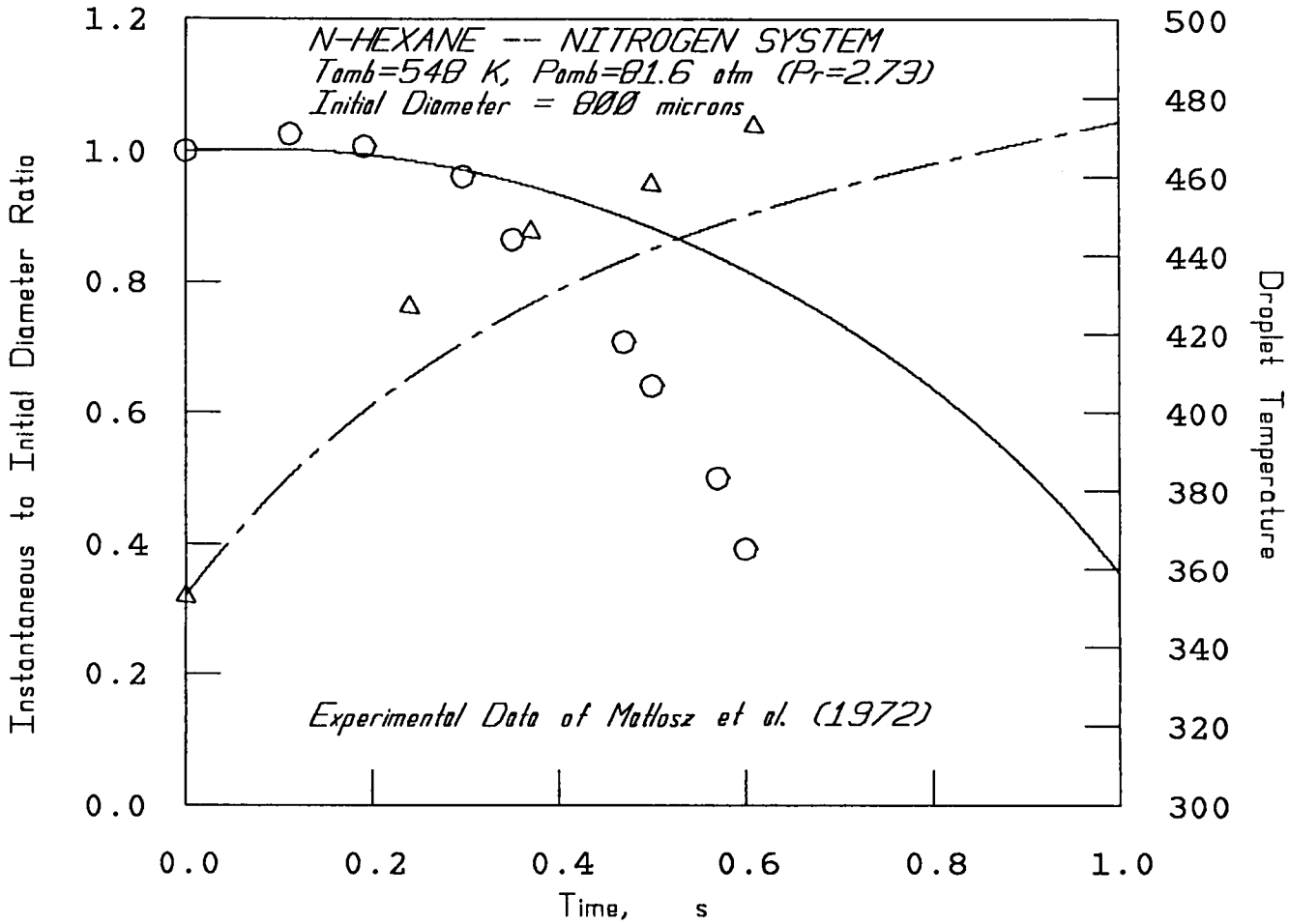

Figure 14. Comparison of theoretical and experimental vaporization histories of n-hexane droplet in nitrogen gas at 548 K and 81.6 atm.

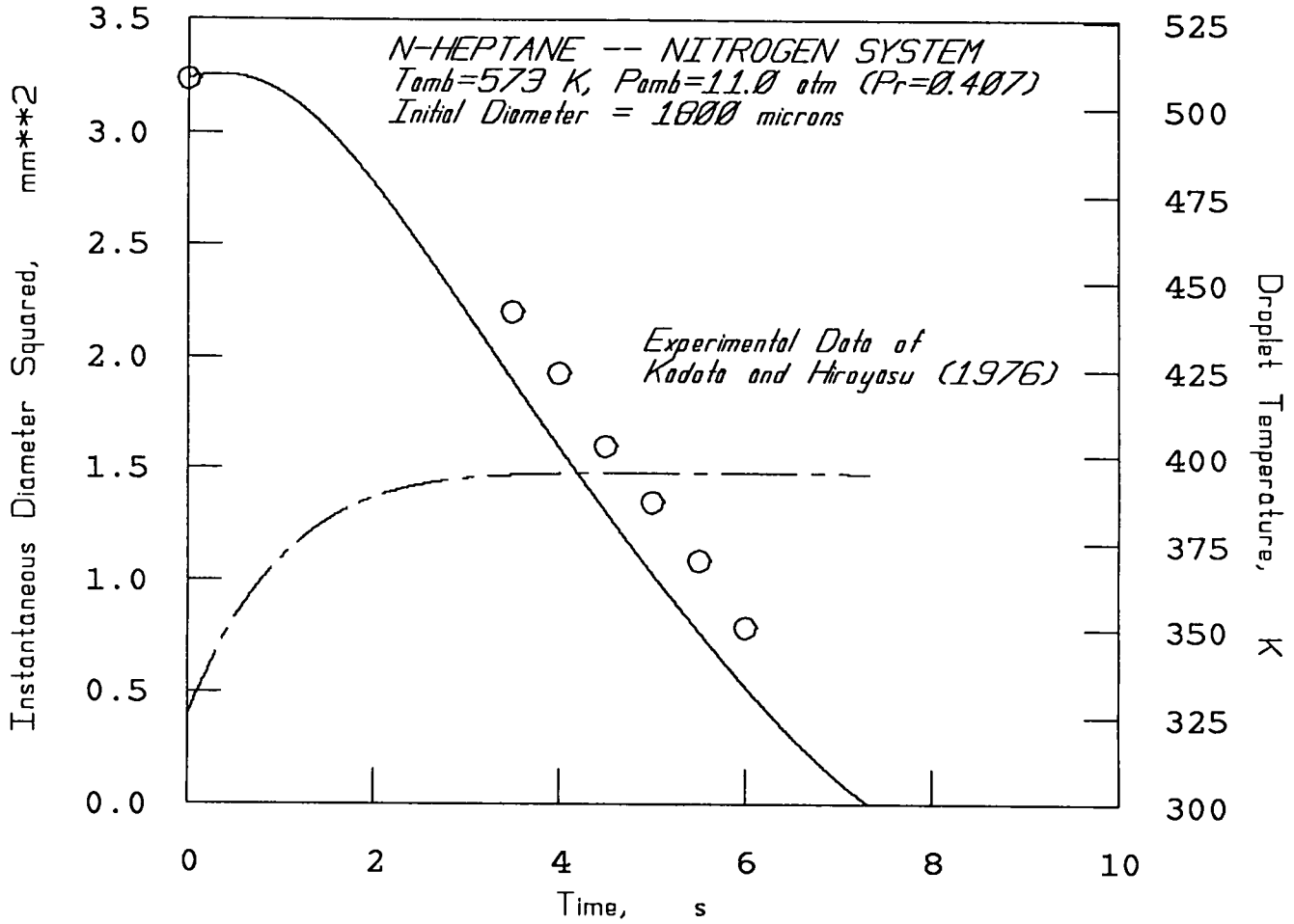

Figure 15. Comparison of theoretical and experimental vaporization histories of n-heptane droplet in nitrogen gas at 573 K and 11 atm.

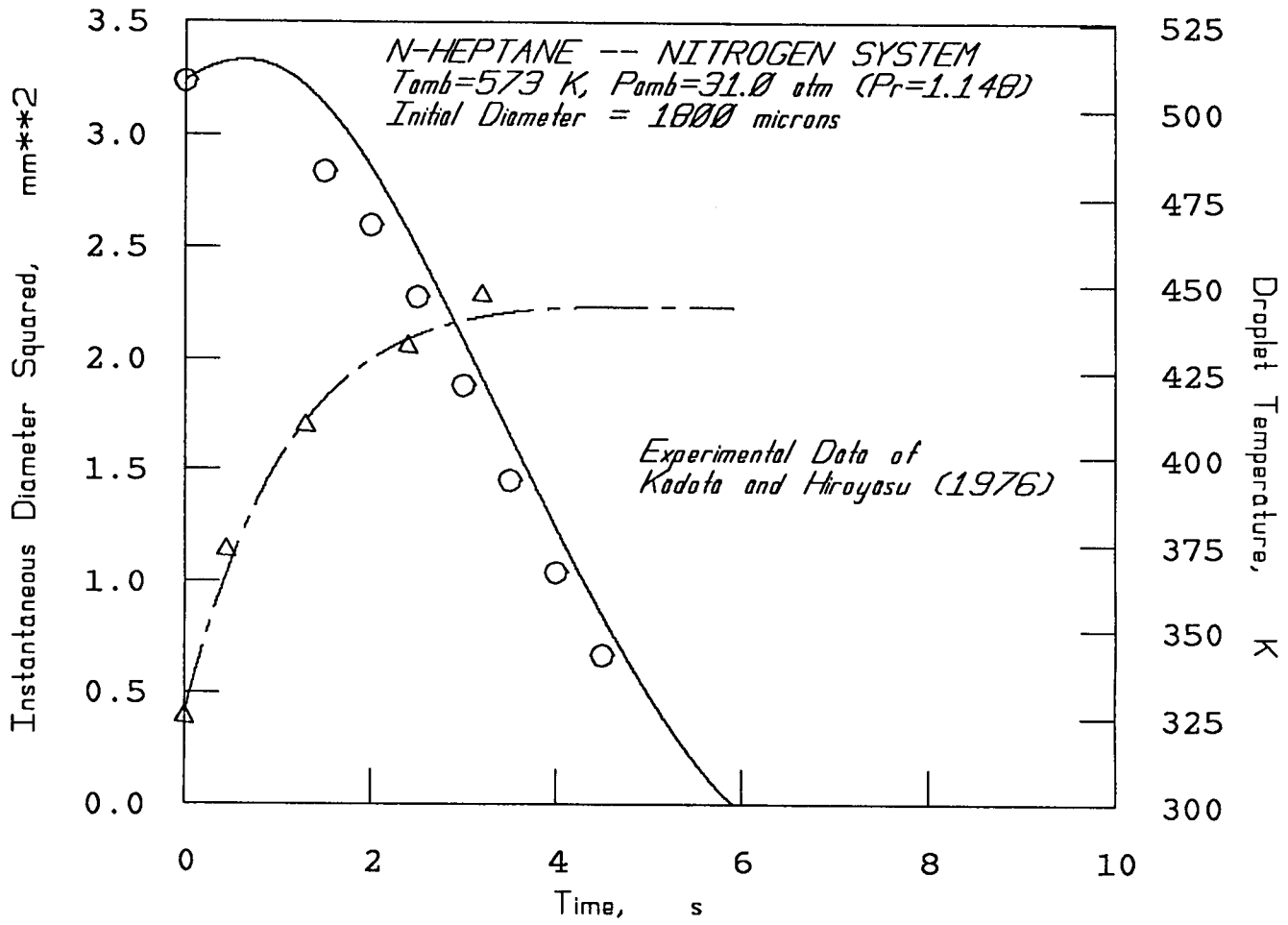

Figure 16. Comparison of theoretical and experimental vaporization histories of n-heptane droplet in nitrogen gas at 573 K and 31 atm.

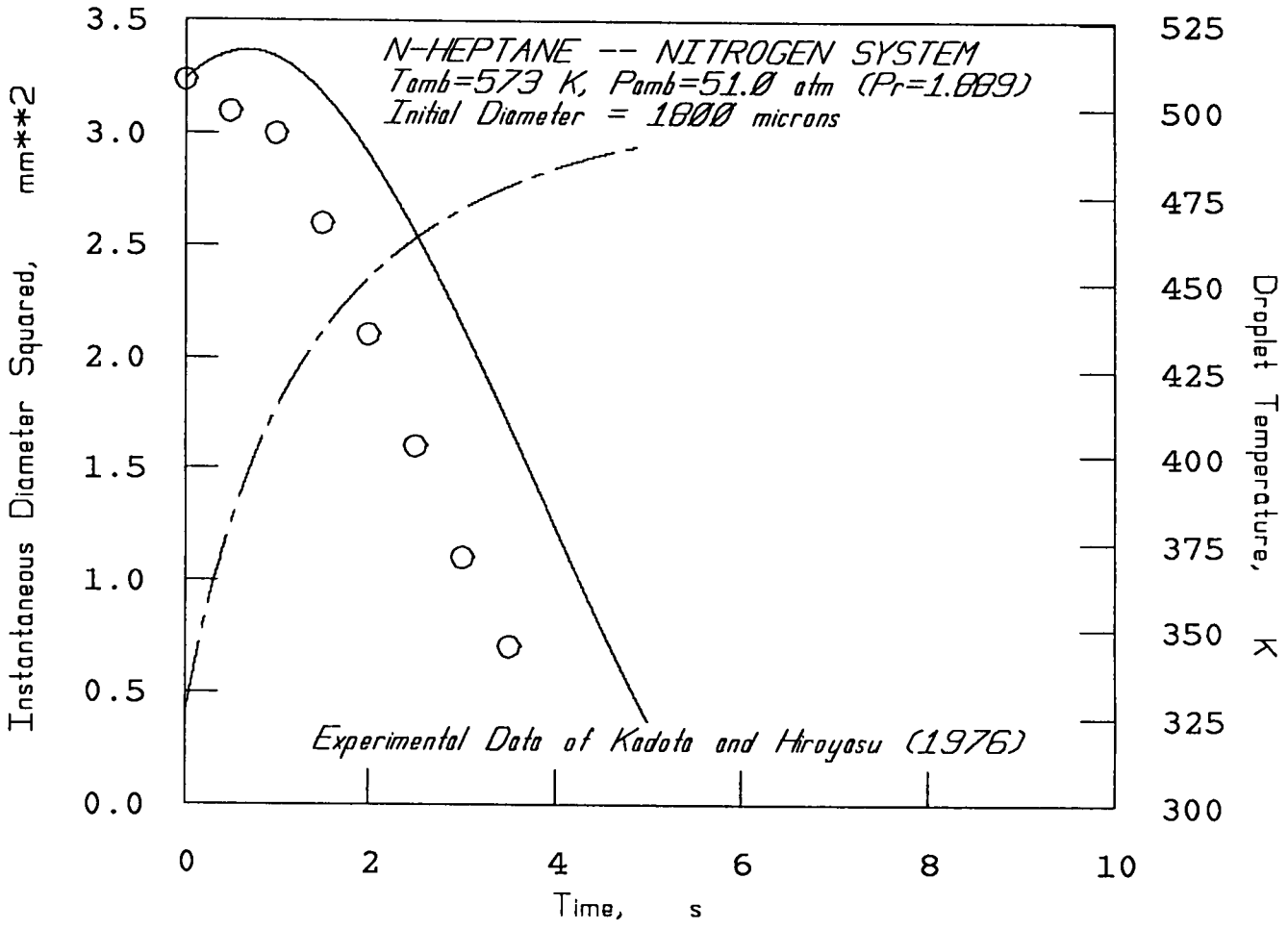

Figure 17. Comparison of theoretical and experimental vaporization histories of n-heptane droplet in nitrogen gas at 573 K and 51 atm.

limiting temperature extreme. Overall, theory follows the correct trends shown by Matlosz's data while there is a tendency to overestimate the drop lifetime.

The cases for n-heptane vaporization in nitrogen gas for reduced pressures of $P_r = 0.407$, $P_r = 1.148$, and $P_r = 1.889$ are given in Figures 15–17, respectively. Theoretical predictions agree with the experimental data of Kadota and Hiroyasu much better than that of Matlosz, even though no corrections were made for heat conduction and radiation errors. Since the droplets were initially much larger than the thermocouple bead in these cases, it is surmised that the conduction error is less than that encountered in the experimental set-up of Matlosz. However, Kadota and Hiroyasu have estimated that the combined heat conduction and radiation errors in their experiments could shorten the droplet lifetime by up to 15% . The agreement between the computed and measured temperature history for a reduced pressure of $P_r = 1.148$ in Figure 16 is very good with excellent correspondence for the steady-state temperature. In addition, droplet size calculations compare reasonably well with experiment although there is a tendency to overestimate the droplet lifetime at increasingly higher pressures.

The favorable comparison between theory and experiment indicates the basic validity of the formulated high-pressure droplet vaporization model. Despite a proclivity toward underestimating the rate of development of the process, the theory displays the correct quantitative and qualitative trends for droplet size and temperature histories.

4.2 PRESSURE DEPENDENT PARAMETRIC BEHAVIOR: HIGH-PRESSURE DROPLET VAPORIZATION THEORY

With the basic validity of the transport model established, a study of param-

eter pressure dependence is warranted. The nonlinear nature of the mathematical equations describing the physical phenomena makes direct extraction of pressure dependent parametric behavior impossible; however, transient behavior under different ambient pressures can be examined through numerical simulation of droplet vaporization in a combustor environment. Since the interest here is on the effect of pressure, the ambient temperature and composition which the droplet experiences are kept constant while the ambient pressure is changed for each simulation.

To make the calculations physically realistic and characteristic of droplet vaporization in a practical combustor, environmental and droplet conditions representative of fuel vaporization in a Diesel engine were selected. In this case, a $20\mu m$ n-pentane fuel droplet initially at 300 K is suddenly exposed to a constant relative velocity of 50 m/s in a hot nitrogen rich gas at 900 K. The effective ambient fuel concentration is considered to be zero for simplicity, and deformation and breakup processes are neglected. Furthermore, the n-pentane fuel is assumed to be in thermodynamic phase equilibrium with nitrogen only. Calculations are made for reduced pressures of $P_r = 0.5$, $P_r = 1$, and $P_r = 2$, and the transient histories of relevant parameters are stored in computer files from which they can be read and displayed graphically.

The computations were carried out on the MASSCOMP 5600 computer, and time iterations were continued until the droplet diameter became less than $3\mu m$. Since it is possible for the critical state to be reached for sufficiently high supercritical pressures, the code was modified to continue running even if the critical state was attained. This was accomplished by setting the time derivative of droplet temperature to zero once the heat of vaporization became negligibly small. In this way, finite rate vaporization could be enforced until the drop was completely evaporated. Although the above procedure is a gross simplification of the actual process,

it allows for a more extended comparison with the cases where the critical state is not reached. In the graphs to follow, parameter behavior after the enforcement of finite rate vaporization at the critical state will be shown by short dashed lines.

The two parameters of foremost interest, transient droplet size and temperature, are shown in Figures 18 and 19, respectively. Here, the droplet size is represented as the instantaneous diameter squared normalized by the initial diameter squared. From these graphs one immediately sees that the droplet gasification lifetime decreases with the ambient pressure. This may at first be puzzling as it seems to violate the intuitive notion that mass transfer from the droplet should decrease as the equilibrium surface gas-phase concentration decreases with increasing pressure, but careful examination will reveal that heat transfer processes can become the dominant, controlling factor for the vaporization rate. Indeed, from a vapor-liquid equilibria diagram such as Figure 11, the surface equilibria concentration of fuel is seen to decrease with an increase in pressure for a given temperature; however, from Figure 12 it is also quite obvious that the heat energy required to vaporize a given mass of fuel is in turn decreasing substantially with increasing pressure. For a sufficiently high ambient temperature, therefore, the actual vaporization rate increases with pressure because the effect of a greatly reduced enthalpy of vaporization is much more dominant than the slight reduction in the surface equilibrium fuel concentration. If the ambient temperature is low enough that heat transfer to the drop is small, then one could expect an increase in the droplet lifetime with pressure, but combustors do not operate at low temperatures negating any practical interest in this low temperature regime.

Other interesting information from Figure 18 includes the recovery of a diameter-squared gasification law at all investigated pressures after an initial droplet heat-up starting transient. The use of such a d^2 law for prediction of the drop size history is

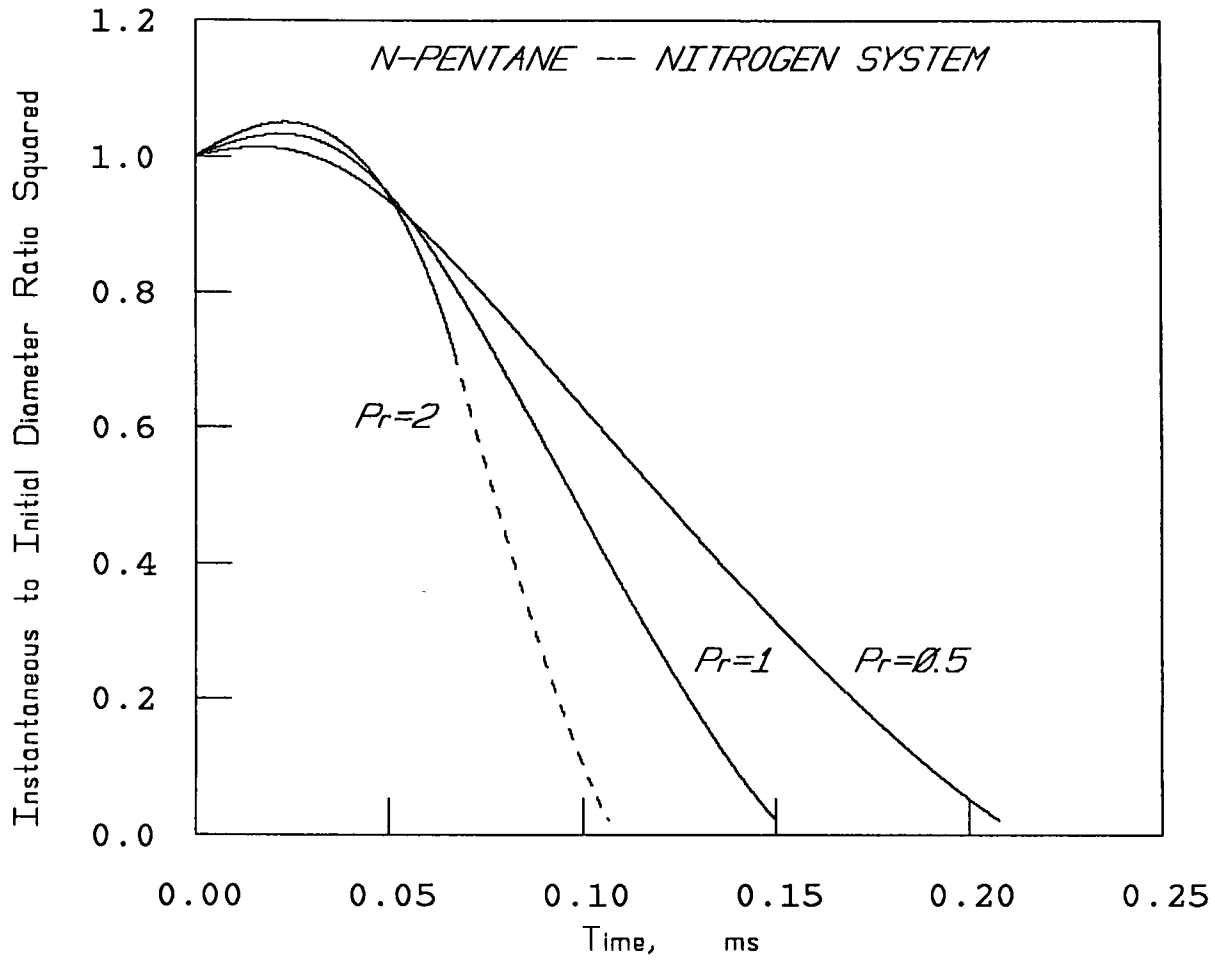

Figure 18. Calculated $d_d^2/d_{d_0}^2$ ratio histories at different ambient pressures for n-pentane drop in N_2.

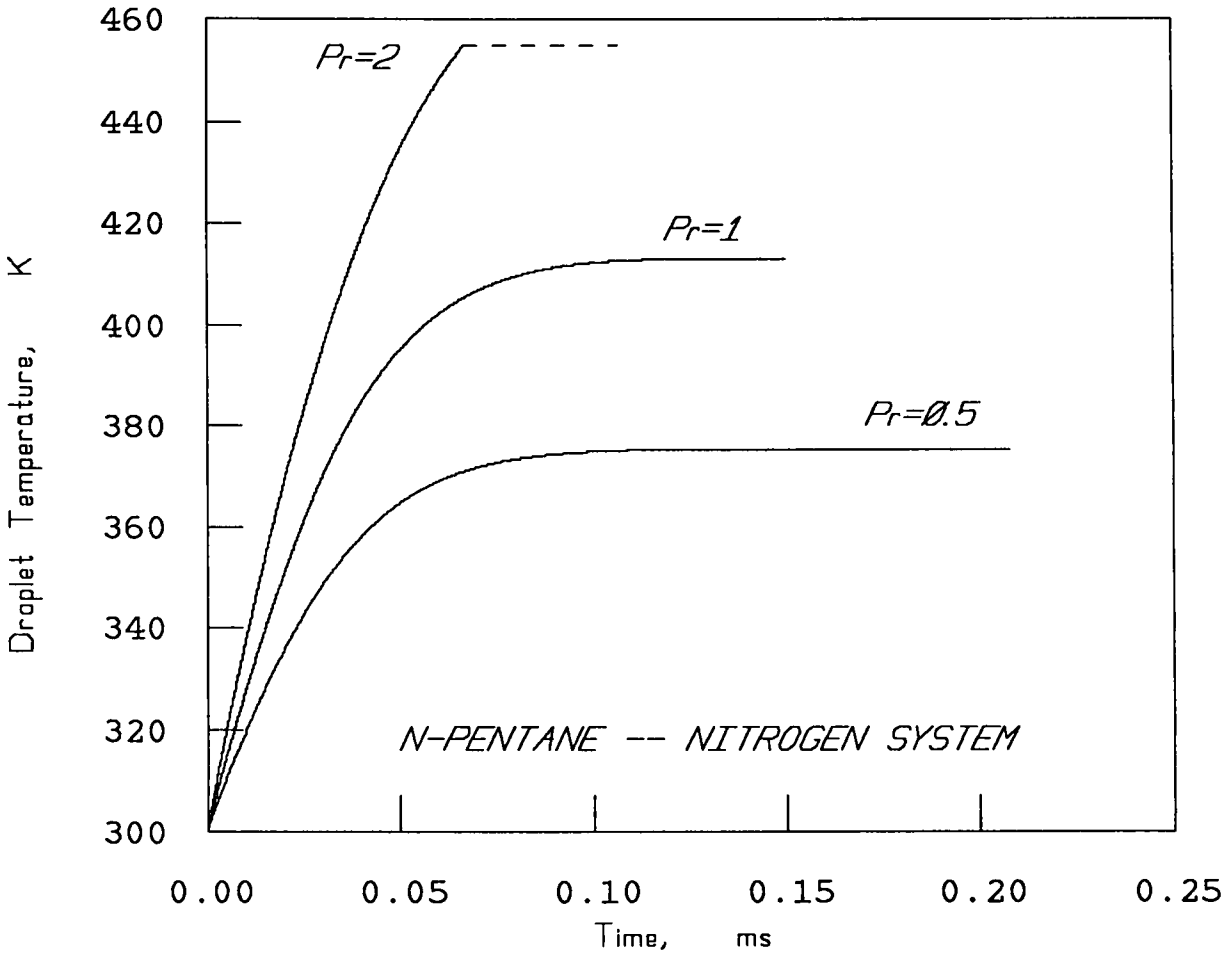

Figure 19. Calculated droplet temperature histories at different ambient pressures for n-pentane drop in N_2.

not valid, however, as it is also evident that the starting transient occupies a large portion of the total droplet lifetime. Furthermore, theory predicts thermal expansion of the droplet during initial heat-up. While this effect may be exaggerated by the infinite conductivity assumption, the qualitative trend indicates the effect is probably important in the accurate prediction of droplet tracking and breakup atomization.

In Figure 19 thermal history pressure dependence is illustrated very succinctly. For a reduced pressure of $P_r = 0.5$ the attainment of a steady-state temperature is evident, and steady-state gasification occupies a significant portion of the droplet lifetime. With a reduced pressure of unity, a steady-state temperature is again attained, but steady-state gasification occurs over a much smaller time span. Finally, for a reduced pressure of $P_r = 2$, the droplet heats continuously through the critical state. This phenomenon is primarily the result of reduced enthalpy of vaporization with increasing pressure, which can occur to such an extent that the heat transfer to the droplet always exceeds the energy consumed in vaporization. The threshold pressure for continuous heat-up to the critical state is somewhat larger than the pure component critical pressure but less than twice the critical pressure. The exact value depends upon the heat transfer characteristics. It is important to note also that the critical mixing temperature is less than the pure componet critical temperature as seen from a comparison of Figure 19 for $P_r = 2$ and Figure 12.

The ratio of the instantaneous to initial droplet mass is given in Figure 20, and the instantaneous gasification flux is shown in Figure 21. The droplet mass is seen to decrease slowly very early in the heat-up period followed by a rapid decrease that is almost linear in time. Toward the end of the droplet lifetime, the rate of decrease of droplet mass is slowed because of reduced surface area. Note for the supercritical case, $P_r = 2$, that over 40% of the initial droplet mass remains when the critical state

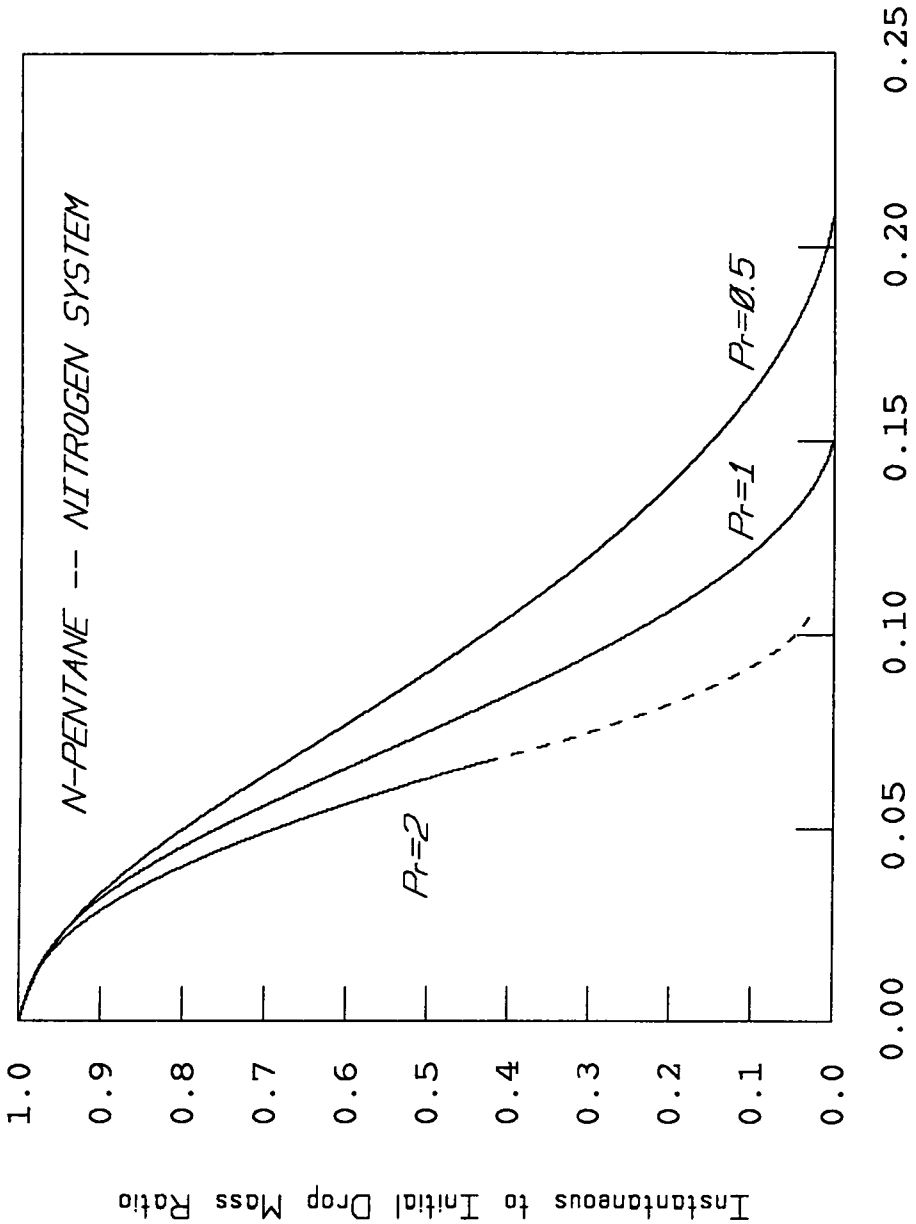

Figure 20. Calculated m_d/m_{d_0} ratio histories at different ambient pressures for n-pentane drop in N_2.

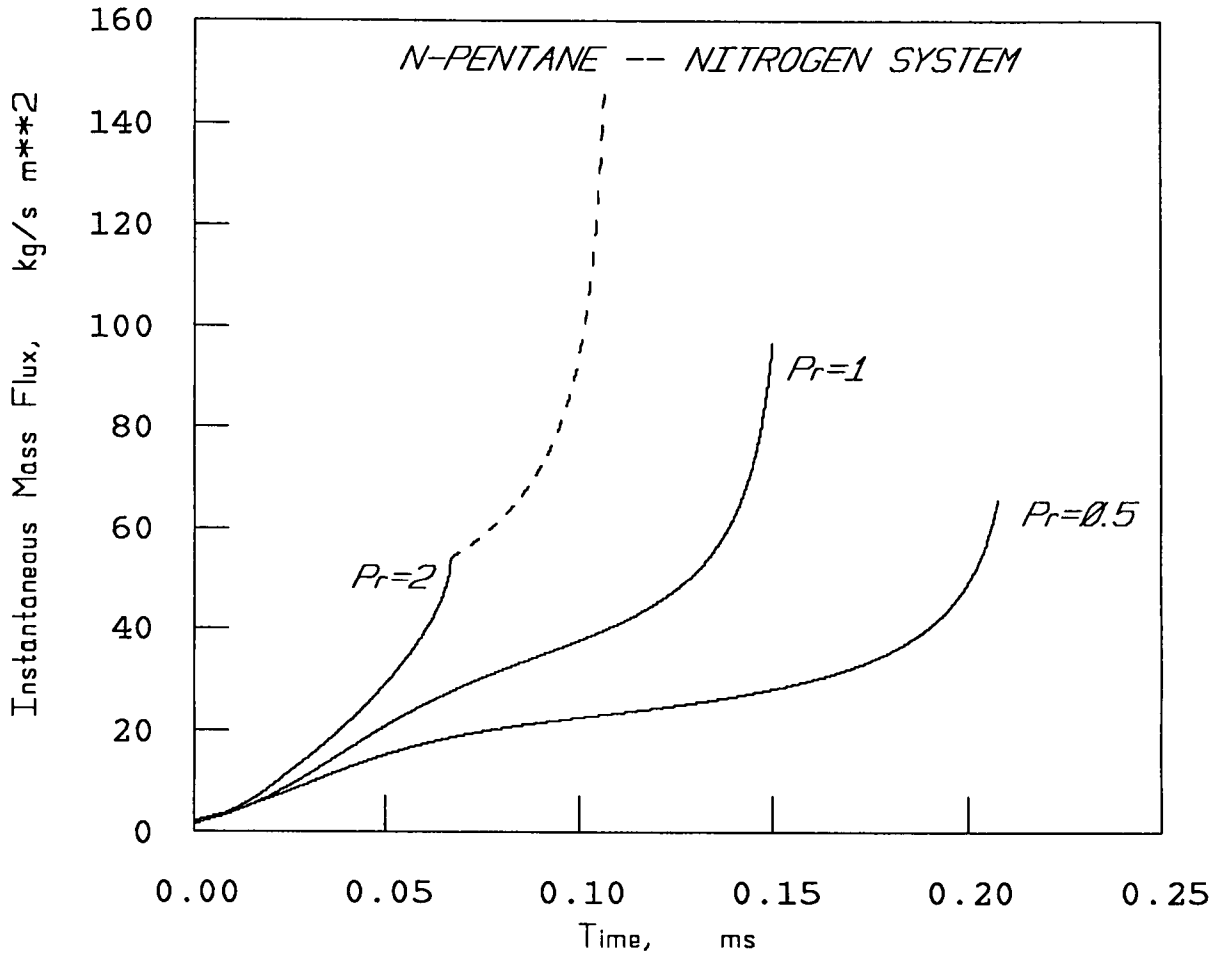

Figure 21. Calculated vaporization mass flux histories at different ambient pressures for n-pentane drop in N_2.

is reached. Certainly, the correct prediction of the gasification rate after the droplet surface reaches the critical state is of major importance in high-pressure combustor modeling since it becomes the rate controlling parameter for a significant portion of the droplet lifetime. The vaporization mass flux shows an initial increase with a leveling off in the steady state region followed by a rapid increase near the end of the droplet lifetime for $P_r = 0.5$ and $P_r = 1$. For continuous heating to the critical state with $P_r = 2$, the mass flux rises at a continuously increasing rate.

Instantaneous heat transfer and mass transfer coefficients are shown in Figures 22 and 23, respectively. The heat transfer coefficient shows a decrease with time because of the decreasing temperature difference between the surface and the ambient environment followed by a rise with time as the droplet diameter recedes. The mass transfer coefficient, with the exception of $P_r = 2$, shows little change with time except for a large increase near the end of the droplet lifetime as the diameter decreases. The odd behavior of the mass transfer coefficient for $P_r = 2$ can be attributed to an abrupt change in the diffusion coefficient estimation method with increasing gas-phase temperature.

In order to demonstrate more vividly the unique high-pressure characteristics of continuous droplet heating to the critical state, the transient convective heat transfer flux to the droplet, and the transient heat flux from the droplet consumed in vaporization, are examined for reduced pressures of $P_r = 0.5$, $P_r = 1$, and $P_r = 2$ in Figures 24–26, respectively. Recall that for attainment of a steady-state temperature, these two heat fluxes must become equal. For example, in Figure 24 for $P_r = 0.5$, Q_{in} decreases and Q_{out} increases during the heat-up period until they have the same magnitude after which a steady-state condition is maintained to complete gasification. The same trends are displayed in Figure 25 for $P_r = 1$ although the heat-up period is longer and the steady-state period is shorter in this

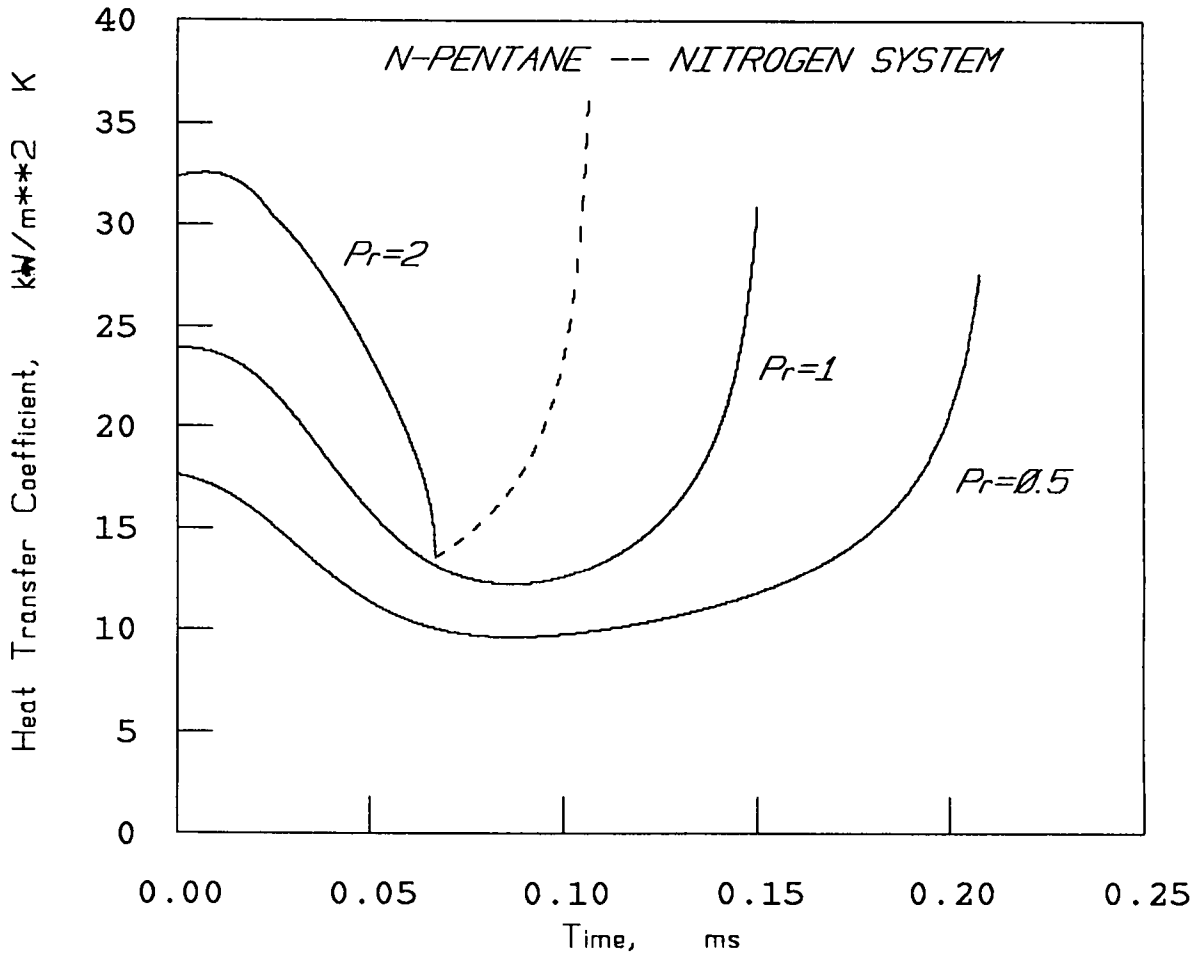

Figure 22. Calculated heat transfer coefficient histories at different ambient pressures for n-pentane drop in N_2.

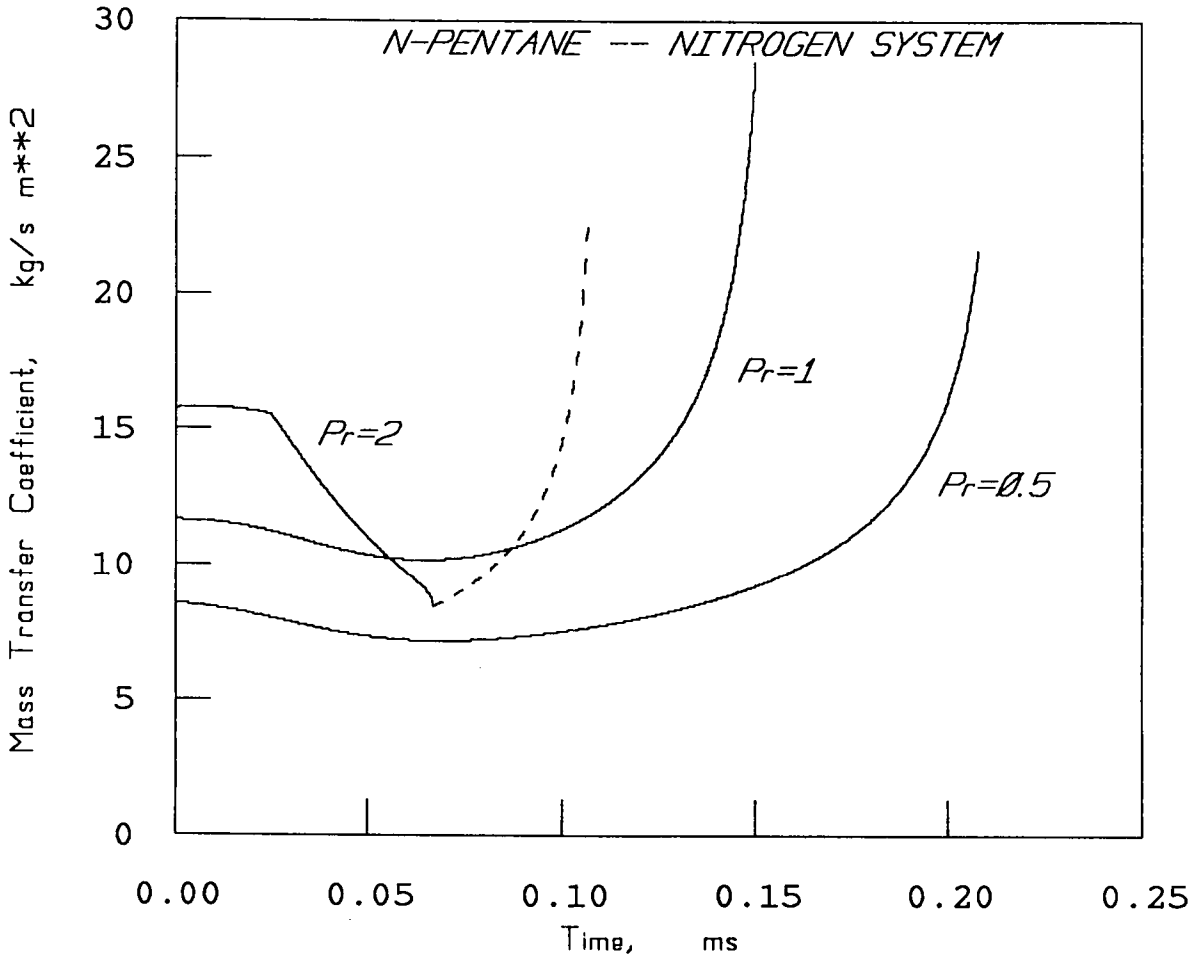

Figure 23. Calculated mass transfer coefficient histories at different ambient pressures for n-pentane drop in N_2.

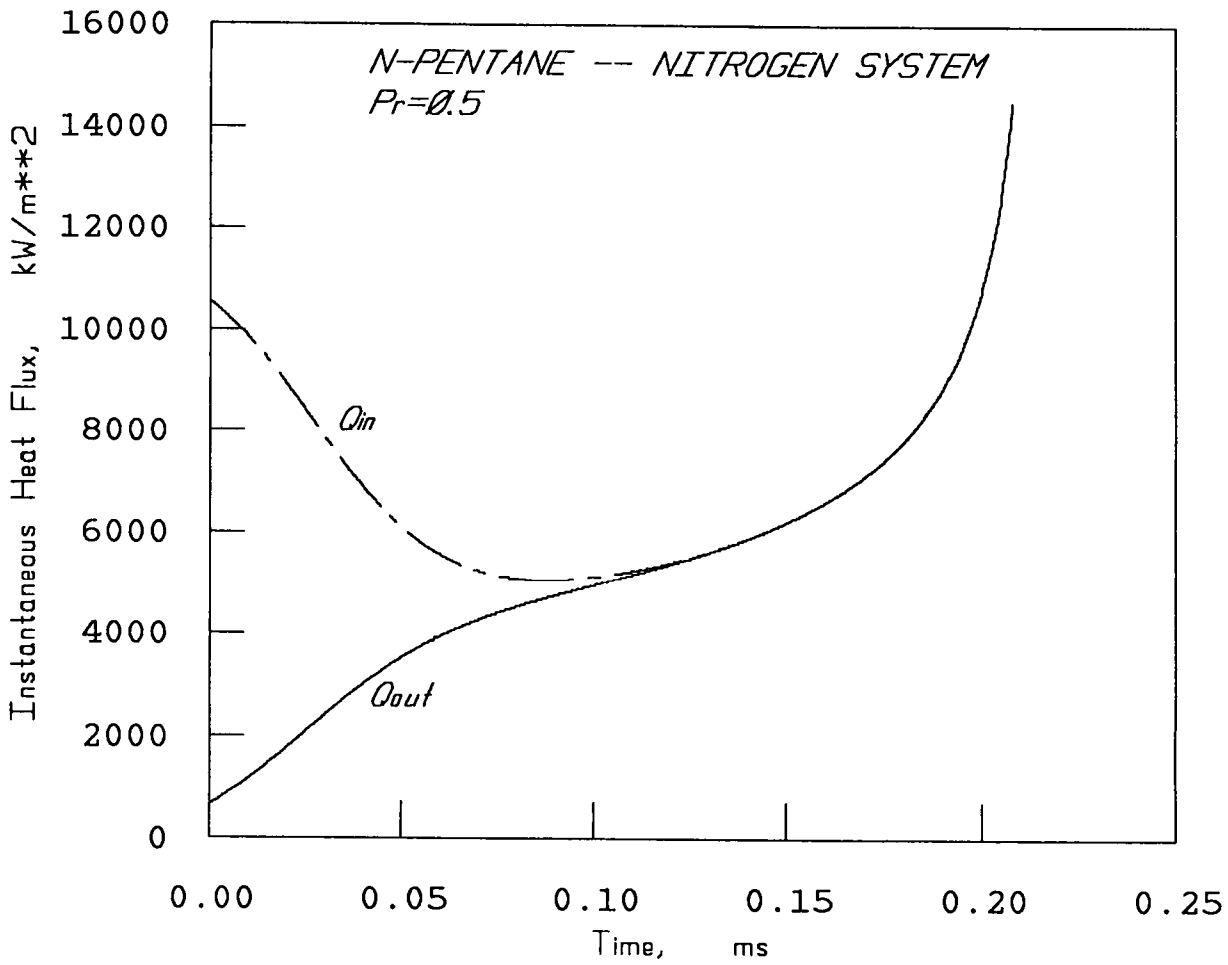

Figure 24. Calculated heat flux histories at $P_r = 0.5$ for n-pentane drop in N_2.

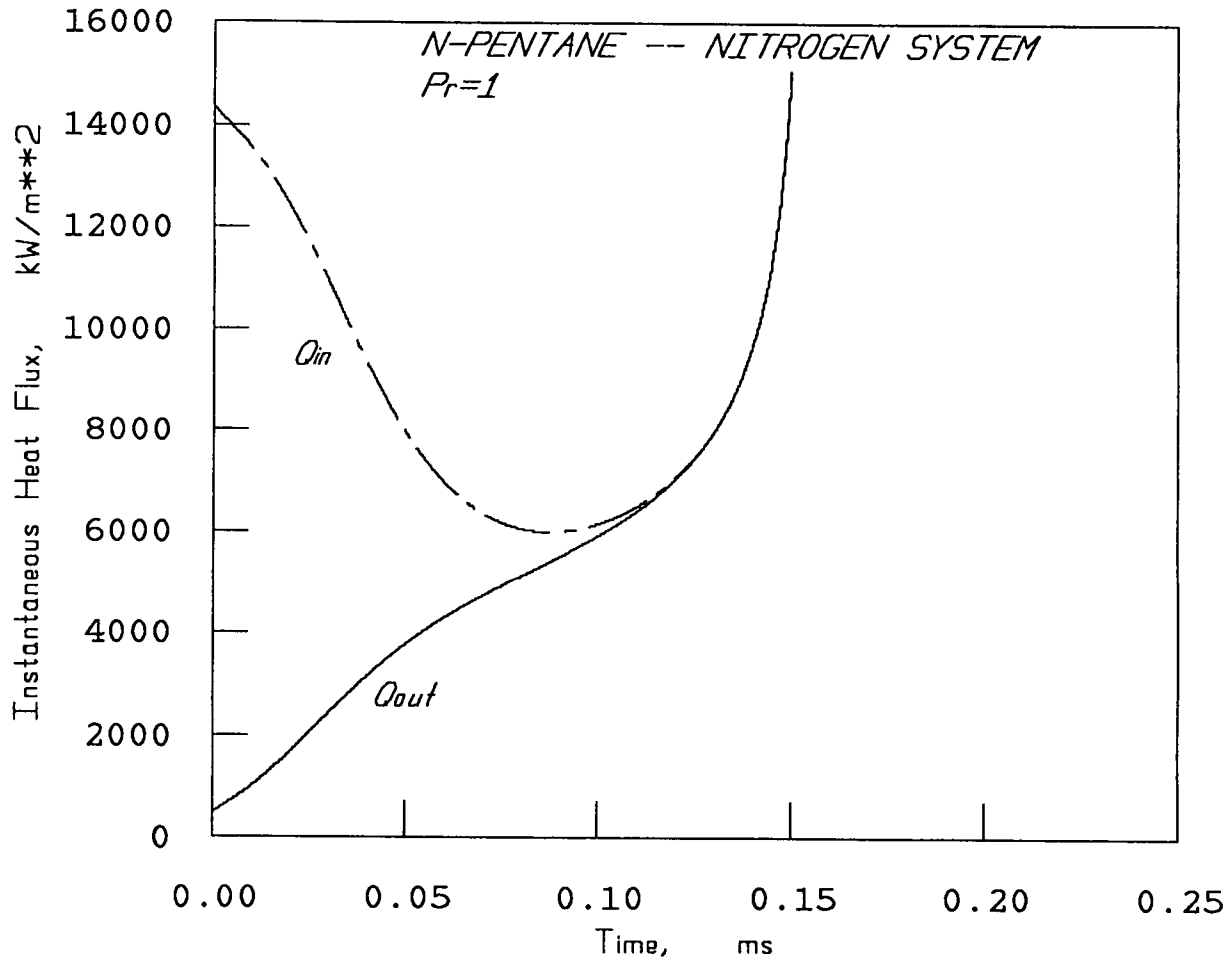

Figure 25. Calculated heat flux histories at $P_r = 1$ for n-pentane drop in N_2.

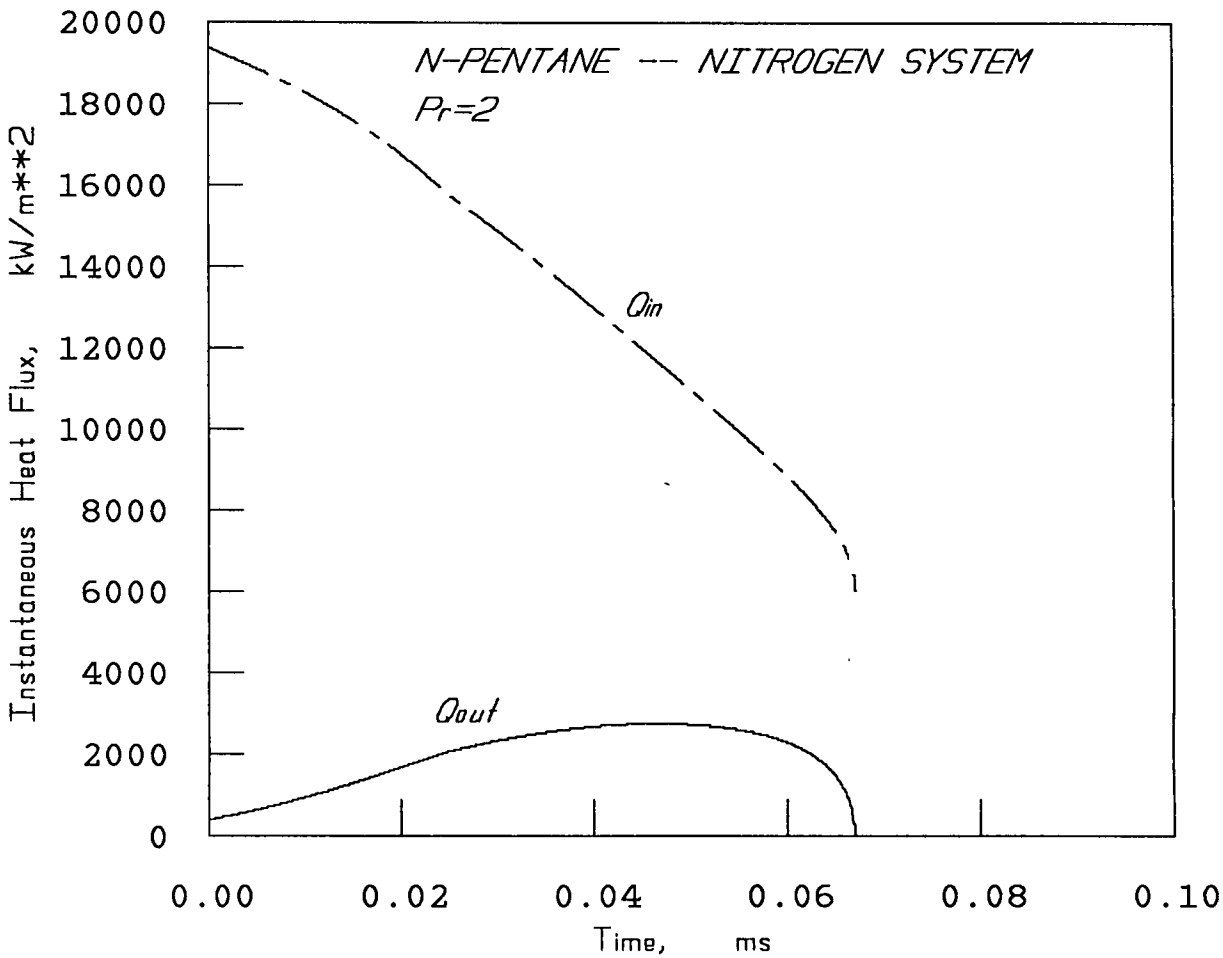

Figure 26. Calculated heat flux histories at $P_r = 2$ for n-pentane drop in N_2.

case. But for a reduced pressure of $P_r = 2$, steady-state conditions are unattainable as Q_{out} reaches a maximum value much less than Q_{in} whereupon it decreases to zero at the critical state. This behavior is the direct result of a greatly reduced enthalpy of vaporization at such a highly over-critical pressure.

The transient mass transfer B number and surface regression parameter ζ are shown in Figures 27–29 for reduced pressures of $P_r = 0.5$, $P_r = 1$, and $P_r = 2$, respectively. From the figures, one sees that the B number increases with time to a steady-state value for $P_r = 0.5$ and $P_r = 1$ and that it increases continuously to the critical state for $P_r = 2$. Note that the B number has steady-state values only slightly greater than 3 while it exceeds 6 at the critical state. The general behavior of the surface regression parameter is to have an initially positive value as the droplet expands and to become negative once the droplet size begins to decrease with time; when $\zeta = 0$, transition from expansion to regression occurs. The higher the ambient pressure the greater the initial and final magnitudes of ζ.

The Prandtl , Lewis, and Schmidt numbers are also shown in Figures 30–32 for reduced pressures of $P_r = 0.5$, $P_r = 1$, and $P_r = 2$, respectively. The Prandtl number tends toward unity in all cases, and the Lewis and Schmidt numbers approach values less than unity. The deviation from steady-state values at time zero increases with ambient pressure. The odd behavior of the Lewis and Schmidt numbers at $P_r = 2$ is again attributed to a sudden change in the diffusion coefficient estimation method.

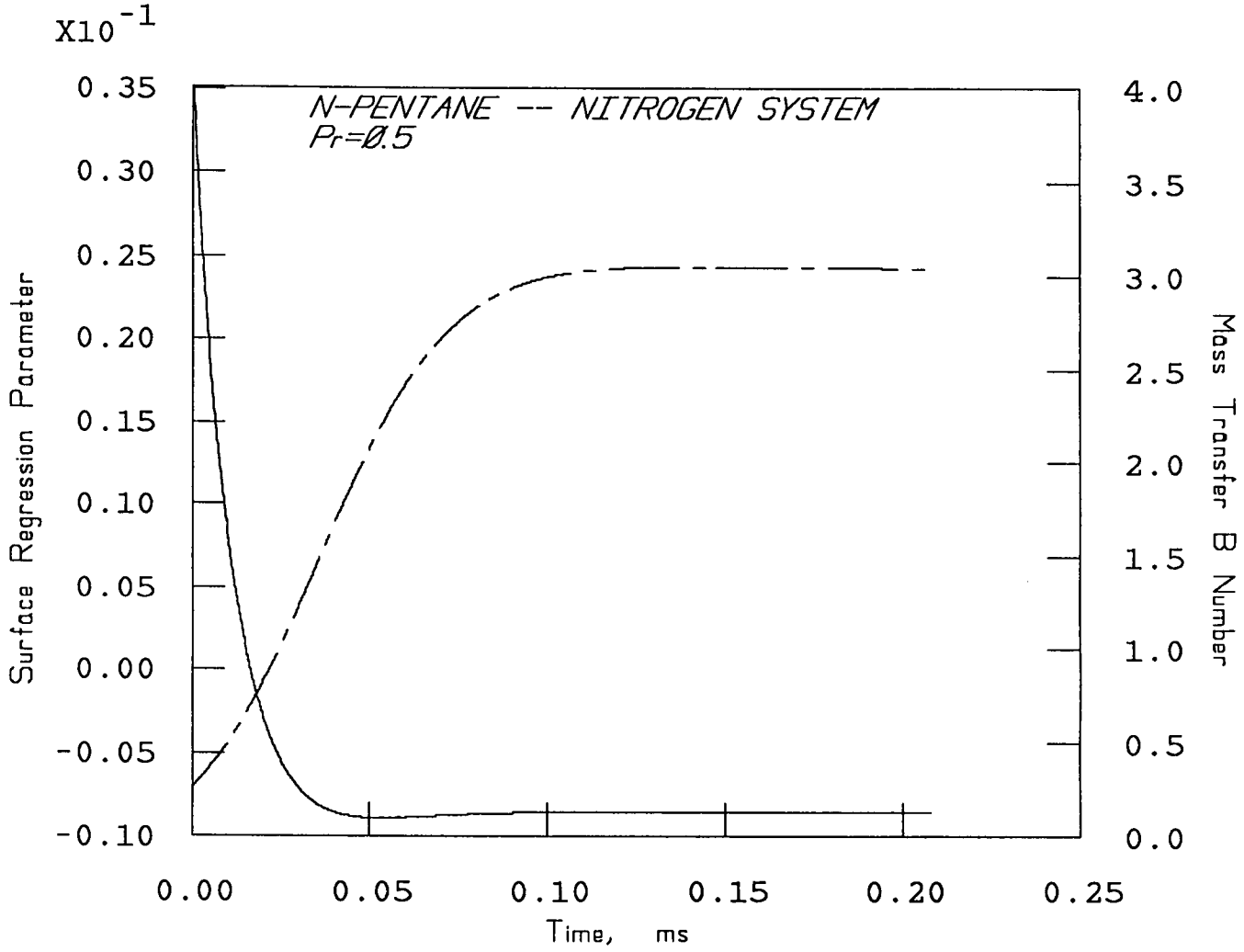

Figure 27. Calculated surface regression parameter and mass transfer B number histories at $P_r = 0.5$ for n-pentane drop in N_2.

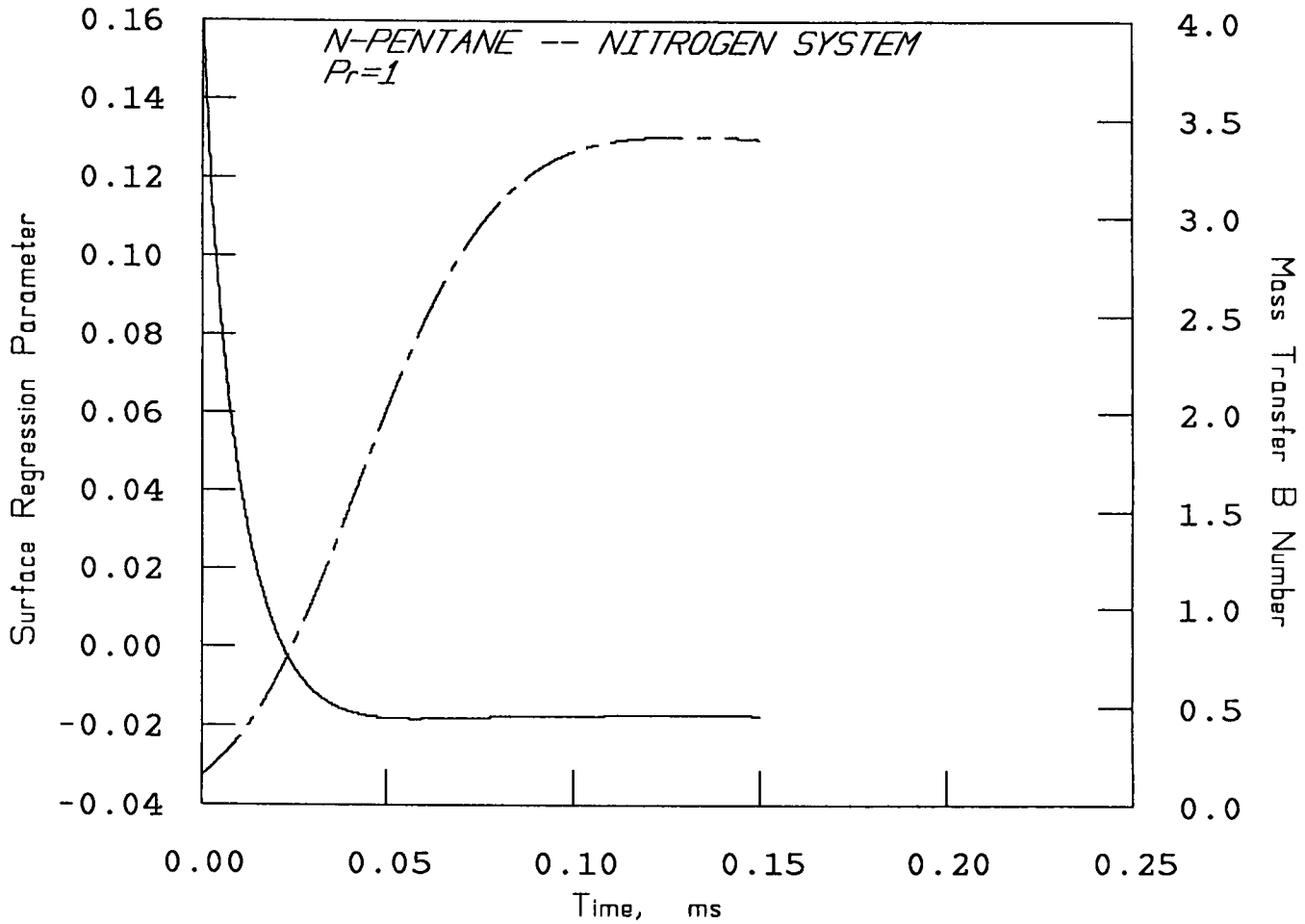

Figure 28. Calculated surface regression parameter and mass transfer B number histories at $P_r = 1$ for n-pentane drop in N_2.

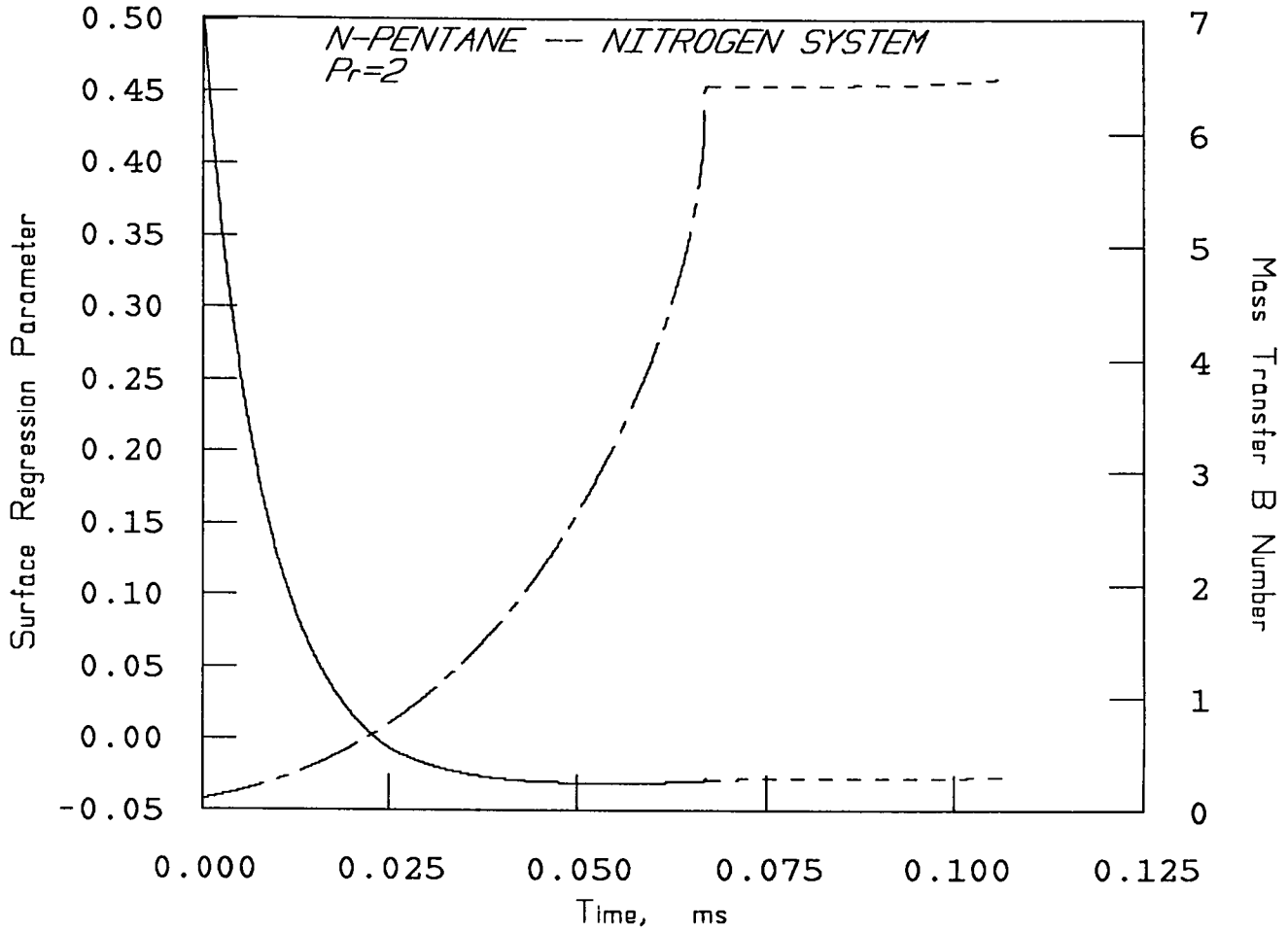

Figure 29. Calculated surface regression parameter and mass transfer B number histories at $P_r = 2$ for n-pentane drop in N_2.

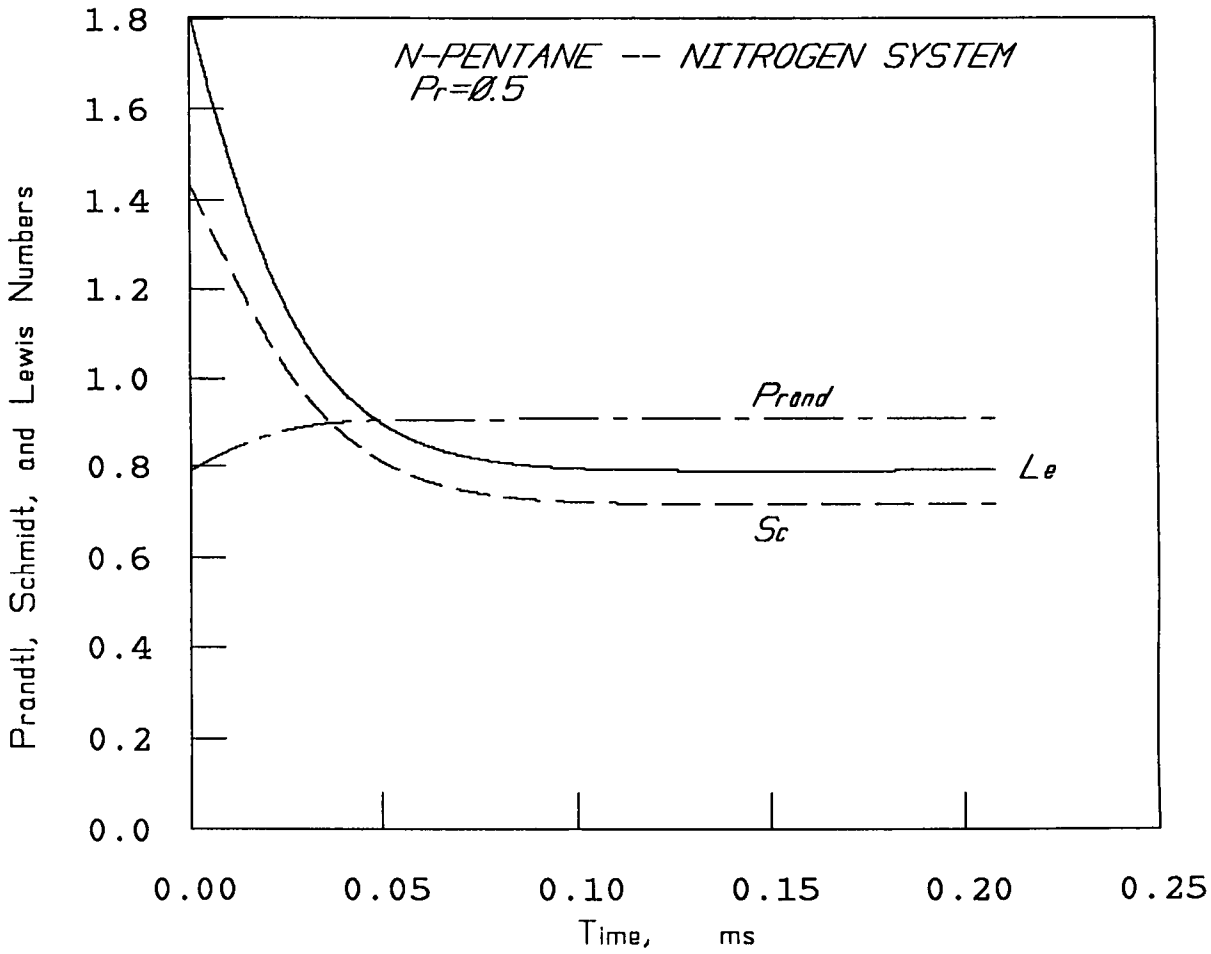

Figure 30. Calculated Prandtl number, Schmidt number, and Lewis number histories for $P_r = 0.5$ for n-pentane drop in N_2.

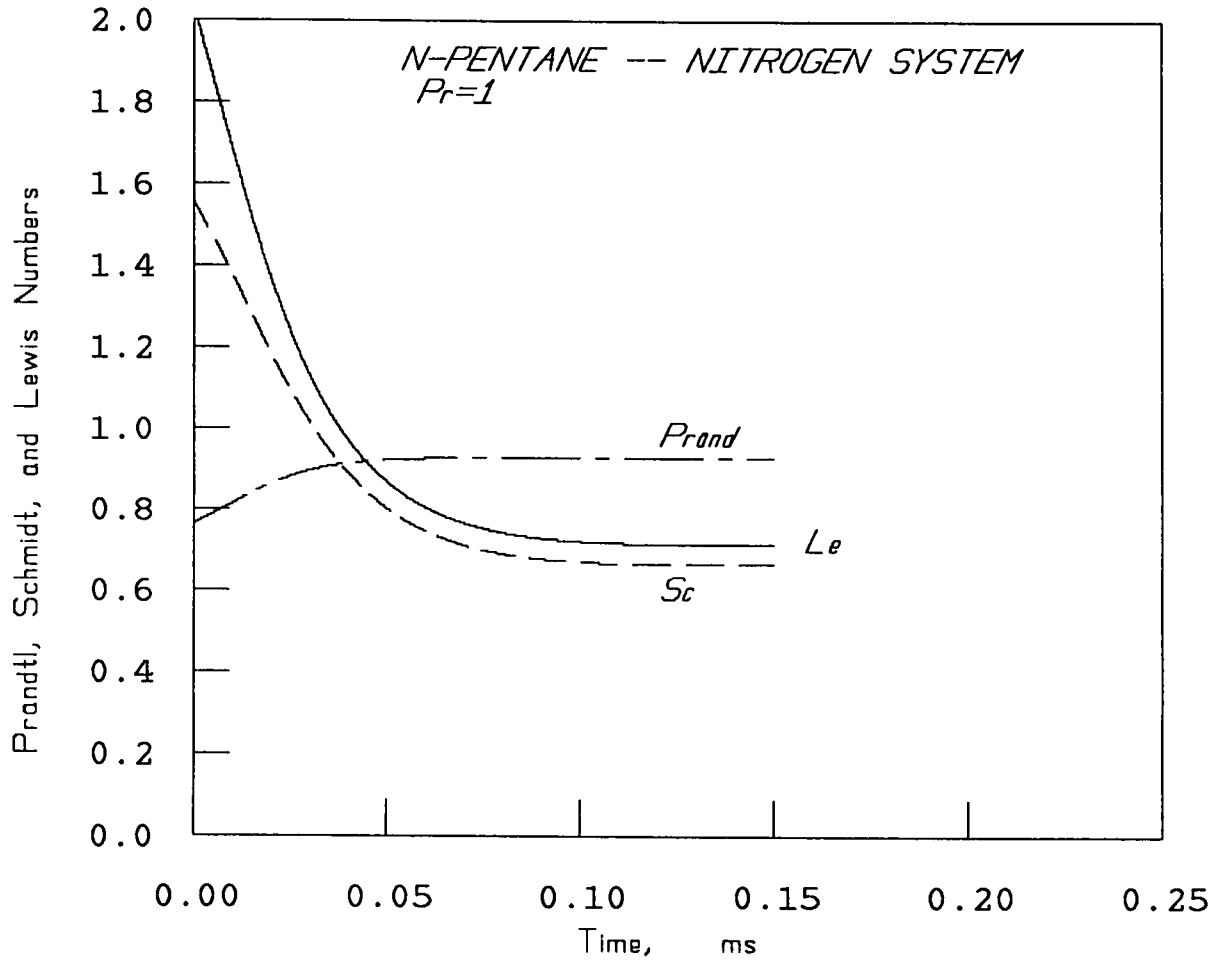

Figure 31. Calculated Prandtl number, Schmidt number, and Lewis number histories for $P_r = 1$ for n-pentane drop in N_2.

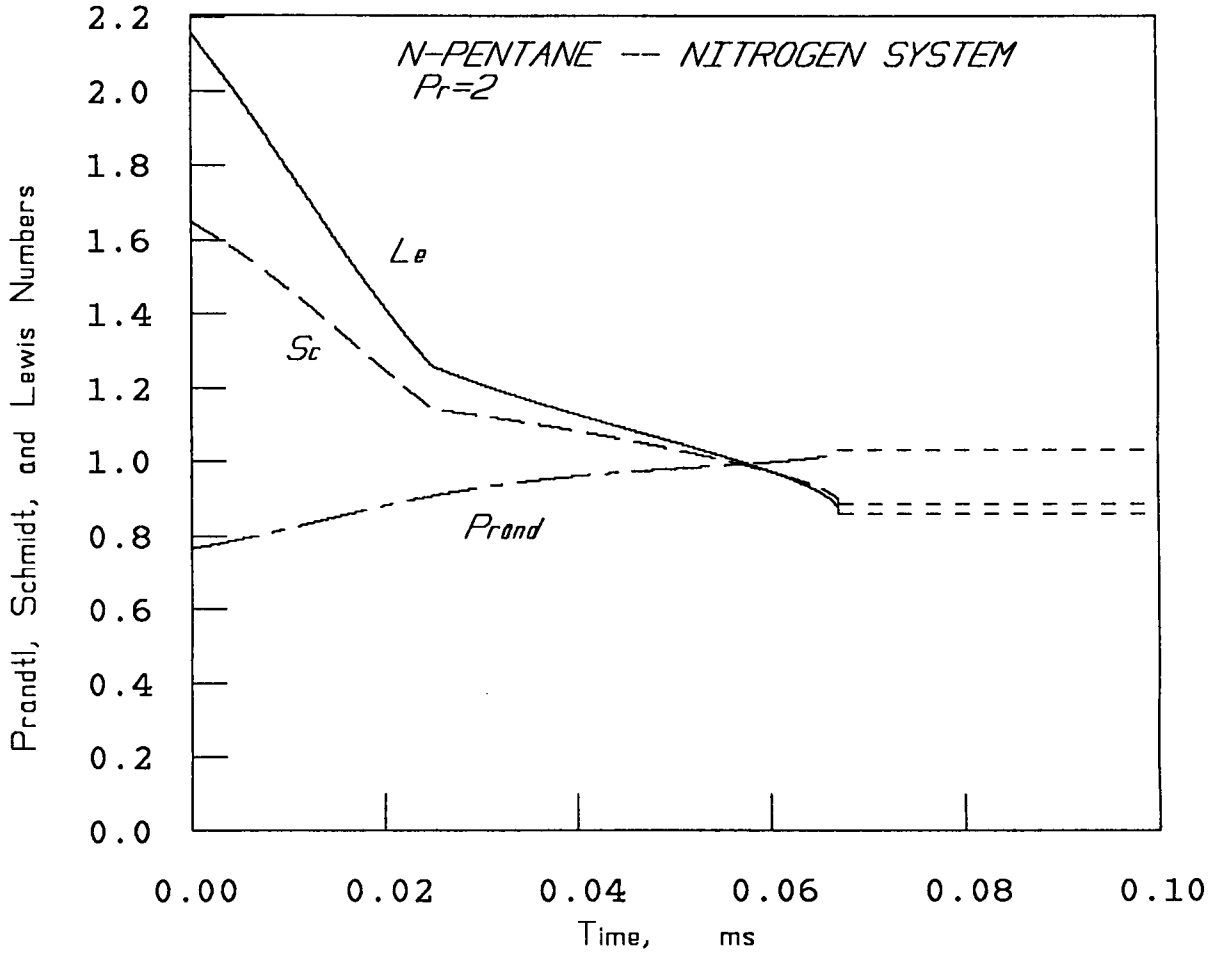

Figure 32. Calculated Prandtl number, Schmidt number, and Lewis number histories for $P_r = 2$ for n-pentane drop in N_2.

CHAPTER 5

APPLICATION TO LOX/HYDROGEN LIQUID ROCKET COMBUSTOR MODELING

5.1 ISOBARIC LOX GASIFICATION IN LOX/H_2 HIGH-PRESSURE, CYLINDRICAL COMBUSTOR

5.1.1 LOX/H_2 High-Pressure Vapor-Liquid Equilibria

In section 3.2.3, the quantum-gas mixing rules for use in the high-pressure vapor-liquid equilibria model of Chueh and Prausnitz (1967) were presented. Inclusion of these mixing rules into the FORTRAN codes described in Chapter 4 allows for a theoretical prediction of the LOX/H_2 system's equilibria thermodynamics. While no experimental results for the precarious vapor-liquid mixture were found for comparative purposes, the theoretical predictions for less hazardous quantum-gas mixtures do compare well with experiment (Chueh and Prausnitz, 1967). Thus, the theory is assumed to provide credible results for the LOX/H_2 system. Some experimental data is available for solid-vapor equilibria in the O_2/H_2 system for trace concentrations of solid oxygen (Mckinley *et al.*, 1961) which might be used to validate the theory in the gas phase, but this analysis is left to future study.

Since the central aim of this study is to produce a propellant vaporization submodel for use in comprehensive CFD spray combustion codes, it is also of interest to examine the predictions of an equilibrium correlation from a current CFD code for LOX/H_2 high-pressure combustor modeling. In this case, the correlation for the LOX gas-phase equilibria mole fraction in hydrogen gas is taken from the ARICC–

LJ code (Liang, 1989) as

$$x_{lox}^{v} \approx \begin{cases} [1.445(10)^{-19}]T_d^{8.36557} & ;T_d < 154.6\ K \\ 0.54493 & ;T_d \geq 154.6\ K \end{cases} \tag{5.1}$$

In addition, the ARICC–LJ code assumes the enthalpy of vaporization for the LOX propellant is identically the latent heat of vaporization.

With inclusion of the quantum-gas mixing rules in the general code, calculations were made for reduced pressures of $P_r = 1$, $P_r = 2$, $P_r = 3$, and $P_r = 4$. The results for LOX equilibria concentration and enthalpy of vaporization are given in Figures 33 and 34, respectively. For comparison, the ARICC correlation for LOX equilibria concentration is shown by the dashed line in Figure 33 and the estimated latent heat of vaporization is shown by the solid line in Figure 34. Again in Figure 33, the expected decrease in the critical mixing temperature with increasing pressure is evident as well as a substantial departure of the ARICC correlation from theory. Most importantly, perhaps, is implication by the ARICC correlation that the critical state occurs at the pure component critical temperature for all pressures. This is certainly erroneous given the established general behavior of the critical mixing temperature with pressure. The enthalpy of vaporization is also seen to depart greatly from the pure component latent heat of vaporization with increasing pressure in Figure 34. The vanishing of the enthalpy of vaporization at the critical state and the decrease in the critical mixing temperature with increasing pressure is again clearly demonstrated in this figure. It would seemingly be fair to conclude from these graphs that the current thermodynamic model in the ARICC–LJ code does not display realistic thermodynamic behavior. If vapor-liquid equilibria is accurate under these conditions, a high-pressure multi-component thermodynamic model is needed. The model used in this study has been validated with experimental data in the literature and is felt to reliable for such computations.

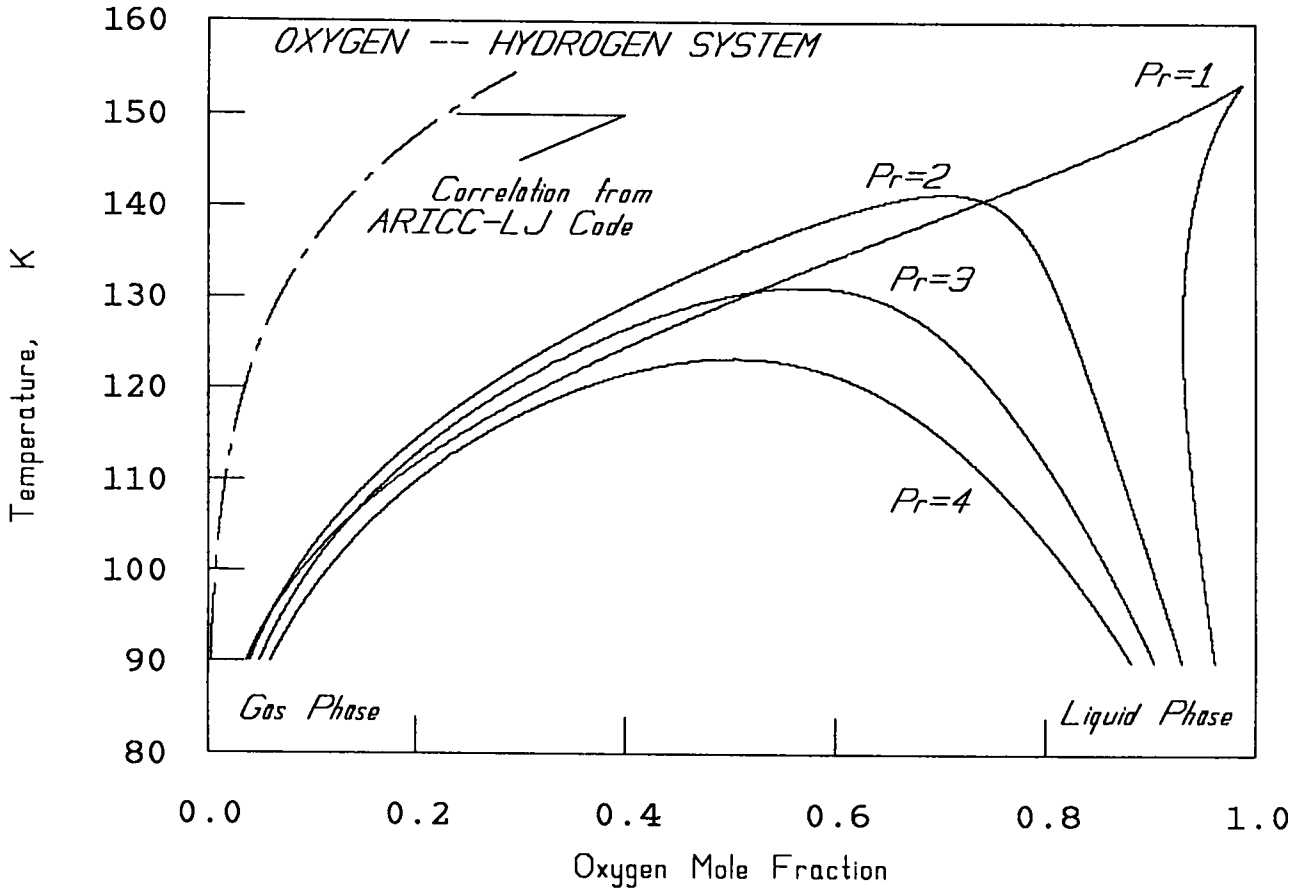

Figure 33. Comparison of theoretical equilibria from general model including ambient gas absorption with current correlation in ARICC-LJ code for oxygen—hydrogen binary system.

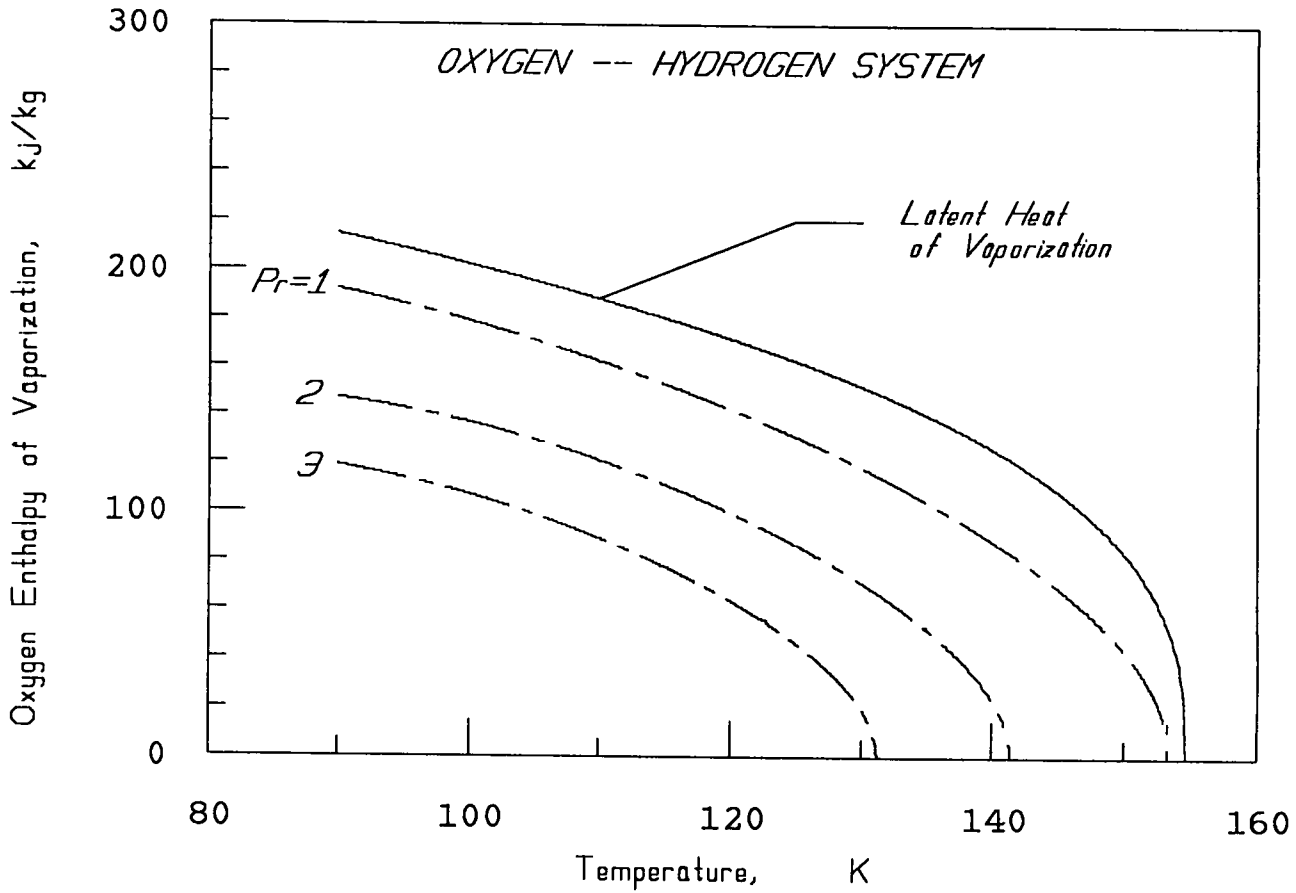

Figure 34. Comparison of theoretical enthalpy of vaporization from general model including ambient gas absorption at supercritical pressures with the latent heat of vaporization for the oxygen—hydrogen binary system.

5.1.2 Simulation of Isobaric LOX Droplet Gasification in a LOX/H_2 High-Pressure, Cylindrical Combustor

The simulation code for droplet gasification described in Chapter 4 is easily adapted to the LOX/H_2 system through incorporation of the quantum-gas vapor-liquid equilibria model and appropriate modifications in thermophysical property evaluations. With this basic code, the behavior of LOX droplets injected into hot hydrogen-rich gases can be investigated. While the submodel could be studied using a comprehensive CFD code for the whole combustor, it is advantageous and instructive to consider axially injected LOX droplets in a simplified one-dimensional flow within a cylindrical combustor.

The temperature and pressure within the vaporization region of this simplified combustor are considered to be constant. The LOX droplets are assumed to be injected as discrete, identically sized particles at the injector face and to travel with an axial component of velocity only. Following the approach of previous investigators, the axial gas velocity in the combustor is assumed to increase in direct proportion to the amount of mass evaporated from the droplets giving

$$U_{axial} = U_F\left(1 - \frac{m_p}{m_{p_0}}\right) + U_{inj} \tag{5.2}$$

where U_F is the final axial gas velocity. The stripping mode of vaporization is also included but is only enforced when the droplet has attained the critical state and the Rabin number is greater than unity. Evaluation of a break-up induction time is neglected for simplicity. When stripping vaporization is invoked, Liang's criteria for mass transfer, which is given in equation (3.64), is utilized. In addition, the rate of change of droplet temperature is forced to zero when the droplet reaches criticality so that computation may continue.

The simulation code was easily modified to meet the desired criteria, and a

sample calculation was made with conditions representative af a realistic thrust chamber. In the calculation, 100 μm LOX droplets are assumed to be injected at 30 m/s relative to the injected gaseous hydrogen. The temperature and pressure in the vaporization region are assumed to be 1000 K and 200 atm ($P_r = 4$), respectively. The final gas velocity was arbitrarily taken as 250 m/s.

This calculation was repeated using the ARICC–LJ thermodynamic model to illustrate the role of thermodynamics in the gasification process. A comparison of the principal results are given in Figures 35–36. Results using the high-pressure vapor-liquid equilibria model are given by solid curves, and results for the ARICC–LJ equilibria model are denoted by dashed curves.

The instantaneous to initial diameter ratio squared is given in Figure 35. Both models indicate that the droplet will expand early in its lifetime and undergo rapid gasification due to stripping atomization once the relative velocity vector is reversed. Because the ARICC model allows the drop to reach the pure component critical temperature, it experiences more thermal expansion. After the droplets reach criticality they experience some stripping-mode vaporization until they enter the zone of relative velocity reversal. In this region, there is reduced forced convection as the droplet decelerates to the gas-phase velocity and then accelerates as the freestream velocity continues to increase; thus, stripping-mode vaporization is here inactive and finite-rate diffusion controlled vaporization must be considered. As the droplet leaves the reduced convection region, stripping vaporization is again invoked, and the droplets experience rapid gasification. The end result is that the ARICC–LJ model predicts a droplet lifetime roughly twice that of the general thermodynamic model.

The time dependent droplet temperature profiles for both thermodynamic models are shown in Figure 36. For the ARICC model, the droplet is shown to attain

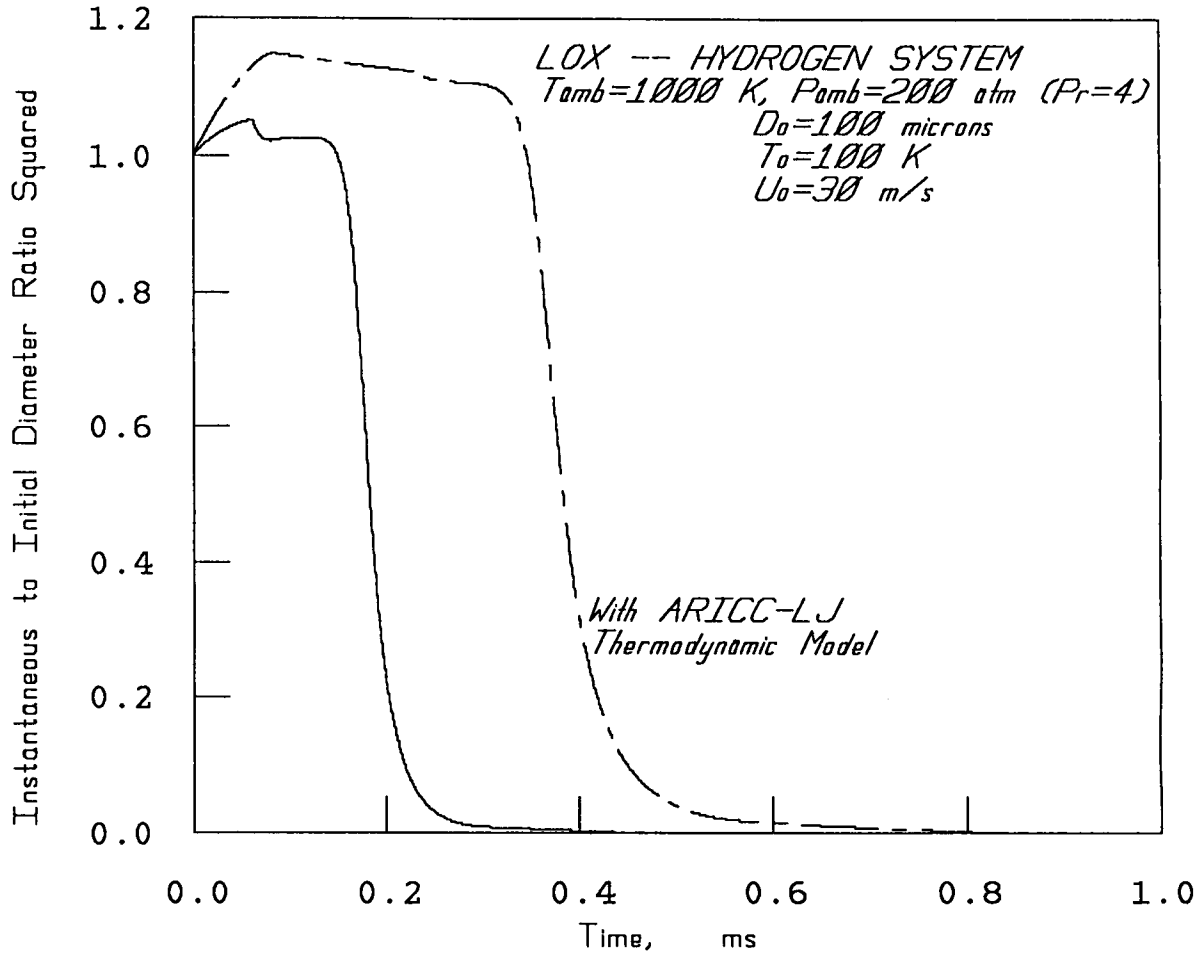

Figure 35. Calculated $d_d^2/d_{d_0}^2$ ratio histories for LOX/H_2 liquid rocket combustor.

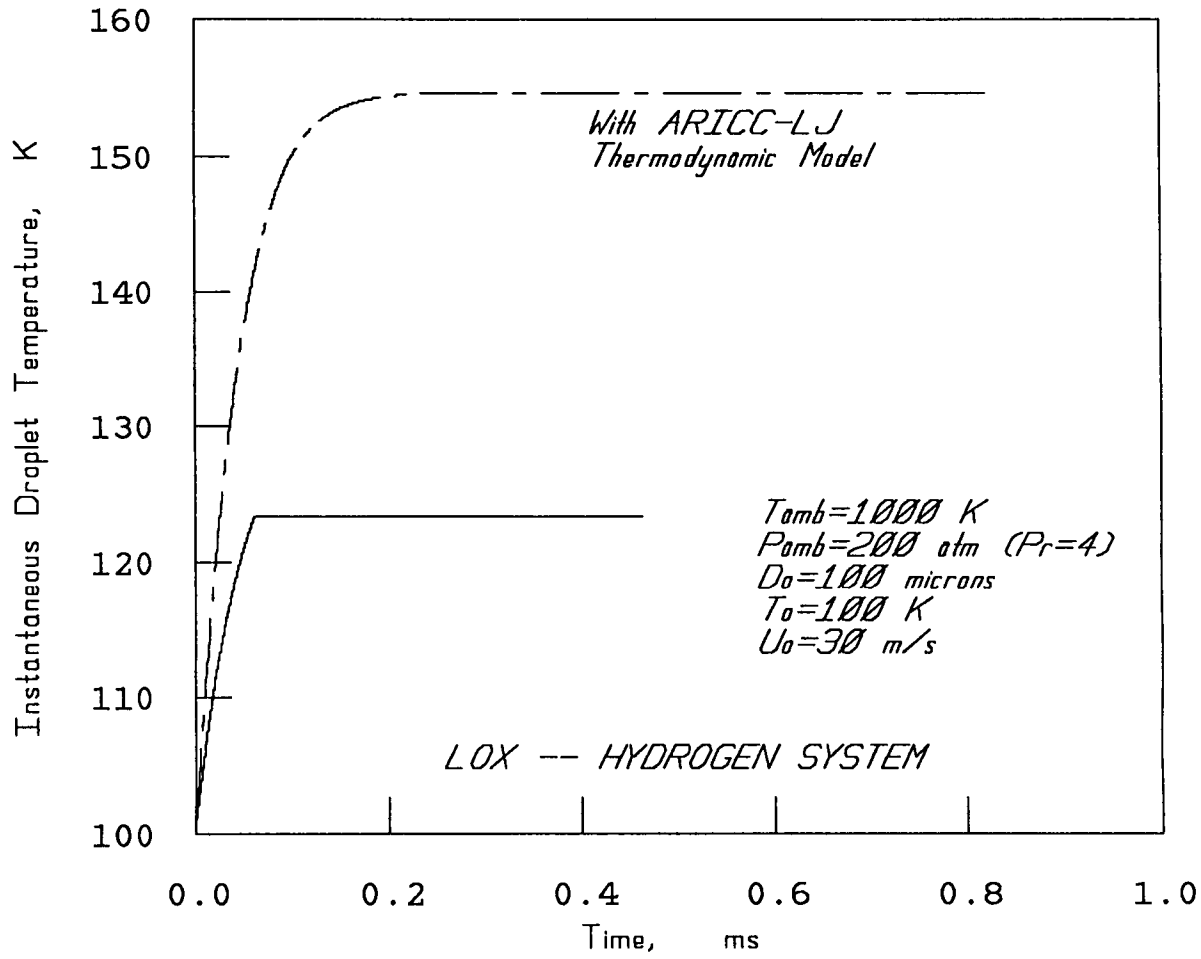

Figure 36. Calculated droplet temperature histories for LOX/H_2 liquid rocket combustor.

the pure component critical temperature whereas for the general model the droplet reaches criticality at roughly 124 K for a chamber pressure of 200 atm. Heat-up times are very short for both models.

In Figure 37, the instantaneous to initial drop mass ratios are presented providing a comparison of gasification rates. The rate for the general model exceeds the rate using the ARICC model during the heat-up period primarily because of the reduced enthalpy of vaporization relative to the latent heat of vaporization. Because the droplet attains criticality sooner for the general model, it can undergo stripping vaporization earlier and therefore vaporize more quickly. The step shapes in the curves are attributed to the relative velocity reversal region.

The axial droplet velocity relative to the freestream velocity is given in Figure 38, and the axial distance traveled with time is shown in Figure 39. The relative velocity curves show the same trends for both models. The injected droplet initially decelerates until the droplet velocity is identically equal to the freestream velocity whereupon the direction of the relative velocity reverses and the droplet begins acelerating until it reaches dynamic equilibrium with the final gas-phase velocity in the chamber. From Figure 39, one sees that the droplet travels farther downstream for the ARICC model because of its longer lifetime. The sharp rise in the rate of distance traveled by the droplets is due to the rapid gasification of stripping vaporization. Obviously, the general thermodynamic model predicts a rapidly developing spray process.

In summarizing, the high-pressure thermodynamic model predicts a faster rate of development of the gasification process. The basic overall trends are similar as the fluid dynamics which the droplets experience in both cases are similar, but use of a realistic thermodynamic model indicates that the atomization and vaporization processes are compacted much closer to the injector face.

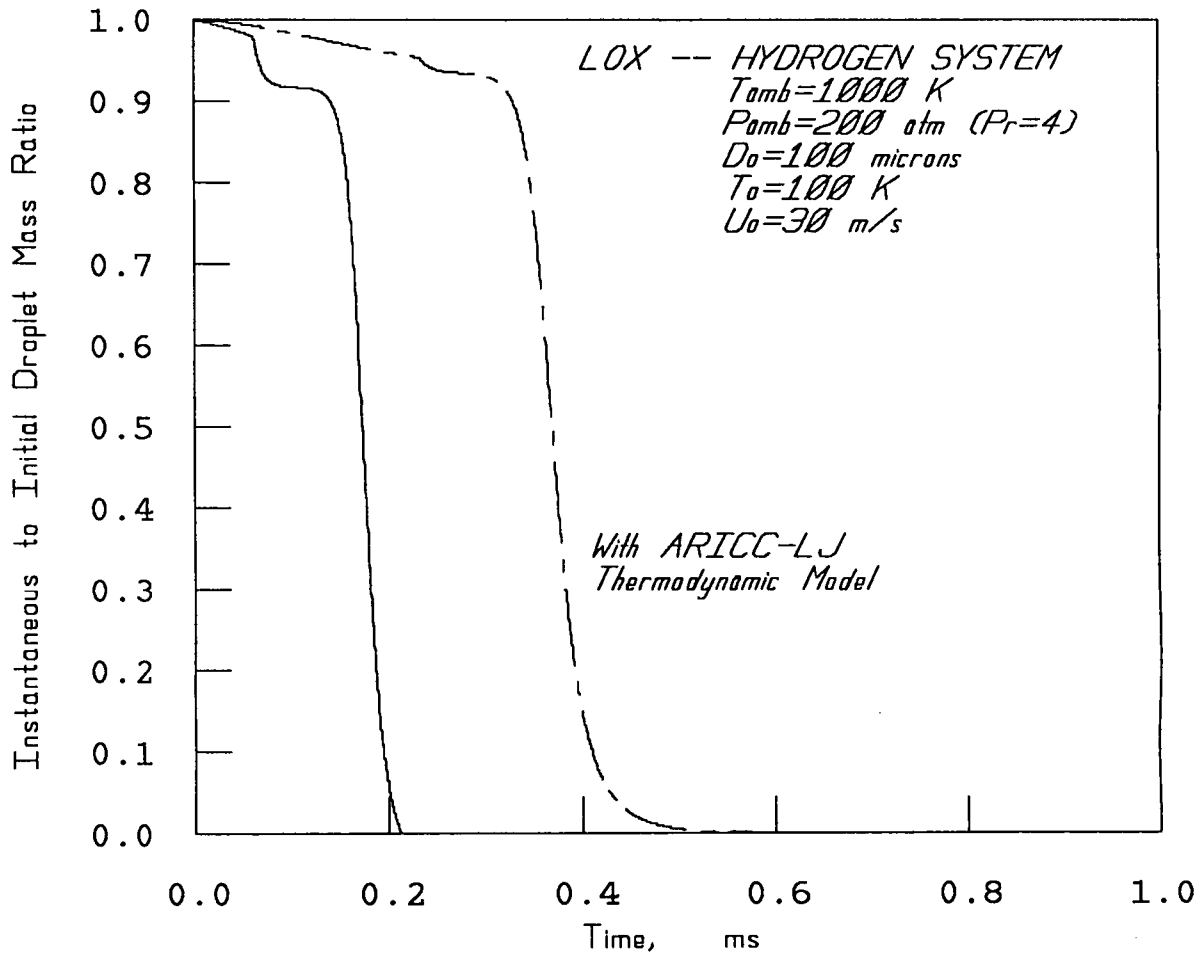

Figure 37. Calculated m_d/m_{d_0} ratio histories for LOX/H_2 liquid rocket combustor.

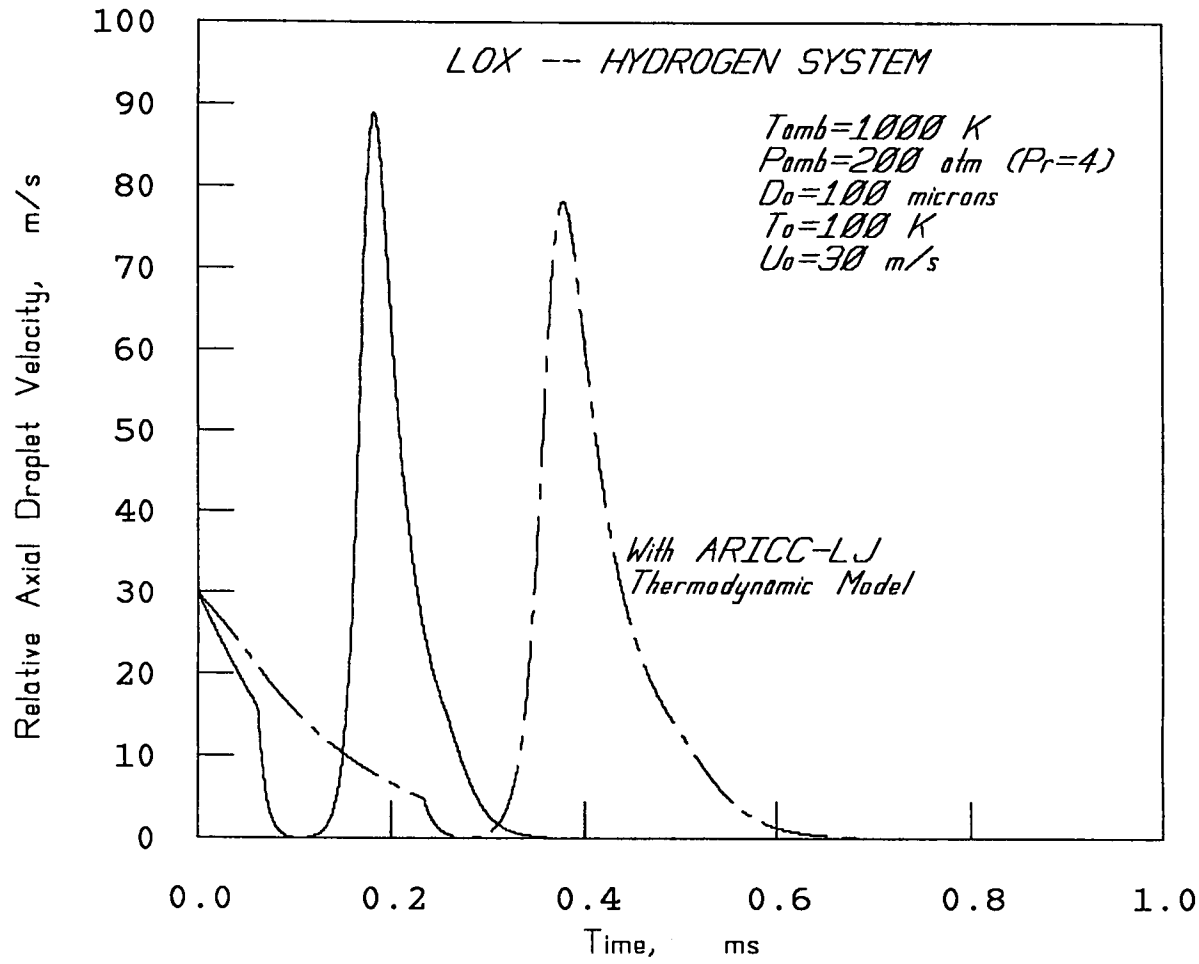

Figure 38. Calculated relative axial droplet velocity in LOX/H_2 liquid rocket combustor.

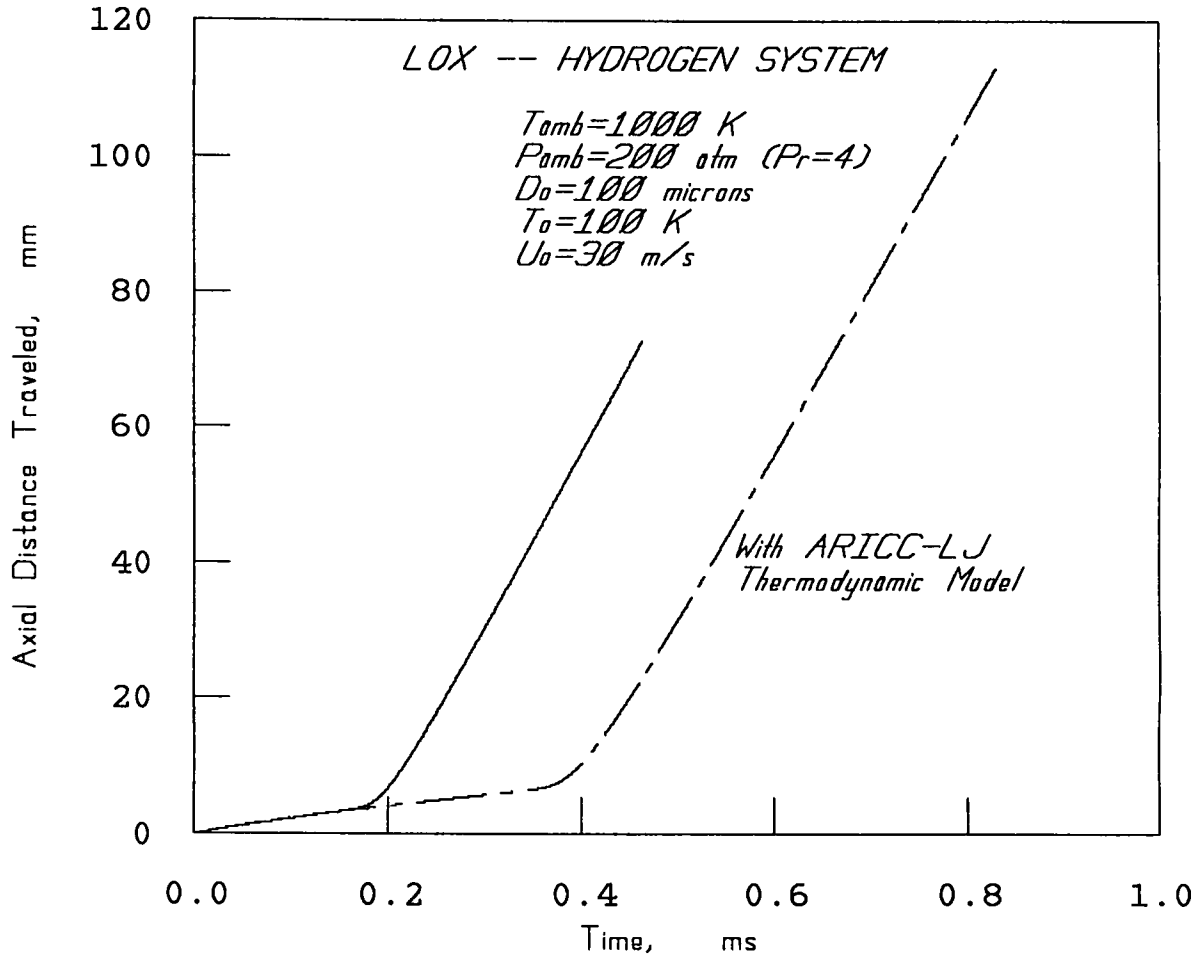

Figure 39. Calculated axial distance traveled by LOX droplet in LOX/H_2 liquid rocket combustor.

5.2 LOX GASIFICATION IN ACOUSTICALLY OSCILLATING FIELD INSIDE A LOX/H_2 HIGH-PRESSURE, CYLINDRICAL COMBUSTOR

5.2.1 High-Frequency Transverse-Mode Acoustic Oscillation Theory For a Cylindrical Combustor

Although shock wave models have been proposed to describe nonlinear unstable rocket combustion, emphasis has remained upon Rayleigh-type mechanisms of acoustic wave reinforcement within the rocket chamber. The mathematical models developed for Rayleigh-type instability are varied depending on the rate controlling mechanism for the combustion process, but they generally share a common approach. This commonality lies in the neglect of instability initiation and the attempt to determine system stability limits by superimposing a proposed acoustic mode at a specified frequency on the steady flow within the combustor. If the oscillations are damped, the combustor is said to be dynamically stable, but if the system is driven to resonance, the combustor is said to be susceptible to the imposed mode of instability.

Therefore an acoustic mode of oscillation is proposed before stability limits are determined. For high-frequency screeching instability, experiental evidence indicates that acoustical resonance is in the form of combined radial and tangential modes in the transverse plane (Harrje and Reardon, 1972), and this has led to the use of transverse-mode resonant acoustics in high-frequency stability analyses.

As it is of interest to examine high-pressure LOX droplet gasification in the presence of an oscillating acoustic field characteristic of high-frequency liquid rocket combustion instability, a prevalently used traveling-transverse resonant acoustic mode will be superimposed upon the one-dimensional combustor model previously

described. The pressure and velocity acoustic oscillations for a cylindrical combustor are adapted from Heidmann and Wieber (1966) as

$$P = P_{mean}\left[1 + 1.718\frac{P_{amp}}{P_{mean}}\, J_1\left(\frac{1.841r}{R_{wall}}\right)\sin(2\pi ft - \theta)\right] \tag{5.3}$$

$$V_r = 0.860\frac{a}{\gamma}\frac{P_{amp}}{P_{mean}}\left[J_0\left(\frac{1.841r}{R_{wall}}\right) - J_2\left(\frac{1.841r}{R_{wall}}\right)\right]\cos(2\pi ft - \theta) \tag{5.4}$$

$$V_\theta = 0.934\frac{a}{\gamma}\frac{R_{wall}}{r}\frac{P_{amp}}{P_{mean}}\, J_1\left(\frac{1.841r}{R_{wall}}\right)\sin(2\pi ft - \theta) \tag{5.5}$$

where a is the gas-phase speed of sound, γ is the gas-phase specific heat ratio, R_{wall} is the radius of the cylindrical combustor, and r is any specified radius. In addition, the acoustic wave is assumed to be adiabatic such that

$$\rho = \rho_{mean}\left(\frac{P}{P_{mean}}\right)^{\frac{1}{\gamma}} \tag{5.6}$$

$$T = T_{mean}\left(\frac{P}{P_{mean}}\right)^{\frac{\gamma-1}{\gamma}} \tag{5.7}$$

These acoustic oscillation equations were incorporated into the LOX/H_2 combustor code, and the differential equations (3.57) and (3.56) were included to account for the three dimensional motion of the droplet. To verify initially the qualitative correct acoustical behavior, a sample calculation was made for the superimposed oscillations in hydrogen gas while injecting LOX droplets. For this test case, the mean pressure and mean temperature in the vaporization region were taken to be $P_{mean} = 150$ atm and $T_{mean} = 1000$ K. The peak pressure perturbation amplitude was assumed to be 10% of the mean chamber pressure ($P_{amp}/P_{mean} = 0.1$), the radial injection location in the combustor was fixed such that $r/R_{wall} = 0.912$

where the maximum pressure amplitude occurs, and the resonant frequency was specified as $F = 2000$ Hz. Also, at time $t = 0$ the acoustic phase angle was set at $\theta = 0$.

Results for this calculation are shown in Figure 40 for one cycle of oscillation. Note that the pressure and tangential velocity fluctuations are in phase with each other but 90° out of phase with the radial velocity component as expected from the sinusoidal terms in the acoustic equations. The pressure amplitude is indeed 10% of the mean chamber pressure, and tangential velocity fluctuations are much larger than the radial velocity fluctuations at the specified radius for this particular acoustic mode. The intuitively sensible results of the calculation allow one to proceed with some confidence.

5.2.2 Simulation of LOX Gasification in Unstable LOX/H_2 High-Pressure, Cylindrical Combustor

Before executing a simulation of LOX droplet gasification in an acoustically oscillating field, some preliminary understanding may be aquired from expected qualitative behavior and from the parametric study of n-pentane vaporization in nitrogen gas from Chapter 4. From this parametric study, it was found that the rate of droplet gasification increased with increasing pressure causing the entire process to occur on much shorter time scales. Also, the ability to heat to the critical state for ambient pressures sufficiently higher than the vaporizing substance's critical pressure, and the fact that the critical mixing temperature decreases with increasing pressure, was demonstrated. Furthermore, the effect of velocity on the gasification process is easily isolated as a convective enhancement for heat and mass transfer. For higher relative velocity, the greater convection increases transport rates while for lower relative velocity the reverse is true. These conclusions, note, are general.

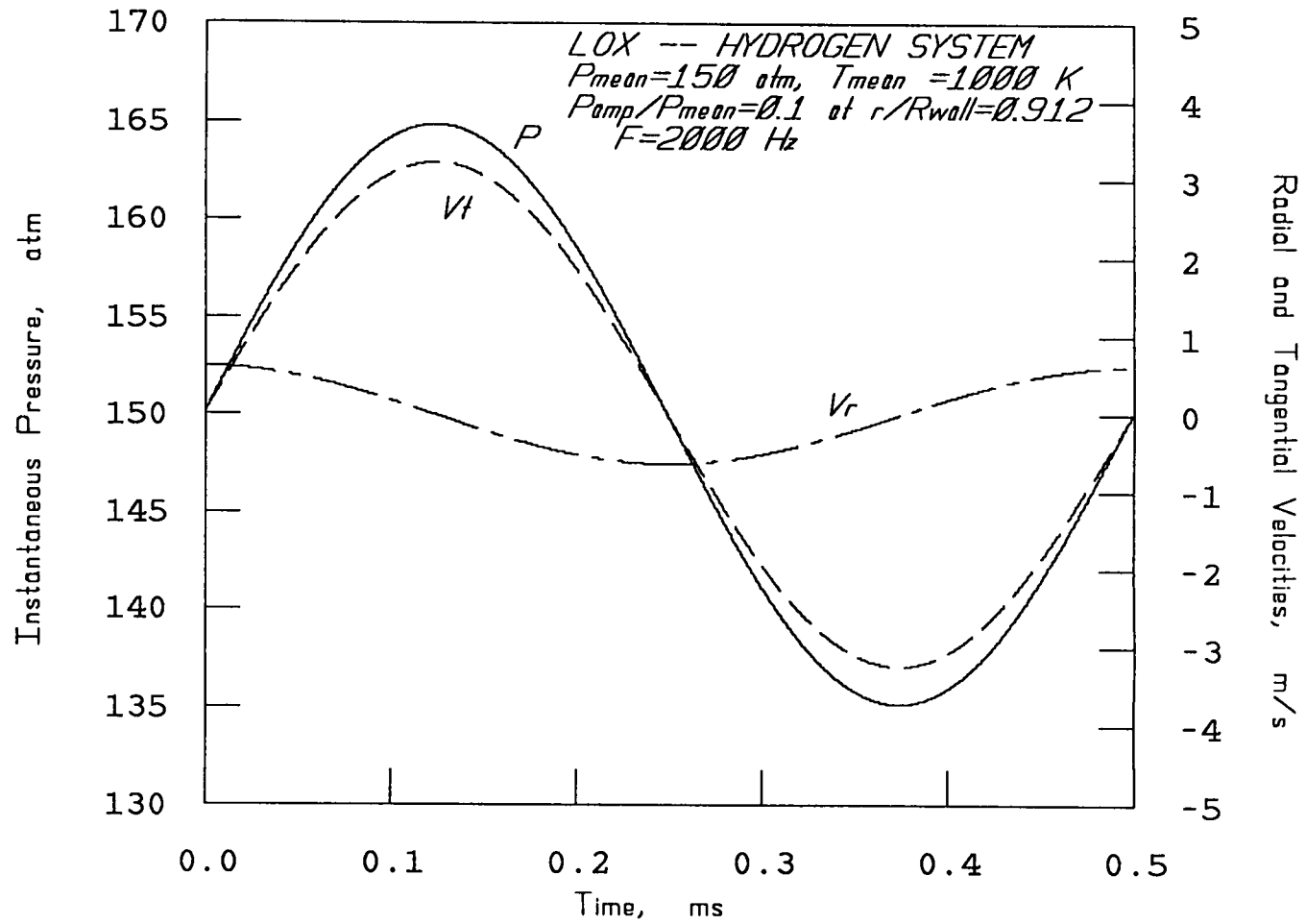

Figure 40. Pressure and velocity oscillations of a traveling-transverse resonant acoustic mode in a cylindrical LOX/H_2 combustion chamber.

Because the propellant gasification response to changing ambient pressure and freestream velocity is qualitatively general, it is possible to discern droplet gasification characteristics under the influence of sinusoidally oscillating pressure and velocity fields. For example, one would expect the vaporization rate to show a rectified response to velocity fluctuations if the magnitude of the perturbations were indeed strong enough to have a major influence on the convective transfer rates. However, since the velocity oscillations of Figure 40 are of relatively small magnitude, gasification frequency response is probably insignificant for the considered acoustic mode although the increased convection will certainly shorten the process in comparison to the stable case. On the other hand, a fluctuating pressure field will surely have a marked effect upon gasification behavior because the amplitude of the perturbations are relatively large and because the gasification process is demonstrably sensitive to the ambient pressure.

Depending upon when the droplet is injected into the chamber during the acoustic cycle, the instantaneous pressure may be rising or falling. If the pressure is rising, the vaporization rate can be expected to increase in response, and if the pressure is falling, the vaporization rate can be expected to decrease in response. Thus, the droplet history will depend intimately on the injection phase angle in relation to the acoustic cycle. This is especially true for LOX propellant since the lifetime for gasification can be much less than the period of oscillation, even at high acoustic frequencies. Oddities also arise when the droplet reaches the critical state at some instantaneous pressure which then changes in the ensuing instant of time.

To demonstrate these effects, calculations were made with the one-dimensional LOX/H_2 combustor code including superimposed acoustic oscillations. The mean chamber pressure was set at $P_{mean} = 150$ atm and the mean temperature in the

vaporization region was taken to be T_{mean} = 1000 K. The maximum pressure perturbation was kept at 10% of the mean chamber pressure at $r/R_{wall} = 0.912$, and the resonant frequency was specified as $F = 2000$ Hz. The LOX droplets were injected at $U_{x_d} = 30m/s$ with an initial temperature of $T_{d_0} = 100K$ and an initial diameter of $d_{d_0} = 100\ \mu m$. Different phase injection angles were considered to examine the chracteristic droplet behavior.

Although the gasification frequency response of LOX propellant is of interest as a Rayleigh-mechanism for instability, the qualitative trend of the vaporization rate with pressure is established, and the gasification rate is here disregarded in favor of the more interesting droplet temperature and thermodynamic behavior in an acoustically oscillating field. For example, Figure 41 depicts the temperature history of a LOX droplet, injected at a phase angle of $\theta = 0$, in relation to the accompanying pressure oscillation. This same temperature history is presented on the LOX/H_2 vapor-liquid equilibria diagram in Figure 42. It is immediately obvious from Figure 41 that the heat-up period to criticality is extremely short and occurs in less than a fourth of the oscillation period. This can be attributed to the increased gasification rate with pressure. Further, the calculation is seen to cease as soon as the critical conditions are reached. This particular anomaly infers a thermodynamic phenomenon that may play a considerable role in the initiation or sustenance of spray combustion instability.

The cause for the halt in calculation at the critical state is due to the inability of the vapor-liquid equilibria model to provide a solution as the pressure continues to increase with time. A proposed physical explanation for this anomalous behavior, termed *punctuated criticality* by this author, is best explanied with reference to Figure 42. As time increases, the ambient pressure increases while the acoustic wave proceeds, and the droplet temperature begins to increase as it heats up. This

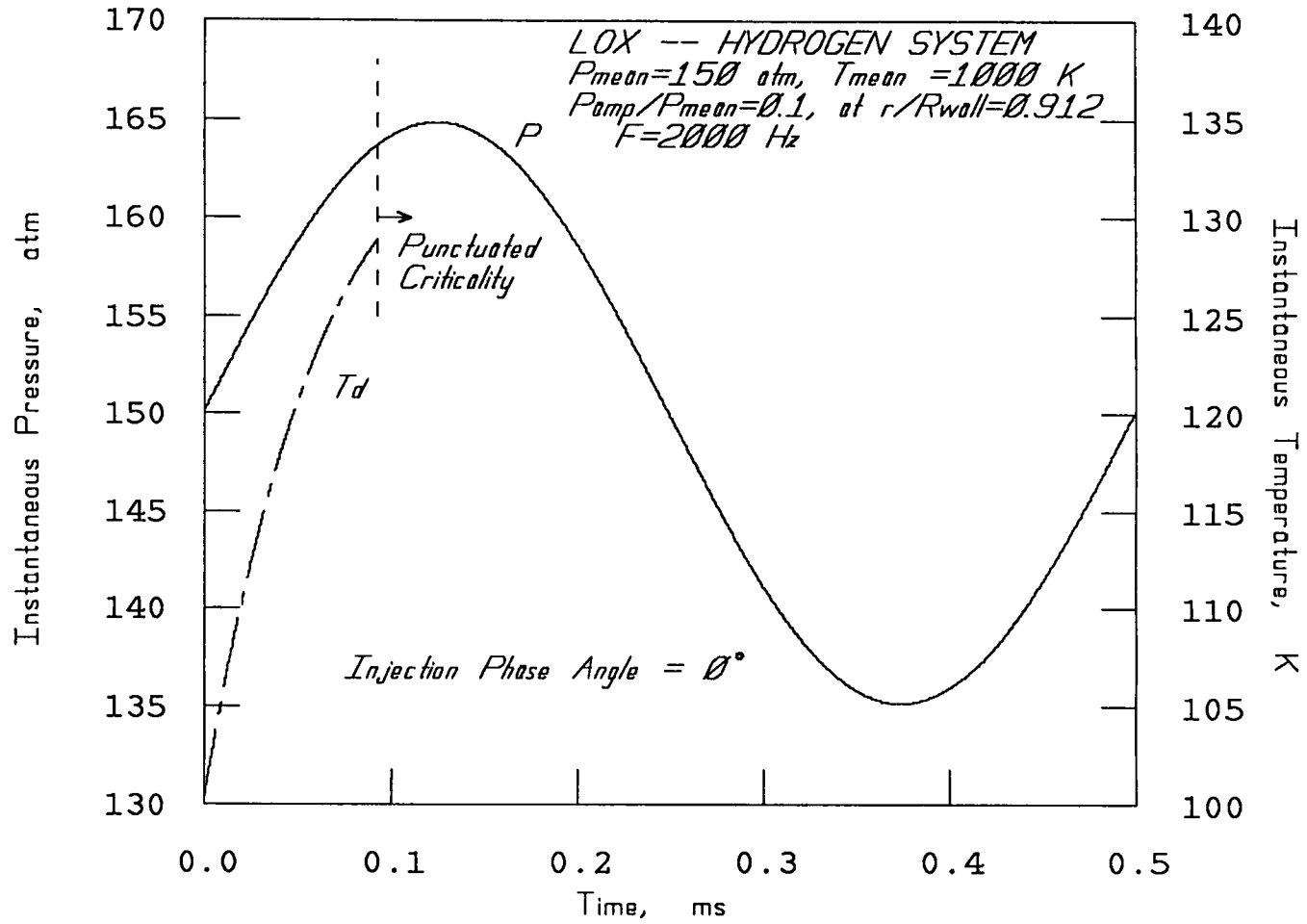

Figure 41. Calculated droplet temperature and acoustic pressure oscillation histories for LOX droplet injection phase angle $\theta = 0$.

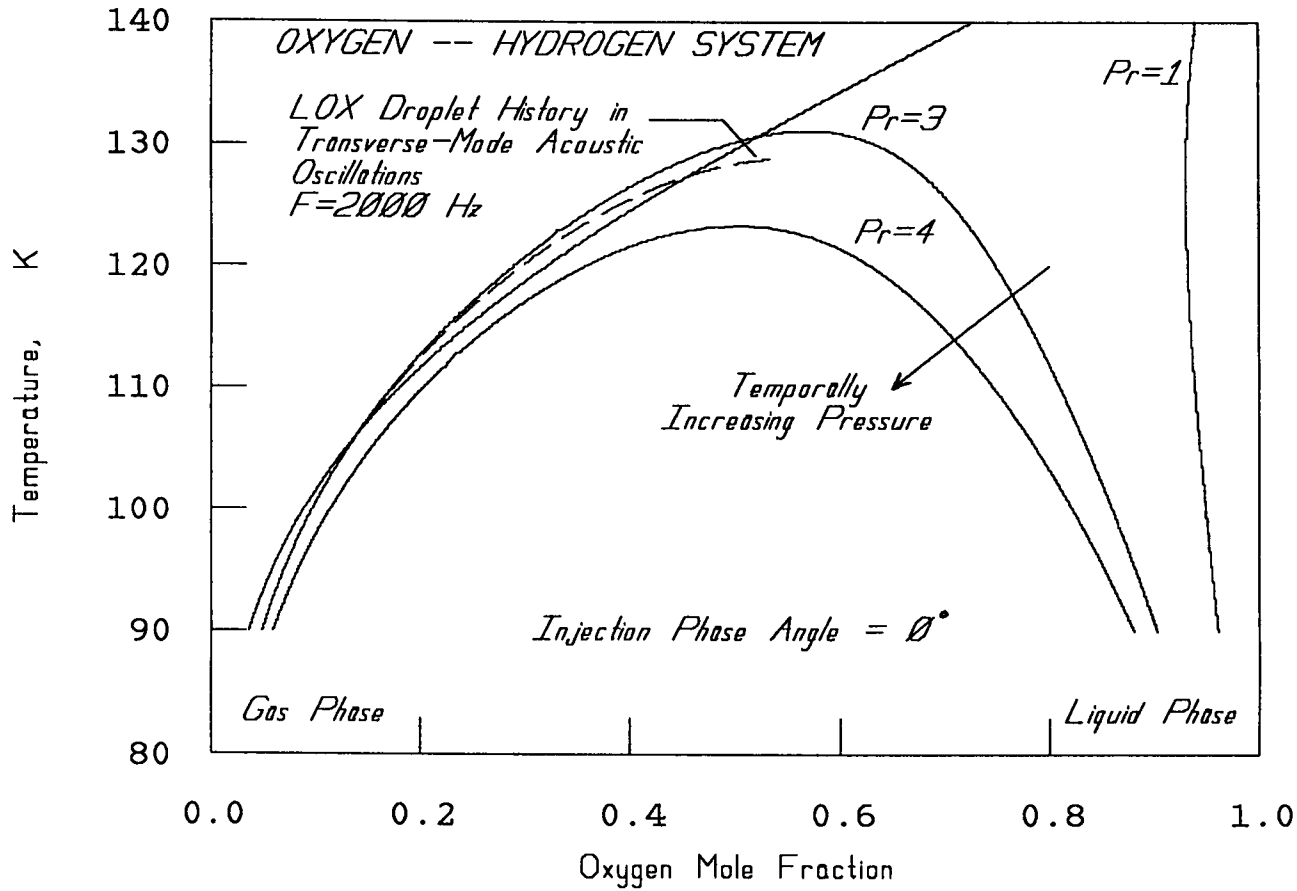

Figure 42. Calculated droplet temperature history on LOX/H_2 vapor-liquid equilibria diagram for LOX droplet injection phase angle $\theta = 0$.

process is represented by the dashed line in Figure 42 which shows the equilibria condition moving along isobars of increasingly higher pressure as the droplet temperature rises. Heat-up continues until a critical state is reached immediately after which the pressure increases again, but the droplet surface temperature is above the critical mixing temperature for this new pressure and an equilibrium solution does not exist. Plainly, the droplet surface moves into the superheated region when the pressure increases beyond criticality and the thin surface mixture must instantaneously vaporize indicating a sudden, vigorous vaporization rate. A schematic of the process is depicted in Figure 43. *It should be emphasized that this explanation is only a proposed physical process as implied by current theory. Verification of this proposition must await experimental observation.*

Certainly, such rapid gasification could possibly initiate instability if a droplet near the critical state suddenly moved into a region of high pressure within the combustor. Also, such a process could couple with the acoustic oscillations and act as a Rayleigh mechanism for driving combustion instability. The concept has been advanced that hot droplets interacting with a pressure rarefaction could support or initiate combustion instability (Wieber, 1963), but the concept of *punctuated criticality* whereby a compression wave interaction with a droplet near the critical state supports or initiates combustion instability appears to be novel. Intuition would support the pressure rarefaction concept but a closer examination of multicomponent thermodynamics at elevated pressures reveals that the compression wave interaction is a more likely instability mechanism.

The path to punctuated criticality as illustrated by Figures 41 and 42 is by no means unique. The process can be altered significantly just by changing the injection phase angle with respect to the acoustic cycle. Such an alternate path is demonstrated in Figures 44 and 45 where the injection phase angle is taken as

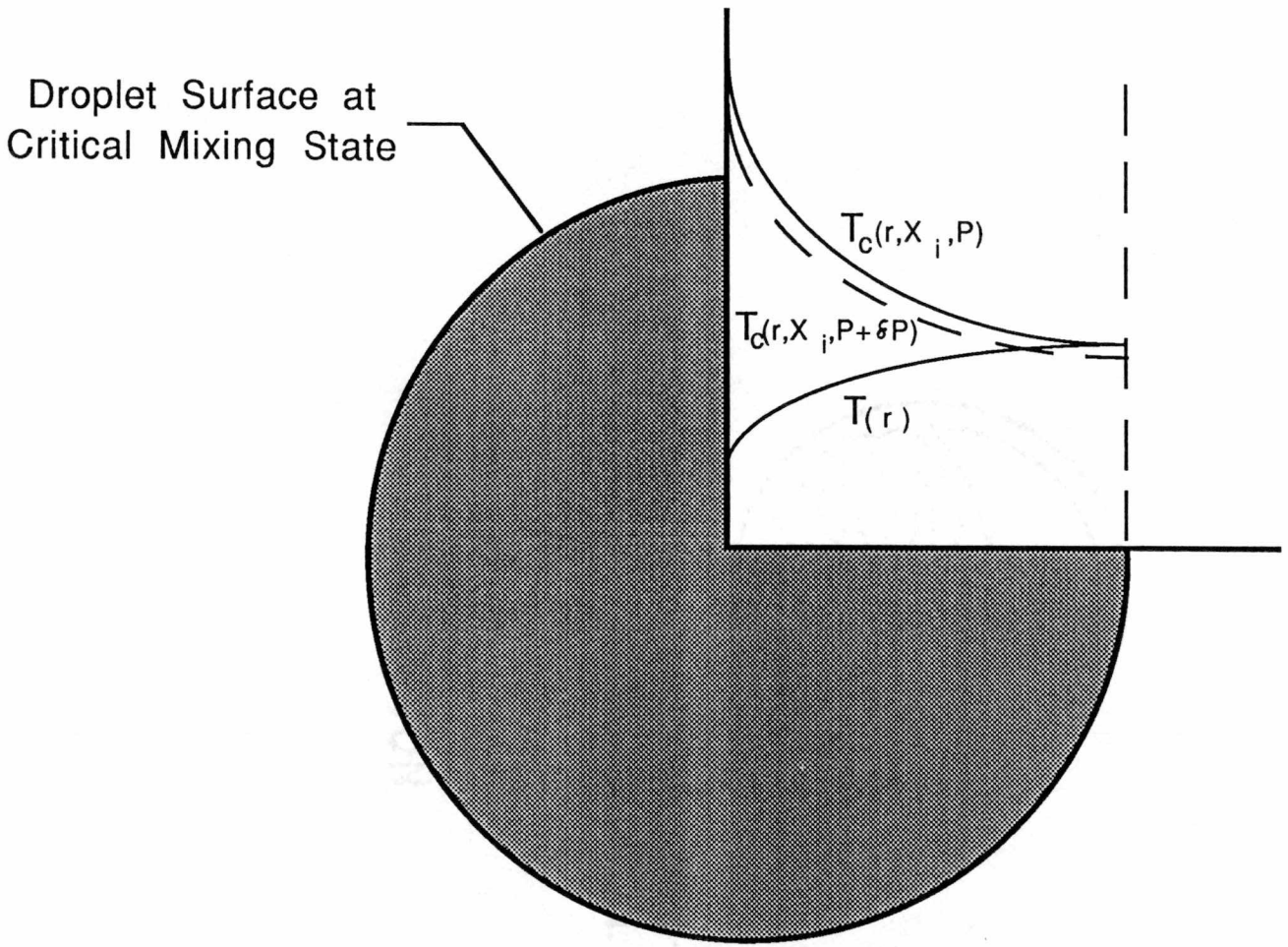

Figure 43. Schematic of *punctuated criticality* process.

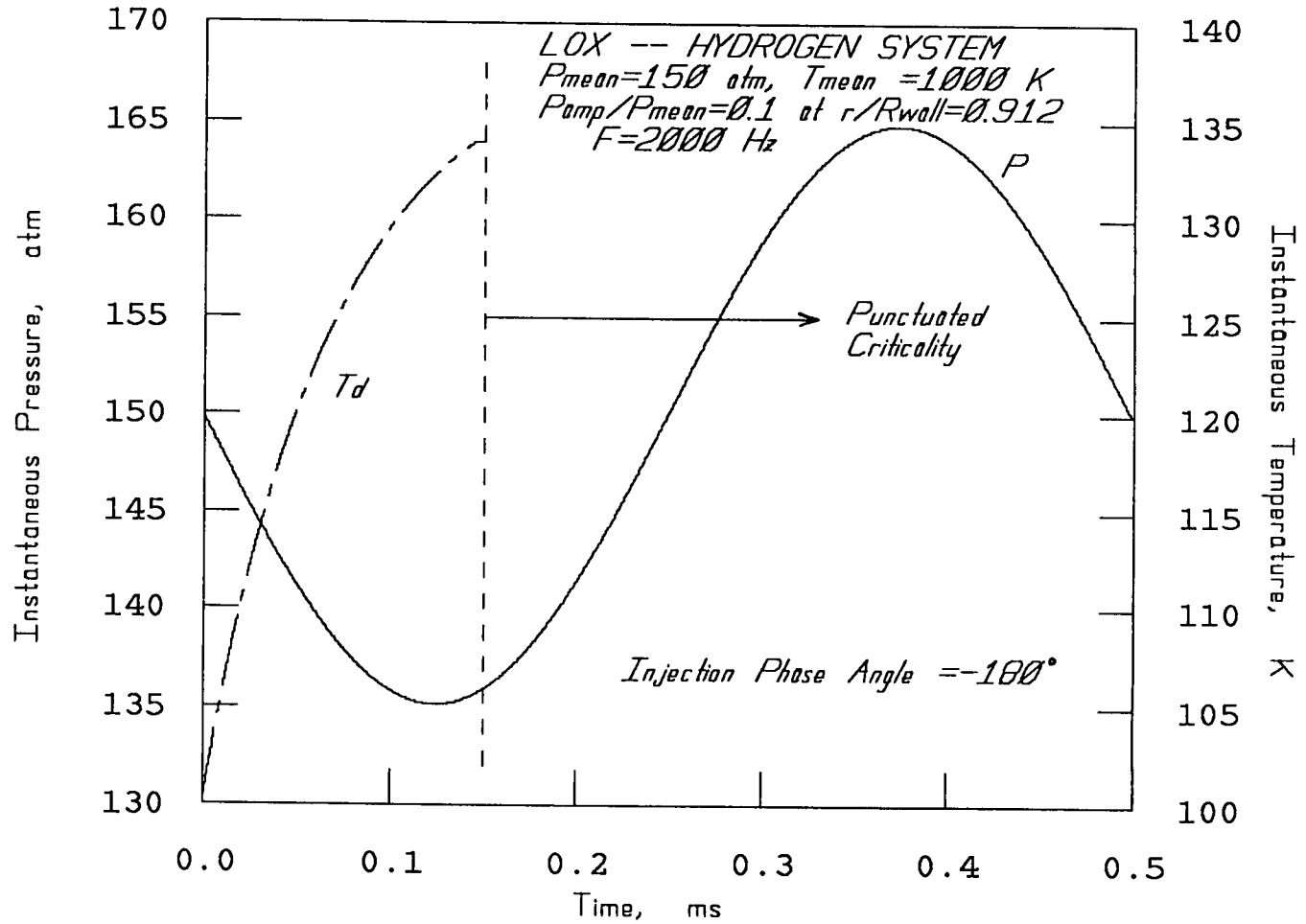

Figure 44. Calculated droplet temperature and acoustic pressure oscillation histories for LOX droplet injection phase angle $\theta = -\pi$.

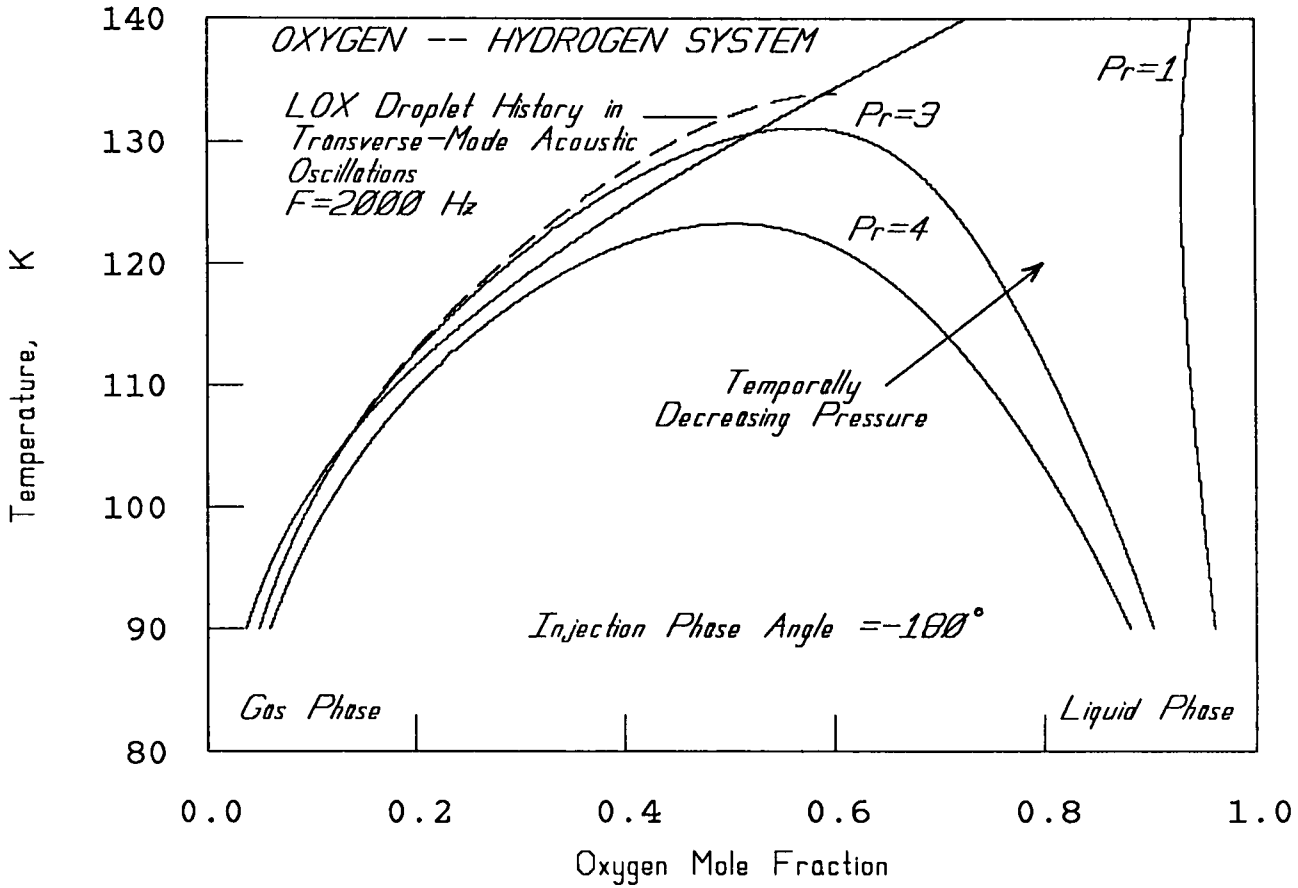

Figure 45. Calculated droplet temperature history on LOX/H_2 vapor-liquid equilibria diagram for LOX droplet injection phase angle $\theta = -\pi$.

$\theta = -\pi$ so that the drop experiences a decreasing pressure field upon injection. In this case, one sees the heat-up period is extended into the ensuing pressure rise portion of the cycle because of reduced gasification rates. The droplet still eventually reaches criticality and experiences the punctuated criticality phenomenon though it does take longer to occur. Therefore, unless the gasification lifetime is much shorter than the period of oscillation, a propellant drop will attain a critical state and experience punctuated criticality in an unstable high-pressure combustor.

A combustor operating at subcritical pressure may also have droplets undergoing a form of punctuated criticality if a sufficiently strong pressure wave is initiated. If the pressure wave peaks above the propellant critical pressure, a droplet can heat to a temperature such that further increase in pressure drives the surface into the superheated region of the phase diagram. Thus, punctuated criticality may be a very common feature of two-phase combustion systems. In fact, it is even conceivable that similar processes occur in the burning of solid propellants where the liquid mixture on the surface can approach a critical state and acoustic oscillations are initiated within the combustor. It would seem preliminary theoretical indications justify more thorough research on this potentially important phenomenon.

CHAPTER 6

PRELIMINARY RESULTS FROM DROPLET COMBUSTION EXPERIMENTS AT ELEVATED PRESSURES

6.1 SCOPE OF EXPERIMENTAL EFFORT

The experimental work reported in this thesis is only the preliminary effort in an ambitious experimental program to observe the temporal and spatial behavior of evaporating and combusting discrete droplets in a high-pressure environment. The long term goal of this project is to observe, using laser-based imaging systems, the life history of evaporating and combusting free droplets, from subcritical heat-up through critical transition, with emphasis on deformation, break-up, and gasification behavior. The transitional regime is of special interest because of the unique critical phenomena which affect the gasification process. Initial work, however, is concentrated on suspended hydrocarbon droplets combusting in air at elevated but subcritical pressures.

6.2 EXPERIMENTAL APPARATUS AND SET-UP

At present, the experimental arrangement consists of a high-pressure test chamber with a beaded quartz fiber for suspending droplets and a shadowgraph system with laser backlight source and a line pass filter as shown in Figure 46. The test chamber, capable of withstanding a pressure of 1000 psi at a temperature of 1000 $^{\circ}F$, was constructed and tested by Pressure Products Co. of Charleston, West Virginia, and final assembly with auxiliary plumbing and support structure was completed

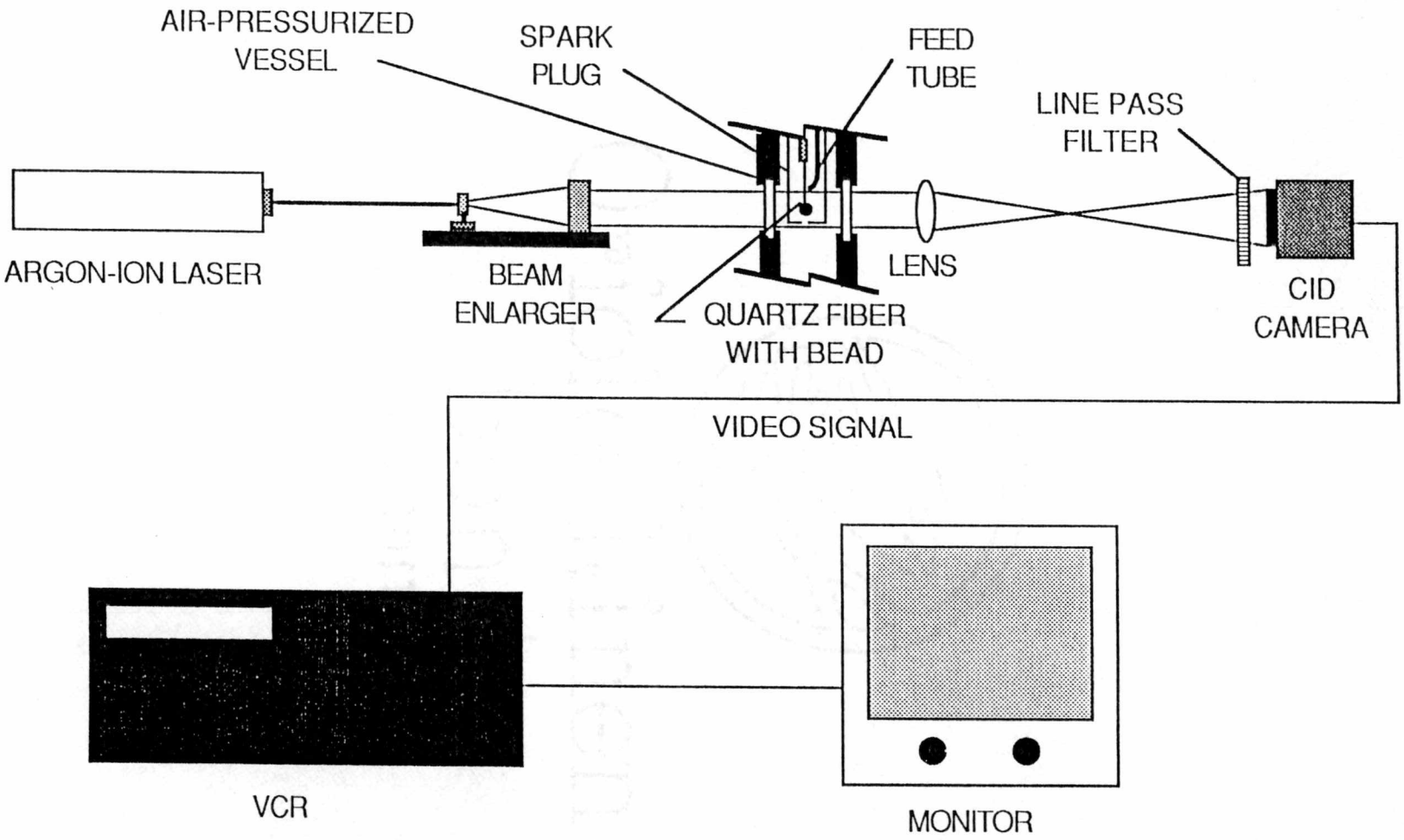

Figure 46. Schematic of experimental arrangement for elevated pressure hydrocarbon droplet combustion tests.

at UTSI. It is 30 inches high, has an inside diameter of 2 inches, and possesses 4 diametrically opposed quartz window ports for optical access. There is also a screw controlled traversing device for vertical positioning of the suspended droplet or of a droplet generator for future experiments.

The test chamber is set up as a through-flow device although current tests are conducted in a static environment. The high-pressure gas supply can be regulated upstream to the desired test pressure while the flow rate is adjusted by a needle valve downstream. A pressure gage is located at the exit manifold as well as a relief valve for quick blow down in case of an accidental surge in pressure. The pressure vessel is mounted on a 2 inch thick aluminum plate which has casters affixed for ease of positioning, and it is ensealed within an aluminum box structure.

A shadowgraph imaging technique is utilized to produce a droplet image during the burn. The image system consists of an argon–ion laser whose beam is expanded and projected through the vessel ports. A simple lens gathers the image which is magnified with a ratio of about 5:1 and passed through a line pass filter to eliminate flame illumination. The filtered light containing the image is projected on the sensor of a CID camera. Images are recorded on a VCR at a rate of 30 frames per second and a live CRT monitor is utilized to provide a means of observation for the operator.

The basic test procedure is straightforward. The vessel is first purged and filled with a fresh charge of air to the desired test pressure. A pressurized feed system then pushes fuel through a capillary tube onto the quartz fiber such that the fluid streams down and forms a drop on the 0.6 mm bead. Once a droplet is formed, the video recorder is started and a spark is produced for ignition. The burn is stored on tape for future analysis, and additional tests can be conducted by purging the vessel and repeating the procedure.

6.3 EXPERIMENTAL RESULTS

A developmental process was initiated as preliminary experiments were conducted and problems emerged. Most of the complications were trivial requiring minor adjustments in the positioning of the feed system and the spark electrodes. For example, the capillary tube outlet must be close enough to the bead such that the liquid stream doesn't run off the tip but slows down enough to form a droplet, yet far enough away not to drastically interfere with the burning process. In addition, the spark electrodes must be close enough to the droplet for ignition but again sufficiently distant to be a negligible participant in the burn. Other problems were of a more conceptual nature and will require alteration to the experimental design.

The most critical problem appears to be the effect of the shock wave from the spark on the droplet. At low pressures, less than 200 psia, the shock wave causes the droplet to oscillate on the bead, but the droplet manages to cling to the tip. For pressures above 200 psia, however, the shock wave tears the drop from the bead and the burn cannot be observed. With a very small spark gap, the shock was still too strong, and if the electrodes were moved further away, ignition wuld not occur. It seems, therfore, that spark ignition may have to be abandoned for a movable hot wire ignition source to obtain future burns above 200 psia.

Some of the subcritical pressure preliminary tests obtained during the developmental stage have been analyzed for presentation and for confirmation of some expected qualitative trends. The stored images were placed on the VICOM digital image processor where size measurements could be easily made. Because the droplets were not spherical, the vertical and horizontal lengths were measured from which an equivalent sphere could be determined by assuming the perturbed droplet was ellipsoidal in shape. Equating the volumes of an ellipsoid and a sphere produces

an expression for the equivalent spherical diameter as used by Kobayasi (1955)

$$d_d = [l_v l_h^2]^{\frac{1}{3}} \tag{6.1}$$

where l_v is the length of the vertical axis and l_h is the length of the horizontal axis.

The tests analyzed are presented in Figures 47, 48, 49, and 50. Figure 47 is the results for n-pentane burning in dry air at a reduced pressure of $P_r = 0.2343$, Figure 48 is for the same components at a reduced pressure of $P_r = 0.3364$, and Figure 49 is for the same system at a reduced pressure of $P_r = 0.4386$. The burning of 2,2,4 trimethylpentane, which has a much lower critical pressure than n-pentane, is shown in Figure 50 at a reduced pressure of $P_r = 0.5215$.

The bounce in the data is due to oscillations set up by the shock from the igniting spark. Some of these oscillations were so bad that the measurements appeared meaningless and were not included in the analysis; however, the general trend of the data appears in the shape of the curves. For instance, following an initial heat-up period, the d^2 gasification law is recovered, and a straight line could be drawn through the linear portion of the curve representing the steady-state gasification rate. Also, note the increase in thermal expansion during the heat-up period at higher pressures indicating that the steady-state droplet temperature is indeed increasing with pressure as predicted by theory. In fact, for the higher reduced pressures of $P_r = 0.4386$ and $P_r = 0.5215$ the droplet actually expands during heat-up

This preliminary data confirms expectations as predicted by theory and holds promise for useful and interesting data in future tests. It is also demonstrated that spark ignition causes stong droplet oscillation such that the droplet falls off the bead at pressures above about 200 psia and distorts the data even at the lower pressures. Thus, a less intrusive ignition source will probably be needed for future

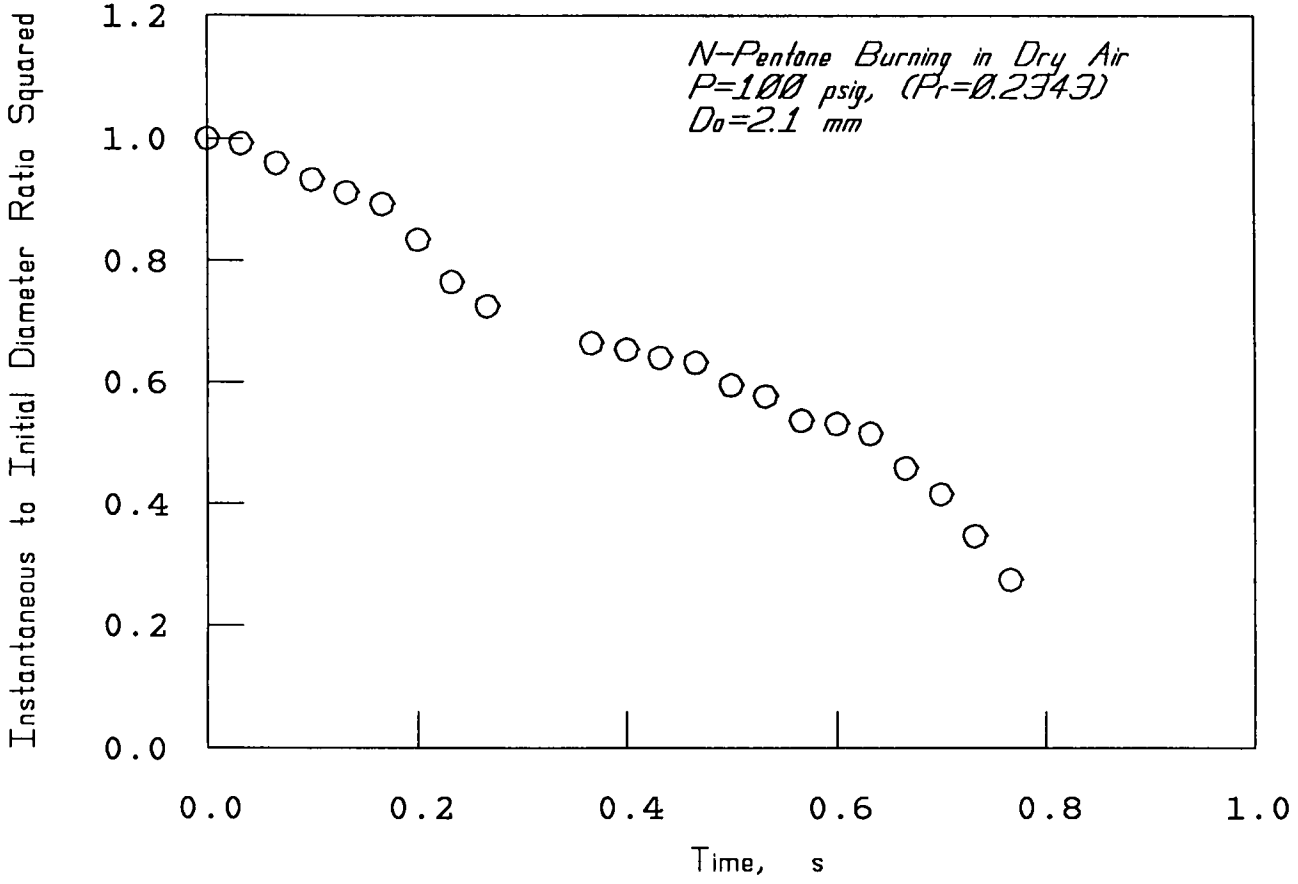

Figure 47. Experimentally observed $d_d^2/d_{d_0}^2$ ratio history for n-pentane burning in dry air at $P = 100$ psig ($P_r = 0.2343$).

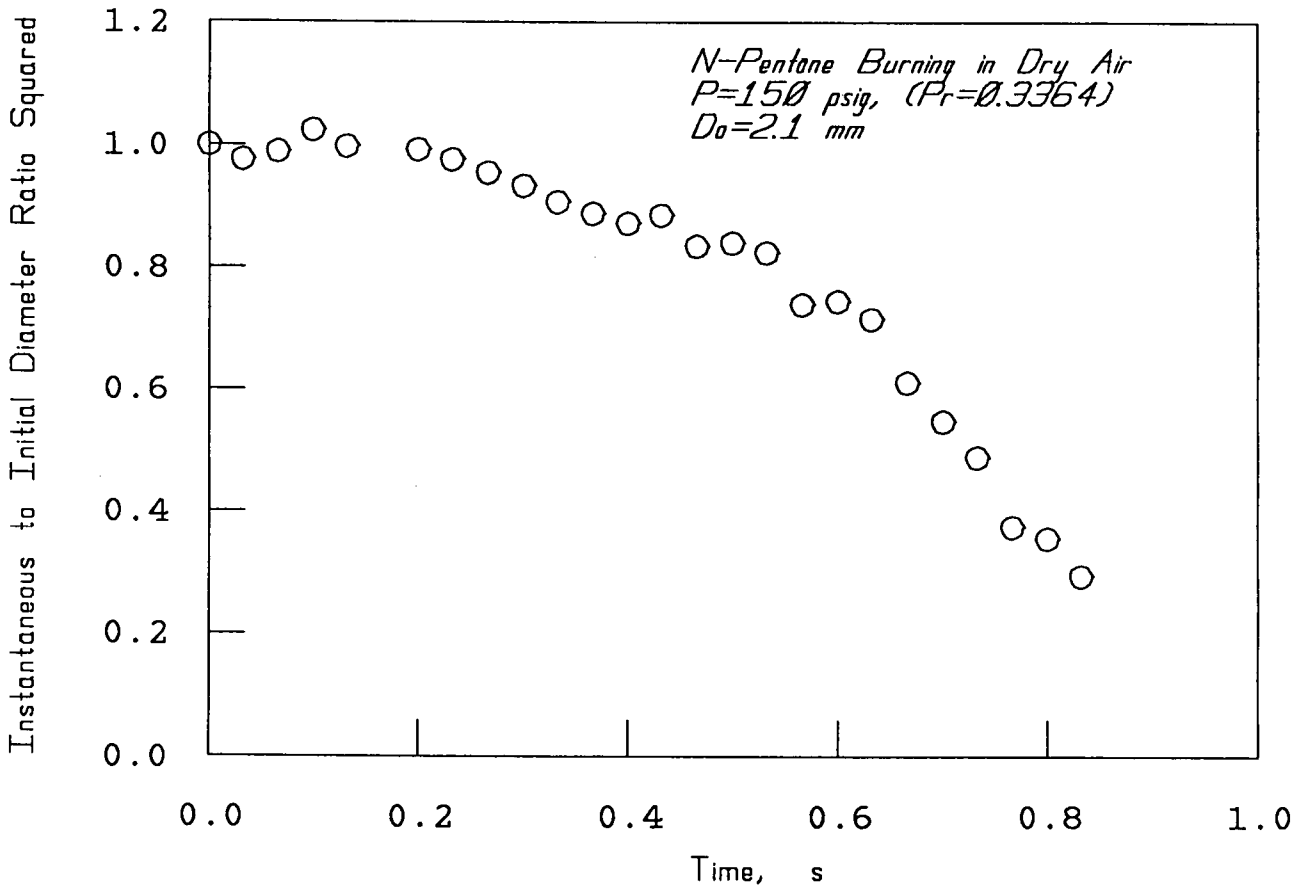

Figure 48. Experimentally observed $d_d^2/d_{d_o}^2$ ratio history for n-pentane burning in dry air at $P = 150$ psig ($P_r = 0.3364$).

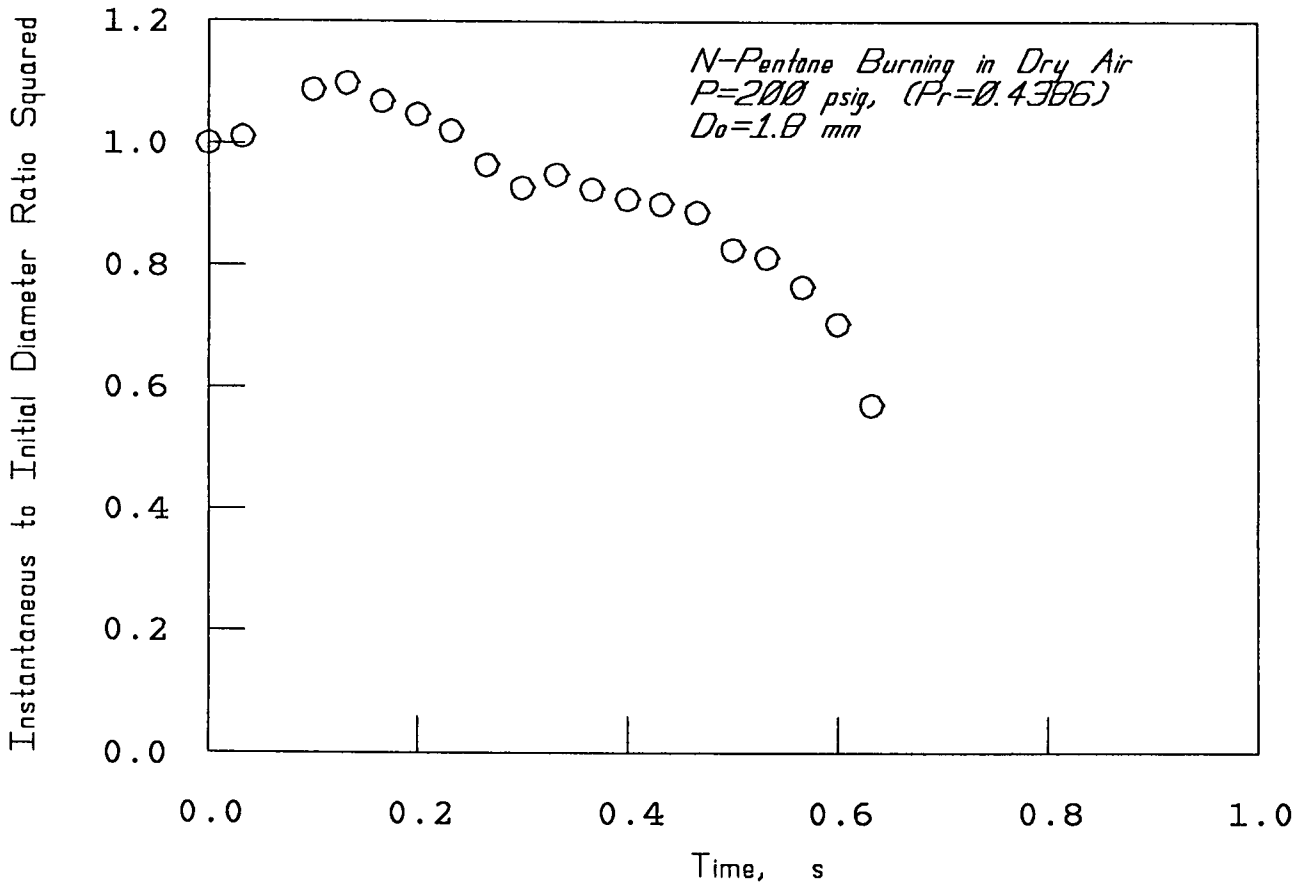

Figure 49. Experimentally observed $d_d^2/d_{d_0}^2$ ratio history for n-pentane burning in dry air at $P = 200$ psig ($P_r = 0.4386$).

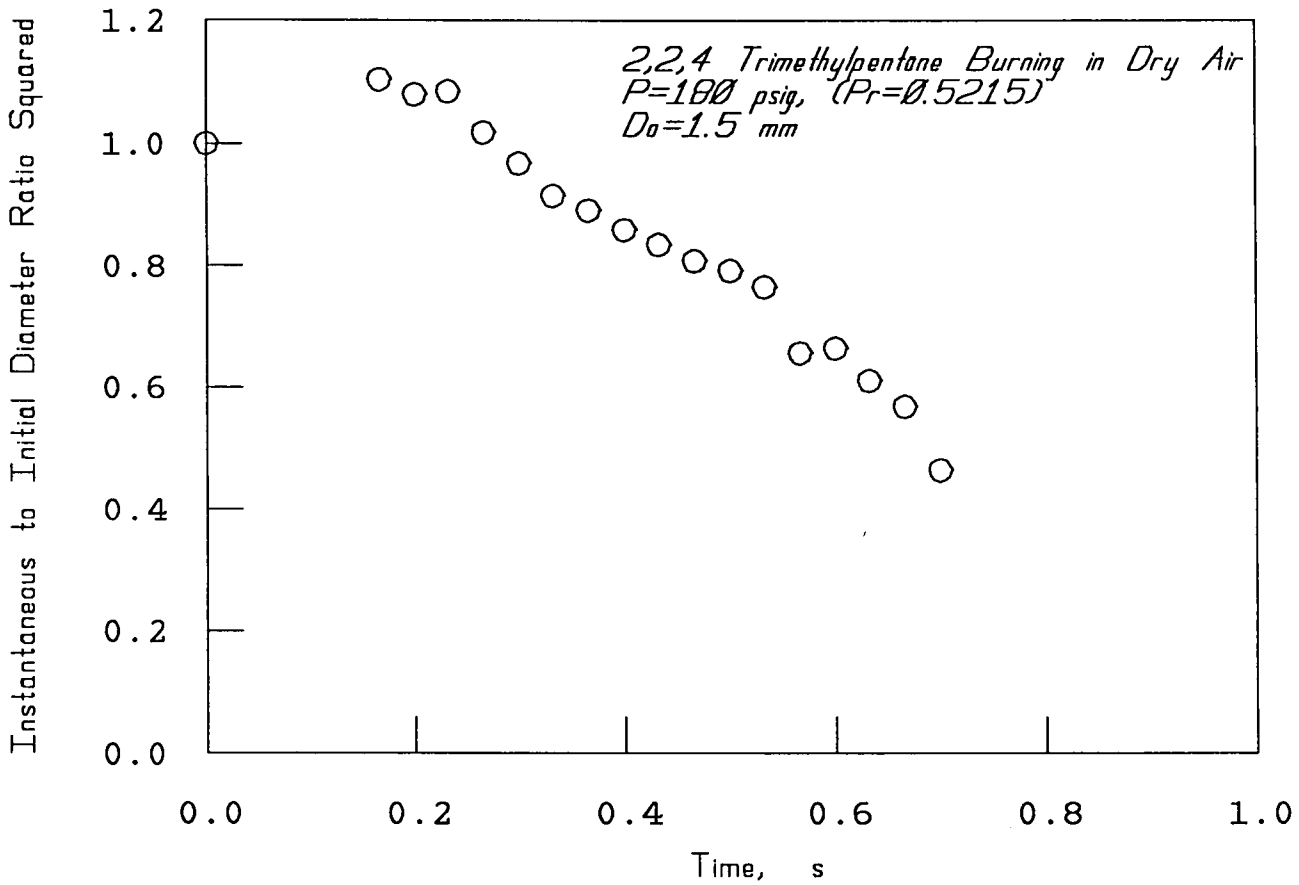

Figure 50. Experimentally observed $d_d^2/d_{d_0}^2$ ratio history for 2,2,4 trimethylpentane burning in dry air at $P = 180$ psig ($P_r = 0.5215$).

high-pressure tests. Furthermore, there are indications that a faster framing rate may be desirable at pressures approaching and above the fuel critical pressure.

CHAPTER 7

CONCLUDING REMARKS

In this study, a high-pressure discrete droplet gasification model has been formulated including vapor-liquid equilibria thermodynamics based on the Redlich-Kwong equation of state with appropriate mixing rules. The transport model is based upon extension of the conventional low-pressure model by including bulk thermal expansion and surface regression effects, an approach used by other investigators. The equilibria model was adopted from similar studies at high-pressures and is well established. A FORTRAN computer code was developed to solve the governing system of equations and simulate droplet gasification in a high-pressure combustor.

Validation calculations were conducted with respect to available experimental data for pure hydrocarbon fuels vaporizing in nitrogen gas yielding favorable comparison. Although there is a tendency to underestimate the rate of development of the process at higher pressures, the model displays correct qualitative and quantitative trends.

An investigation of pressure dependent parametric behavior was also made for n-pentane vaporizing in hot nitrogen gas to demonstrate the effect of pressure on the gasification process. The primary effects were: (1) increasing ambient pressure increases the gasification rate due to greater heat transfer and a smaller enthalpy of vaporization and (2) increased heat transfer and reduced enthalpy of vaporization, at pressures sufficiently higher than the pure liquid substance critical pressure, induce droplet heating to criticality. The crucial influence of the enthalpy of vaporization on these high-pressure phenomena cannot be stressed enough as substantial

deviation from the latent heat of vaporization causes it to be a dominant factor.

Incorporation of quantum-gas mixing rules into the vapor-liquid equilibria model provided the capability to calculate equilibrium conditions for the LOX/H_2 system which is of interest in modern, high performance liquid rocket engines. Comparison of these results with the latent heat of vaporization and vapor-liquid equilibria correlation used in a current CFD spray combustion code, ARICC–LJ, shows considerable difference indicating a need for a more physically realistic thermodynamic model. Furthermore, one-dimensional calculations for a cylindrical LOX/H_2 combustor using the formulated transport model and high-pressure equilibria model of this work show that the entire gasification process is compacted much closer to the injector face than is predicted by the current submodels in the ARICC–LJ spray combustor code.

Because of the intimate relationship between propellant gasification and liquid rocket combustion instability, the high-pressure model was also examined for the case of a superimposed transverse-mode acoustic oscillation within a cylindrical LOX/H_2 combustor. While the gasification frequency response characteristics were not specifically investigated, an interesting thermodynamic behavior in response to the oscillating pressure field was implied by theory. It was found that after the LOX droplet is heated to criticality a pressure increase forces the droplet surface into the mixture superheated region such that rapid gasification must occur. This oddity, termed here as punctuated criticality, could obviously act as an instability initiator or as a Rayleigh-mechanism for driving the instability. This phenomenon may be of much possible importance, if the theory predicts the actual physics, and should be pursued experimentally. For example, experiments on a suspended droplet inside a rapid compression machine would seem to be appropriate.

Finally, some preliminary experimental size data on suspended hydrocarbon

droplets combusting at elevated pressures have been presented. Although the experiments were only conducted up to a chamber pressure half of the fuel critical pressure, the results display expected qualitative trends.

In conclusion, it is believed that the model formulated in this work is of value in engineering design calculations and is sufficiently comprehensive yet simple enough for inclusion in a spray combustion simulation code. Also, a possible spray combustion instability mechanism, punctuated criticality, has been deduced and is probably deserving of further investigation.

LIST OF REFERENCES

Campbell, D. T. and Chadwick, W. D. (1968). "Combustion Instability Analysis at High Chamber Pressure", Rocketdyne, AFRPL TR 68-179.

Canada, G. S. and Faeth, G. M. (1975). "Combustion of Liquid Fuels in a Flowing Combustion Gas Environment at High Pressures," *Fifteenth Symposium (International) on Combustion*, pp.419-428, The Combustion Institute, Pittsburg.

Chang, X., Fujiwara, T., and Umemura, A. (1969). "Analysis of Droplet Combustion at Supercritical Conditions," *Dynamics of Reactive Systems Part II: Heterogeneous Combustion and Applications*, pp. 169-181, Progress in Astronautics and Aeronautics Volume 113, AIAA, Inc., Washington, D. C.

Chervinsky, Amoa (1969). "Supercritical Burning of Liquid Droplets in Stagnant Environment," *AIAA Journal*, Vol. 7, No. 9, pp. 1815-1817.

Chiu, H. H. (1986). "Theory of Bipropellant Combustion, Part I – Conjugate, Normal, and Composite Combustion Phenomena," AIAA Paper No. 86-0220.

Chiu, H. H., Ahluwalia, R. K., and Koh, B. (1978). "Spray Group Combustion," AIAA Paper No. 78-75.

Chueh, P. L. and Prausnitz, J. M. (1967). "Vapor-Liquid Equilibria at High Pressures. Vapor-Phase Fugacity Coefficients in Nonpolar and Quantum-Gas Mixtures," *I&EC Fundamentals*, Vol. 6, No. 4, pp. 492-498.

Chueh, P. L. and Prausnitz, J. M. (1968). "Calculation of High-Pressure Vapor-Liquid Equilibria," *I&EC*, Vol. 60, No. 3, pp. 34-52.

Combs, L. P. (1964). "Calculated Propellant Droplet Heating Under F-1 Combustion Chamber Conditions," Rocketdyne RR 64-25.

de Santis, R., Breedveld, G. J. F., and Prausnitz, J. M. (1974). "Thermodynamic Properties of Aqueous Gas Mixtures at Advanced Pressures," *Ind. Eng. Chem. Process Des. Develop.*, Vol. 13, No. 4, pp. 374-377.

Faeth, G. M., Dominics, D. P., Tulpinsky, J. F., and Olson, D. R. (1969). "Supercritical Bipropellant Droplet Combustion," *Twelfth Symposium (International) on Combustion*, pp. 9-18, The Combustion Institute, Pittsburg.

Faeth, G. M. and Lazar, R. R. (1971). "Fuel Droplet Burning Rates in a Combustion Gas Environment," *AIAA Journal*, Vol. 9, No. 11, pp. 2165-2171.

Faeth, G. M. (1977). "Current Status of Droplet and Liquid Combustion," *Progress in Energy and Combustion Science*, Vol. 3, pp. 191-224, Permagon Press, New York.

Faeth, G. M. (1979). "Spray Combustion Models – A Review," AIAA Paper No. 79-0293.

Faeth, G. M. (1983). "Evaporation and Combustion of Sprays," *Progress in Energy and Combustion Science*, Vol. 9, pp. 1-76, Permagon Press, New York.

Fang, J. J. and Jones, Y. T. (1987). "Development of a Generic Combustion Stability Code for Liquid Propellant Rocket Engines," 24^{th} JANNAF Combustion Meeting.

Gibbs, J. W. (1961 re-publication). *The Scientific Papers of Josiah Willard Gibbs*, Vol. I, Dover Publications, Inc., New York.

IMSL© Software Library: FORTRAN Subroutines for Mathematics and Statistics (1985). IMSL, Inc., Houston, Texas.

Harrje, D. T. and Reardon, E. M. (eds) (1972). *Liquid Propellant Rocket Combustion Instability*, NASA SP-194.

Harper, E. Y., Grube, G. W., and Chang I-Dee (1971). "The Deformation and Instability of a Suddenly Accelerated Liquid Drop," ASME Paper No. 71-393.

Heidmann, M. F. and Wieber, P. R. (1966). "Analysis of n-Heptane Vaporization in Unstable Combustor with Traveling Transverse Oscillations," NASA TN D-3424.

Hsieh, K. C., Shuen, J. S., and Yang, V. (1988). "Analysis of Multi-Component Droplet Vaporization at Near Critical Conditions," AIAA Paper No. 88-637.

Jiang, T. L. and Chiu, H. H. (1986). "Theory of Bipropellant Combustion, Part II – Conjugate, Normal, and Composite Combustion in a Liquid Propellant Rocket Combustion Chamber," AIAA Paper No. 86-0221.

Jin, J. D. and Borman, G. L. (1985). "A Model for Multi-Component Droplet Vaporization at High Ambient Pressures," SAE Paper No. 850264.

Kadota, T. and Hiroyasu, H. (1976). "Evaporation of a Single Droplet at Elevated Pressures and Temperatures," *Bull. JSME*, Vol. 19, No. 138, pp. 1515-1521.

Kadota, T. and Hiroyasu, H. (1981). "Combustion of a Fuel Droplet in Supercrit-

ical Gaseous Environments," *Eighteenth Symposium (International) on Combustion*, pp. 275-282, The Combustion Institute, Pittsburg.

Kobayasi, K. (1955). "An Experimental Study on the Combustion of a Fuel Droplet," *Fifth Symposium (International) on Combustion*, pp. 141-148, The Combustion Institute, Pittsburg.

Kogarko, S. M., Gel'fand, B. E., Gubin, S. A., and Borisov, A. A. (1971). "Dynamics of the Breakdown of Liquid Droplets in a Gas Flow," *Soviet Physics - Doklady*, Vol. 16, No. 5, pp. 358-360.

Kuo, K. K. (1986). *Principles of Combustion*, John Wiley & Sons, Inc., New York.

Lazar, R. S. and Faeth, G. M. (1971). "Bipropellant Droplet Combustion in the Vicinity of the Critical Point," *Thirteenth Symposium (International) on Combustion*, pp. 801-811, The Combustion Institute, Pittsburg.

Law, C. K. (1982). "Recent Advances in Droplet Vaporization and Combustion," *Progress in Energy and Combustion Science*, Vol. 8, pp. 171-201, Permagon Press, New York.

Liang, P. Y., Fisher S., and Chang, Y. M. (1985). "Comprehensive Modeling of a Liquid Rocket Combustion Chamber," AIAA Paper No. 85-0232.

Liang, P. Y. (1989). *ARICC-LJ User's Manual*, 1st Edition, Rockwell International, Rocketdyne Division, Los Angeles, California.

Manrique, J. A. and Borman, G. L. (1969). "Calculation of Steady State Droplet Vaporization at High Ambient Pressures," *Int. J. Heat Mass Transfer*, Vol. 12, pp. 1081-1095.

Mao, C. P., Szekely Jr., G. A., and Faeth, G. M. (1980). "Evaluation of a Locally Homogeneous Flow Model of Spray Combustion," *J. of Energy*, Vol. 4, No.2, pp. 78-87.

Matlosz, R. L., Leipziger, S., and Torda, T. P. (1972). "Investigation of Liquid Droplet Evaporation in a High Temperature and High Pressure Environment," *Int. J. Heat Mass Transfer*, Vol. 15, pp. 831-852.

McCreath, C. G. and Chigier, N. A. (1973). "Liquid Spray Burning in the Wake of a Stabilizer Disk," *Fourteenth Symposium (International) on Combustion*, pp. 1355-1363, The Combustion Institute, Pittsburg.

McKinley, C., Brewer, J., Wang, E. S. J. (1961). "Solid-Vapor Equilibria of the Oxygen–Hydrogen System," *Adv. Cryog. Eng.*, Vol. 10, pp. 114-124.

Newman, J. A. and Brzustowski, T. A. (1971). "Behavior of a Liquid Jet Near the Thermodynamic Critical Region," *AIAA Journal*, Vol. 9, No. 8, pp. 1595-1602.

Parsonage, N. G. and Scott, R. L. (1962). "Contribution of Octopole-Octopole Interactions to the Excess Properties of Mixtures of Tetrahedral Molecules," *J. Chem. Phys.*, Vol. 37, No. 2, pp. 304-306

Philippart, K. D. and Moser, M. D. (1988). "Stability Analyses of Liquid Oxygen/Methane Injectors Using Currently Available Analytical Tools," AIAA Paper No. 88-2851.

Poettmann, F. H. and Katz, D. L. (1945). "Phase Behavior of Binary Carbon Dioxide – Paraffin Systems," *Industrial and Engineering Chemistry*, Vol. 37, No.9, pp. 847-853.

Poston, R. S. and McKetta, J. J. (1966). "Vapor-Liquid Equilibrium in the n-Hexane–Nitrogen System," *J. Chem. Eng. Data*, Vol. 11, No. 3, pp. 364-365.

Prausnitz, J. M. and Chueh, P. L. (1968). *Computer Calculations for High-Pressure Vapor-Liquid Equilibria*, Prentice-Hall, Inc., Englewood Cliffs, New Jersey.

Prausnitz, J. M. (1969). *Molecular Thermodynamics of Fluid-Phase Equilibria*, Prentice-Hall, Inc., Englewood Cliffs, New Jersey.

Prausnitz, J. M., Lichtenthalek, R. N., de Azevedo, E. G. (1986). *Molecular Thermodynamics of Fluid-Phase Equilibria*, Second Edition, Prentice-Hall, Inc., Englewood Cliffs, New Jersey.

Priem, R. J. and Guentert, D. C. (1962). "Combustion Instability Limits Determined by a Nonlinear Theory and a One-Dimensional Model," NASA TN D-1409.

Priem, R. J. and Heidmann, M. F. (1960). "Propellant Vaporization as a Design Criterion for Rocket-Engine Combustion Chambers," NASA TR R-67.

Rabin, E., Schallenmuller, A. R., and Lawhead, R. B. (1960). "Displacement and Shattering of Propellant Drops," Rocketdyne, AFOSR TR 60-75.

Reichel, R. H., Hague, D. S., Jones, R. T., Glatt, C. R. (1973). "Program User's

Manual for Optimizing the Design of a Liquid or Gaseous Propellant Rocket Engine with the Automated Combustor Design Code AUTOCOM," NASA CR-2293.

Reid, R. C. and Sherwood, T. K. (1966). *The Properties of Gases and Liquids*, 2nd Edition, McGraw-Hill, Inc., New York.

Reid, R. C., Prausnitz, J. M., and Poling, B. E. (1987). *The Properties of Gases and Liquids*, 4th Edition, McGraw-Hill, Inc., New York.

Rosner, D. E. (1967). "On Liquid Droplet Combustion at High Pressures," *AIAA Journal*, Vol. 5, No. 1, pp. 163-166.

Rosner, D. E. and Chang, W. S. (1973). "Transient Evaporation and Combustion of a Fuel Droplet Near Its Critical Temperature," *Combustion Science and Technology*, Vol. 7, pp. 145-158.

Savery, W. and Borman, G. L. (1970). "Experiments on Droplet Vaporization at Supercritical Pressures," AIAA Paper No. 70-6.

Shearer, A. J. and Faeth, G. M. (1977). "Combustion of Liquid Sprays at High Pressures," NASA CR-135210.

Shuen, J. S. (1988). Written communication.

Solomon, A. S. P. (1984). *A Theoretical and Experimental Investigation of Turbulent Sprays*, Ph.D. Dissertation, The Pennsylvania State University.

Sonntag, R. E. and Van Wylen, G. J. (1982). *Introduction to Thermodynamics Classical and Statistical*, John Wiley & Sons, Inc., New York.

Spalding, D. B. (1959). "Theory of Particle Combustion at High Pressures," *ARS Journal*, Vol. 29, pp. 828-835.

Sutton, R. D., Hines, W. S., and Combs, L. P. (1972). "Development and Application of a Comprehensive Analysis of Liquid Rocket Combustion," *AIAA Journal*, Vol. 10, No. 2, pp. 194-203.

Tong, A. Y. and Sirignano, W. A. (1987). "Vaporization Response of Fuel Droplet in Oscillatory Field," ASME Paper No. 87-HT-58.

Tong, A. Y. and Sirignano, W. A. (1989). "Oscillatory Vaporization of Fuel Droplets in an Unstable Combustor," *J. Propulsion and Power*, Vol. 5, No.3, pp. 257-261.

Toong, Tau-Yi (1983). *Combustion Dynamics: The Dynamics of Chemically Reacting Fluids*, McGraw-Hill, Inc., New York.

Umemura, A. (1986). "Supercritical Liquid Fuel Combustion," *Twentieth Symposium (International) on Combustion*, pp. 463-471, The Combustion Institute, Pittsburg.

Valentine, R. S. (1972). "Liquid Rocket Performance, Stability, and Compatibility," *J. Spacecraft and Rockets*, Vol. 9, No.5, pp. 295-307.

Wieber, P. R. (1963). "Calculated Temperature Histories of Vaporizing Droplets to the Critical Point," *AIAA Journal*, Vol. 1, No. 12, pp. 2764-2770.

Wieber, P. R. and Mickelsen, W. R. (1960). "Effect of Transverse Acoustic Oscillations on the Vaporization of a Liquid-Fuel Droplet," NASA TN D-287.

VITA

Ronald J. Litchford attended and graduated from Tennessee public schools. He enrolled in the college of engineering at Tennessee Technological University and graduated in 1987 with a B. S. degree in Mechanical Engineering. Upon acceptance of a graduate research assistantship at the University of Tennessee Space Institute, Ron began studies for a Master's degree in Mechanical Engineering. In 1988, he was awarded a NASA Graduate Student Researcher Fellowship, through the Marshall Space Flight Center in Huntsville, Alabama, for one year of graduate study and research at UTSI. The M. S. degree was awarded in 1989.

The author is a member of the American Society of Mechanical Engineers, the American Society of Astronautics and Aeronautics, the Planetary Society, and the Tau Beta Pi Engineering Honor Society. As of this writing, Mr. Litchford is employed by the Center for Advanced Space Propulsion at the University of Tennessee Space Institute and resides with his wife, Betrice, and son, Thomas, in Huntland, Tennessee.